Asymmetry of Inorganic Nanostructures

by

Ji-Young Kim

A dissertation submitted in partial fulfillment
of the requirements for the degree of
Doctor of Philosophy
(Materials Science and Engineering)
in the University of Michigan
2018

Doctoral Committee:

Professor Nicholas A. Kotov, Chair
Professor Jinsang Kim
Doctor John Mansfield
Professor Theodore Norris

Ji-Young Kim

jyoukim@umich.edu

ORCID iD: 0000-0001-5631-957X

© Ji-Young Kim 2018

DEDICATION

To the memory of my dearest father, Seung Han Kim,

Who always believed in my ability to be successful in the academic arena.

You are gone but your guiding hand on my shoulder will remain with me forever.

Rest in Peace.

ACKNOWLEDGEMENTS

I would like to thank my advisor, Prof. Nicholas A. Kotov for not only his guidance throughout my graduate studies but also motivation on being an independent scientist. Whenever I met difficulties in my academic work, he supported me in direct and indirect ways. Also, I would like to thank all my dissertation committee members, Prof. Jinsang Kim, Dr. John Mansfield, and Prof. Ted Norris, for serving as my dissertation committees and their academic advice on my work.

I would like to thank Prof. Jae-seung Lee who was my advisor for my bachelor's and master's degrees for guiding me to the exciting world of science. I could not be what I am here without his guidance and supports. My colleague, Dr. Miao-Bin Lien and Dr. Myung-Geun Han deserve a special mention for all the delightful scientific discussions. I would like to express my gratitude to all the previous and current Kotov lab fellows.

My graduate school life in Ann Arbor would not have been complete without all my friends and members of KUAA (Korea University Alumni Association). I really enjoyed all the times with them in Ann Arbor.

And at last but not least, I would like to thank my lovely grandmother, Eun-soon Lee for all the infinite supports.

TABLE OF CONTENTS

LIST OF FIGURES

ABSTRACT

Matured syntheses of inorganic nanocolloids today have allowed production of diverse asymmertic nanoparticles (NP) and even more complex assemblies, introducing a variety of nanomaterials with unique properties. In many cases, the symmetry of the nanomaterials plays the crucial role in determining the electronic structure, optical activity and physical dynamics of the system. However, precise symmetry assignment to nanoscale materials is a challenging task due to their multicomponent nature and multiscale dynamics. Here we explore asymmetry of inorganic nanomaterials to discover fundamental mechanisms and dynamics of previously puzzling properties and develop a new methodology for syntheses and characterization.

An example of overlooked asymmetry in nanoscale system was demonstrated with gold nanorod (Au NRs). Direct observations of electrostatic properties of Au NRs via off-axis electron holography and Kelvin force microscopy showed that Au NRs have distinct asymmetry of surface charge density and therefore, behave as non-centrosymmetric structures due to uneven distribution of cetyltrimethylammonium (CTA) moieties capping two ends of NRs. The electrostatic asymmetry of Au NRs and potentially other metallic nanostructures emerging from this study showed a new pathway to explain previously puzzling discrepancies in nonlinear optical (NLO) properties in seemingly centro-symmetric nanostructures. By taking the multicomponent nature of nano-colloids, especially originated from surface ligands, into

consideration, we also showed that chiroptically active nanomaterials can be produced by self-assembled processes that are sensitive to subtle anisotropies and ligand-imposed surface of NPs. L-cysteine (L-Cys)– or D-cysteine (D-Cys)–stabilized NPs yields various chiral mesoscale structures including helices and angled conformation of nanoleaves, exhibiting unique chiropitcal properties by combining structural character with their material properties. More interestingly, the handedness of these structures depended solely on the specific Cys enantiomer, thus showing homochiral ensembles.

The organic shell can introduce a property-governing asymmetry into nanoscale system, allowing better understanding relationships between geometrical parameters and properties of complex nanomaterials. The experimental and theoretical findings here can be generalized to other nanoscale materials carrying surface stabilizers and opens new possibilities for solution processed metamaterial devices.

Chapter 1 Introduction

1.1 Motivation: Symmetry Assignment for Nanostructures

To date, the "bottom-up" approach for implementing nano/microstructure was emerged as a promising direction for technology development because this method can (a) use the intrinsic ability of nanocolloids to self-organize; (b) reduce the high energy and equipment cost of device manufacturing, and (c) impart new functionalities to the structure. A large variety of nanocolloids from matured wet-chemical syntheses can now be considered as "building blocks" for the construction of desirable material structures.(*1*) These dispersions offer highly crystalline semiconductor/metal materials, exceptional degree of structural control, and sufficient batch-to-batch reproducibility. Recent interdisciplinary research proposed new categories of assembled materials from these "building blocks", which often exhibit unique properties, hardly observed in natural materials.(*2*) Advanced or new performance from these materials leads development in various technologies including electronics, photonics, and pharmaceutical science (*3–6*) .

Symmetry assignments of the nanocolloids are foundational for theoretical and experimental evaluation of their physical properties (*7–9*)**,** and therefore, are some of the key components needed to engineer structure and property of the assembled materials (*9*, *10*). In many cases, the symmetry of the system plays crucial roles in determining the electronic structure, optical activity and physical dynamics of the particles. However, the multicomponent

nature and multiscale dynamics of nanocolloids make symmetry assignment to nanoscale colloids a difficult task.

1.2 Thesis Overview

We are specifically interested in the understanding of asymmetry of NPs to facilitate complex assembled structures having unique properties. To elucidate the role of asymmetry in inorganic NPs and their assemblies, we have paid special attention to the change in electrostatic and optical property in response to the asymmetry introduced to the system, including but not limited to, nonlinear optical and chiroptical responses. Organic coating of NPs was taken into consideration to assign the symmetry of NPs, which enables us to not only understand phenomenal optical responses from existing systems but also new insight to develop versatile self-assembly methods, providing an important direction for future research - engineering a new class of materials with unprecedented functionalities.

1.2.1 Organic Layer of Inorganic Nanostructures

Nanoscale building blocks -- exemplified in many cases by NPs -- must be dispersible in a solvent; therefore, they must carry a protective coating typically made of surfactants or other organic materials that make NP compatible with a particular organic or aqueous media.(*11*) The surfactant coating is also necessary to make possible the observation of the size quantization effects(*12*) and, in many cases, to obtain high crystallinity of NPs.

It has largely been assumed that the geometry of the inorganic core is representative of the symmetry of the nanoscale particle as a whole. For instance, plasmon oscillations of gold

nanorods (Au NRs) have been interpreted in terms of the electromagnetic modes confined in a perfect cylinder or prolate spheroid (*13*, *14*). However, several recent studies have reported that the actual electrostatic properties of gold NPs showed considerable asymmetry, which are different from the symmetry the bare Au core represents.(*15*) (**Fig. 1.1**)

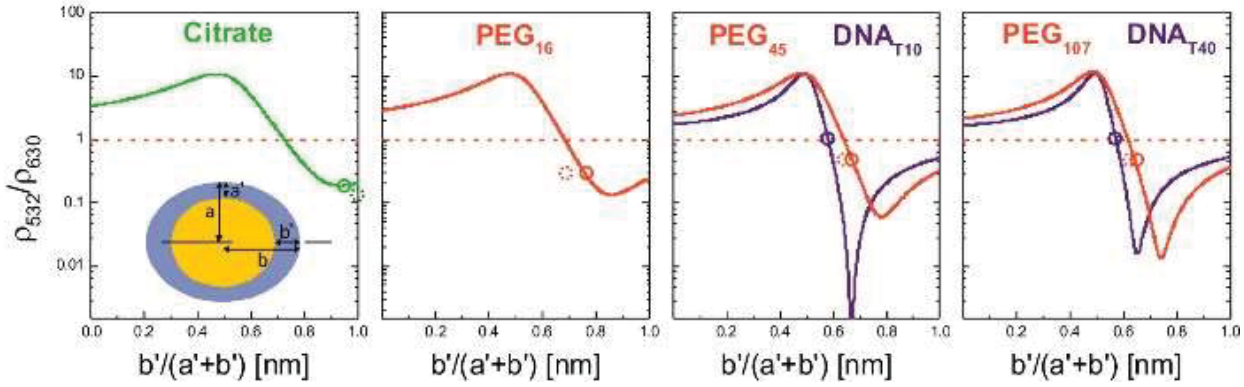

Figure 1.1 Comparison between the experimental asphericity parameter b′/(a′ + b′) (dashed circles) with the corresponding computed (solid circles) b′/(a′ + b′) for the same AuNP with six different coatings. Reproduced from ref.(*15*) Copyright 2014 American Chemical Society.

Therefore, we decided to focus on possible asymmetry introduced by surfactants and other organic materials being used to synthesize and/or disperse nanocolloids, and always take them into consideration as an independent factor for property evaluation.

1.2.2 Gold Nanorods: Symmetry and Optical Properties

Gold nanorods (AuNRs) exhibit unique optical properties based upon surface plasmon (SP) oscillation of free electrons, which is highly attractive to researchers for a variety of applications such as near-field imaging,(*16*) enhanced fluorescence spectroscopy,(*17*) Raman spectroscopy,(*18*) optoelectronic devices,(*19*, *20*) photothermal therapy, (*21*) and sensing applications.(*22*, *23*) The linear optical properties of Au NRs are mainly governed by collective

oscillations of the conduction electrons. Set into resonant oscillation at certain wavelengths of incident light, conduction electrons exhibit plasmon resonances which lead a strong absorption/scattering and local field enhancement.

Due to elongated geometry of AuNR, two plasmon bands are seen in the UV−vis−NIR absorption spectrum: one band for the transverse plasmon and the other of the longitudinal plasmon (**Fig. 1.2**).(*24*) Regardless of aspect ratio of the AuNR, the transverse plasmon exhibits almost similar absorbance of spherical AuNPs whose plasmon absorbance has similar energies across 4−200 nm AuNP diameters. In contrast, the energy of the AuNR longitudinal Plasmon is, however, strongly influenced by the aspect ratio of AuNR, thus approaching to the NIR region. These shape-dependent optical properties of AuNR have been taken advantage to enable various applications.

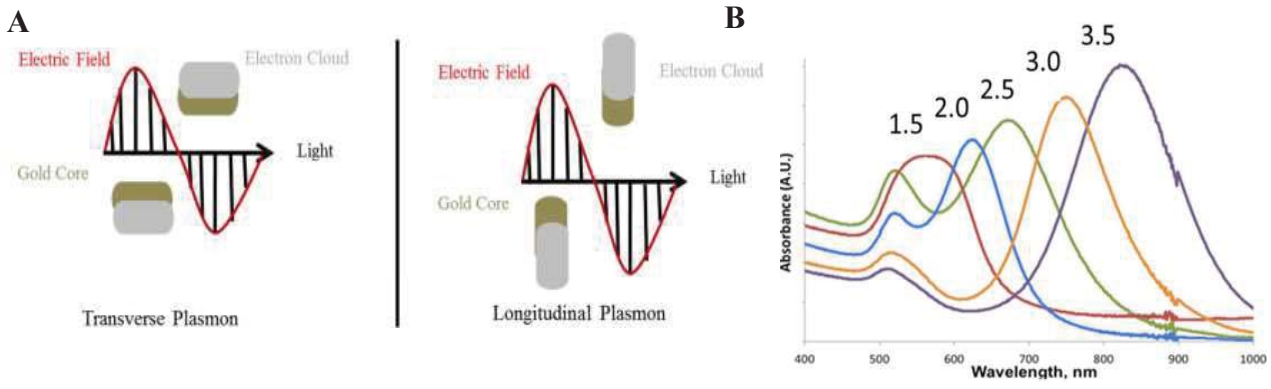

Figure 1.2 (**A**) Schematic representation of AuNR transverse and longitudinal plasmon (**B**) Absorbances in AuNRs with various aspect ratios. Reproduced from ref.(*24*). Copyright 2014 American Chemical Society

The ellipsoid particle model for NRs captures many of the key features of the optical properties found in the physical experiments. The complete electromagnetic fields of the sub-

wavelength ellipsoid particles can be solved with Gans theory(*25*), an extension of Mie theory for the case of spheroidal particles. The calculated result helps explain the optical behaviors such as how the longitudinal absorption band can red-shift largely from the visible to near-infrared region with increasing aspect ratio and media dielectric constant (**Fig. 1.3**) The absorption spectrum is only dependent on the aspect ratio of the particles and not on the absolute dimensions. The theoretical analysis also showed that the absorption efficiency is dominant for smaller rods and the scattering efficiency is dominant for larger rods, which provide good standard for choosing the system for biomedical applications. For instance, larger NRs are preferred for imaging, whereas smaller NRs are preferred for photothermal therapy, as light is mainly adsorbed by the particles, and thus, efficiently converted to heat for cell and tissue destruction.

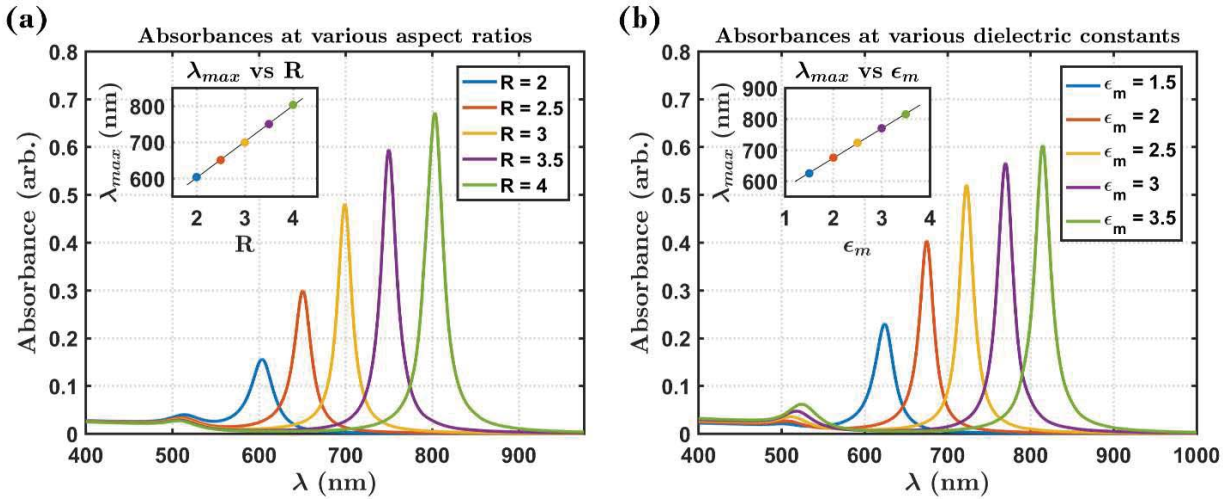

Figure 1.3 Caculated absorbance spectra with Gans Theory. Longitudinal absorption band red-shifts (a) with increasing aspect ratio, R (at $\epsilon_m = 1.5$) and (b) with increasing media dielectric constant, ϵ_m (at $R = 3$). Within the range of these specific examples, the spectral location of the maximal absorbance, λ_{max}, is almost linearly proportional to both R and ϵ_m, see insets. Reproduced from ref (*26*).

Despite the fact that Gans theory can explain many of the optical properties of AuNRs, experimental data still showed unexpected results (e.g. λ_{max} does not only depend on the particle aspect ratio, but also on the particle width and length independently).(*27*) A precise modeling of the NRs is necessary to provide more accurate optical properties of AuNRs.

Together with their linear properties, nonlinear optical properties of the AuNRs were also reported and appeared to be a promising field for photonic applications. The third-harmonic generation (THG) from individual gold colloidal particles down to 40 nm diameter was first observed by Lippitz et al.,(*28*) and THG imaging of Au NRs was demonstrated(*29*); Second Harmonic Generation (SHG) from Au NRs was also investigated by Singh et al.(*30*) However, second non-linear optical properties such as SHG are forbidden for centrosymmetric metal nanoparticles. Although a theory to explain the phenomenological SHG from centrosymmetric spherical metallic particles was suggested by J. I. Dadap et al.(*31*, *32*), the surprisingly strong SHG signal observed in the small seemingly centrosymmetric particles cannot be still rationalized sufficiently. These phenomena have been attributed to surface defects, the asymmetry of metal-media interface, and retardation (30, 31, 33, 34, 44). However, we have questioned directly the presumed centro-symmetry of Au NR instead in this thesis work, with possibility of introducing asymmetry from their organic layer.

1.2.3 Chirality of Inorganic Nanoparticles and Assemblies

Chirality is terminology derived from the Greek χειρ (kheir), meaning "hand", representing a structure which may possess three elements of symmetry: rotation, inversion and

reflection; a chiral structure is non-superimposable on its mirror image. The importance of chirality was discovered in 1963, when the wrong handed thalidomide in a drug caused the critical birth defects. The molecular and nanoscale chirality of biomolecules, surfactants, and liquid crystals, as well as hybrid materials constructed thereof, has been extensively studied and is generally well understood (*33*–*35*).

The field of chiral inorganic nanostructures is still evolving and as such, their optical properties remain largely unexplored compared to simple organic materials. Recent studies shown that high polarizability of plasmonic metals, combined with asymmetric geometries of NPs (*36*) or chiral arrangements in supraparticles (*37*), leads to strong chiroptical activity. This knowledge guides design principles for complex assemblies with new optical, chemical, and biological functions and their utilization in chiral detection (*23*), chiral catalysis (*38*), telecommunications (*39*), and medical diagnostics (*40*). The synthesis and assembly methods have been now expanded to sophisticated synthetic protocols involving nanostructures from semiconductors, (*41*, *42*) ceramics,(*43*) and nanocarbons(*44*) over the last decade.

Enantiomers are chiral molecules that are mirror images of one another. Typically, the molar ratio of one enantiomer over another is expressed with enantiomeric excess measured in percent (%), and abbreviated to ee. When the compound consists of a single enantiomer (ee = 100%), it is called homochiral. Homochiral compounds are commonly found among bioorganic substances but not among inorganic nanostructures.(*45*) This thesis work will cover both

experiment and theoretical understating of homochiral assemblies starting with the asymmetry of individual NPs originated from organic layers.

Chapter 2 Inversion Symmetry Breaking in Gold Nanorods

From Kim, J. -Y.; Han, M. -G.; Lien, M. -B.; Magonov, S.; Zhu, Y.; George, H.; Norris, T. B.; Kotov, N. A., "Dipole-like electrostatic asymmetry of gold nanorods." Science Advances 4, e1700682 (2018). Reprinted with minor modifications with permission from AAAS.

Contributions: Kotov, N. A. conceived the project. Kim, J.-Y. designed the study, prepared the samples to be characterized, performed the experiments, and ran the finite element simulations. Under the guidance of Norris, T. B., Lien, M. -B., and George H. measured the NLO response of AuNR composite films. Han, M. -G., Zhu, Y., and Kim, J. -Y. acquired the electron microscopy images. Magonov, S. conducted Kelvin probe microscopy. Kim, J.-Y. and Kotov, N.A. analyzed the data and wrote the manuscript.

2.1 Introduction and Background

Plasmon mapping using different techniques, including electron energy loss spectroscopy (EELS) (*46–48*), cathodoluminescence (*49*), and near-field microscopy (*50*), have consistently recorded curious asymmetry in NRs. For example, Rossouw *et al.* reported plasmon modes displaced by (17 ± 3) nm with respect to the center of nearly perfect silver nanorods (NRs) (*48*). Some of these observations were attributed to unspecified effects of the local environments around the NRs. However, calculations reveal that even close topographical or chemical neighbors cannot produce the considerable mode shifts observed in experimental data in previous literature (**Fig. 2.1**). From a different standpoint, the quantitative assessment of the catalytic reactivity of AuNRs were reported to have a distinct gradient along the longitudinal axis (*51*). Such a gradient of catalytic activity could not also be rationalized as effects of the local

environment, because they would be averaged in the dispersed state and over the large number of nanowires and NRs. Other phenomena that are of interest are non-linear optical (NLO) responses from NRs and nanoparticles (NPs). The second harmonic generation (SHG), third harmonic generation (THG), and nonlinear (multiphoton) photoluminescence (NPL) of metal NPs have been extensively studied over the past decade (*29*, *32*, *50*, *52–59*). A consistent description of NLO emission in metal nanostructures has not yet been attained, however. For instance, the strong SHG signal observed in the small seemingly centrosymmetric particles cannot be rationalized by conventional nonlinear optical processes since it should be forbidden in such system (*53*, *56*). These phenomena have been attributed to surface defects, the asymmetry of metal-media interface, and retardation (*32*, *56–58*, *60*). A recent observation of NPL from Au nanostructures, being dependent on NP shapes (*59*), contradicts the conventional interpretation of NPL as electron-hole recombination located at different energy states in the metal (*50*, *61*). Since the shape of nanoscale metals should have little effect on energy of solid state electronic levels and recombination rates, additional factors are necessary to explain this dependence. These considerations prompted us to investigate whether NRs are centrosymmetric with respect to the dimensions of the gold core, but non-centrosymmetric with respect to another parameter.

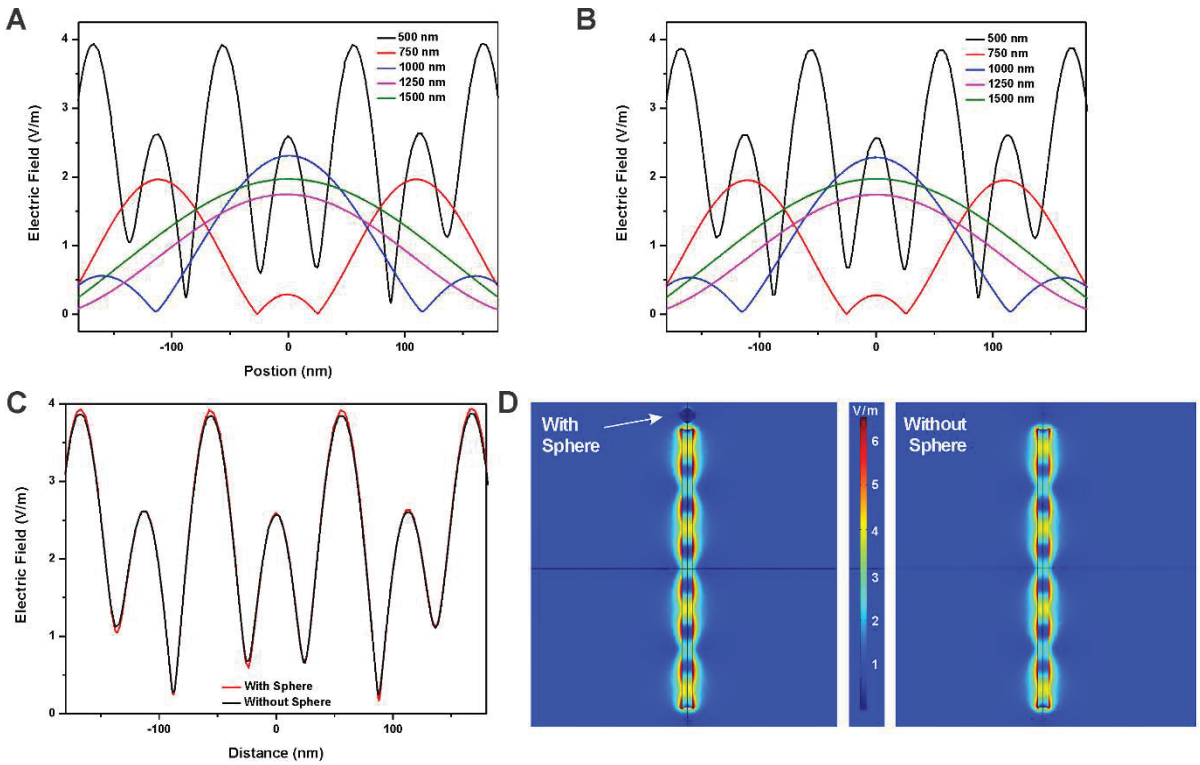

Figure 2.1 Computations of plasmon modes of silver nanowire (NW) with and without a neighbor particle. Electric field profile along NW long axis with (**A**) /without (**B**) a neighbor sphere interacting with different wavelengths of plane-polarized waves. A comparison of two plasmon line profiles (**C**) and images (**D**) for the wavelength of 500 nm.

2.2 Hypothesis

Unequal density of surface ligands due to the difference in their affinity to {111} facets compared to other major facets of gold NPs, such as different density of cetylthimethylammonium bromide (CTAB) on the sides and ends of NRs, is well known (*15*, *62–65*). Recent studies of NR geometries at atomic resolution (*63*, *66*) also reported that the facet compositions may not necessarily be simple combination of these facets, but complex, due to

rounded shape and "bridging" face between cylindrical body and the ends. However, these models still retain central symmetry. We hypothesized that different surface area of {111} and {110} facets at the two ends of the NRs (**Fig. 2.2 A**) and/or different packing density of the surface ligands may cause loss of the central symmetry. Since CTAB moieties carry charges, such a model must lead to non-centrosymmetric electrostatic potential on the outer surface of the AuNRs (**Fig. 2.2 B, case 2**).

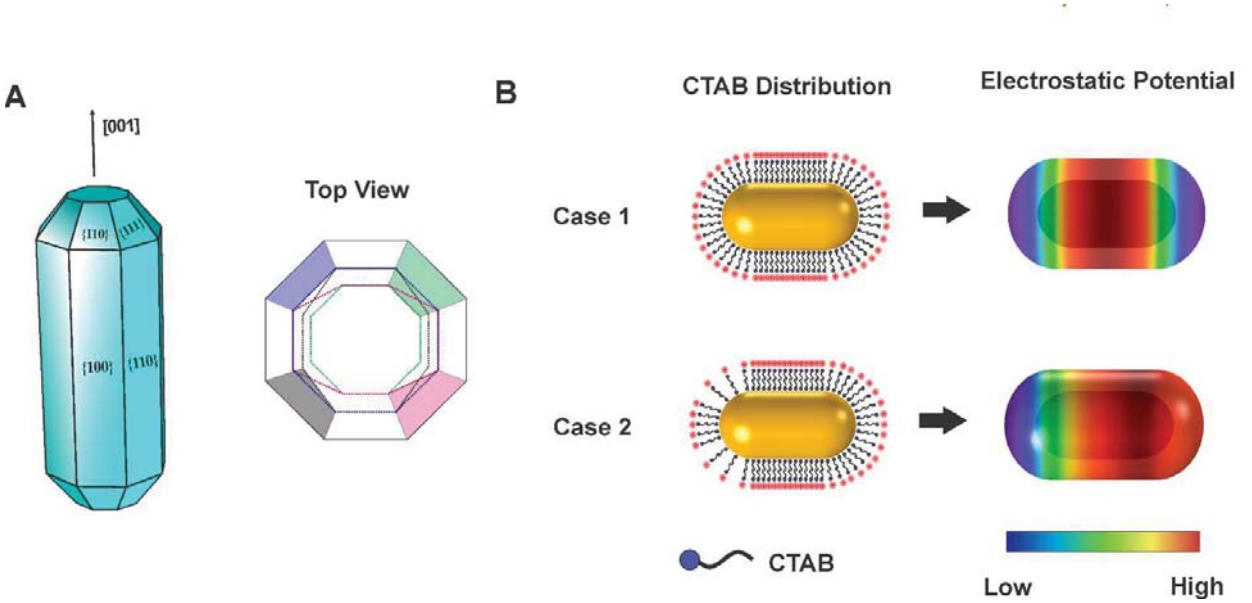

Figure 2.2 Schematic description of possible electrostatic potential in AuNRs. (**A**) Typical morphology and surface facets of AuNR grown with CTAB surfactant. Top view shows possible complexity of facets composing ends of AuNR. The colored areas are presenting possible variation of {111} facet area. (**B**) Expected electrostatic potential at outer surface of CTAB with equal (case 1) and unequal (case 2) capping for two ends.

2.3 Electrostatic Potential Gradient in Electron Hologram

The nanometer-resolution off-axis electron holography (EH) enables direct imaging of the electrostatic potential around a nanoscale object (*67*). The potential can be determined by

evaluating the phase shift, $\phi(x)$, of an electron wave that has passed through the sample, relative to the wave that has travelled through a vacuum:

$$\phi(x) = C_E \int V(x, z)\ dz - \frac{e}{\hbar} \iint B_{\perp}(x, z) dx dz \quad \textbf{(Eq. 2.1)}$$

where z is the incident beam direction, x is a direction in the plane of the sample, V is the electrostatic potential, $B\perp$ is the component of the magnetic induction perpendicular to both x and z, and C_E is the interaction constant depending on the acceleration voltage of the electron microscope (*68*). For a non-magnetic material such as gold, the second term of **Eq. 2.1** is zero and only the first term contributes. Therefore, the magnitude of $\phi(x)$ is proportional to the integral of the electrostatic potential along a straight-line path through the specimen.

The phase shift map, reconstructed from the electron hologram, shows that standard NRs stabilized by CTAB are asymmetric (**Fig. 2.3 A, B**). The $\phi(x)$ along the long axis of the NR is linearly fitted with a slope of 0.02 rad/nm in the range of the cylinder body. We took EH images of more than 50 nanorods, including different aspect ratios (from 3 to 6), in high and low magnification imaging conditions. Their $\phi(x)$ values display distinct gradients along the long axis, which corresponds to electrostatic potential gradient of 0.11-0.07 V/nm, are consistent across multiple areas on the microscopy grid, separately prepared samples, and imaging conditions. Contrastingly, $\phi(x)$ values observed for NRs that lack a CTAB layer are symmetrical with no slope (**Fig. 2.3 C, D**).

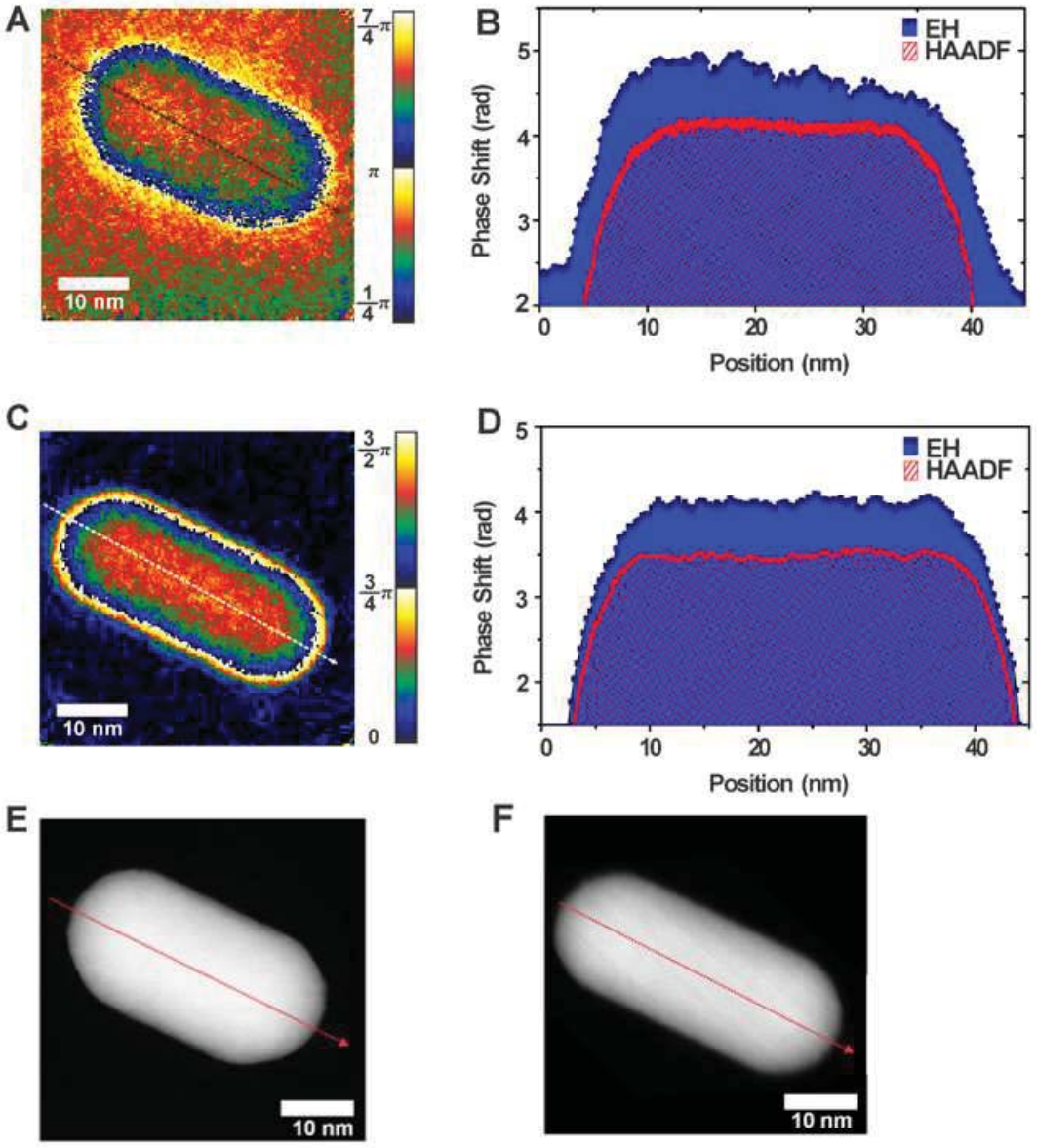

Figure 2.3 Electrostatic properties of individual AuNRs. Phase map (**A,C**) and profiles (**B,D**) along the longitudinal axis of the AuNRs supported by silicon grids with (A,B) and without (C,D) CTAB coating. Blue and red curves are extracted from their phase shift maps by electron holography (EH) and high angle angular dark field (HAADF) images, respectively. (**E**, **F**) HAADF images of AuNRs presented in A and C, respectively.

The electrostatic potential at a given position, $V(x,z)$, is a combination of the mean inner potential, V_{MIP}, and the potential from charge accumulation, V_{CP} (x,z) of the sample material. V_{MIP} is the volume-averaged potential due to incomplete screening of atomic cores and is defined as $1/\Omega \int V(\vec{r})\ d^3r$ (*68*), where $V(\vec{r})$ is the total electric potential at point $\vec{r}$ due to all the charges in the solid, Ω is the volume of the solid, and the integral is over the entire crystal volume. Thus, the phase shift $\phi(x)$ gradient observed in the hologram should originate either from thickness $\delta(x)$ or charge potential (V_{CP}) variation of the specimen. If our hypothesis is valid, the observed electrostatic asymmetry does not originate from $\delta(x)$ variation of the cylinder body but rather from V_{CP} variation. To determine the origin of this asymmetry, potential sources for such a slope have been thoroughly evaluated.

One potential cause of $\delta(x)$ variability along the long axis of the AuNR is the variation of the gold core diameter, ε. To evaluate this possible source of asymmetry, high-angle annular dark field (HAADF) scanning transmission electron microscopy (STEM) images were taken on the same AuNR (**Fig. 2.3 E, F**). Since the intensity of HAADF signal is proportional to ε, *i.e.* $I_{HAADF} \propto \varepsilon \cdot Z^{\alpha}$ where Z is the atomic number and $\alpha \approx 1.6 - 2.0$, the HAADF signal can be considered as ε profile and simply converted to $\phi(x)$ by using two constants, V_{MIP} of gold and C_E of a 200 kV electron beam (V_{MIP} = 30V, C_E = 0.00729 rad/V·nm) (*69*). Since the HAADF intensity profile shows no variability along the long NR axis, the estimated phase shift profile from the gold core is symmetric (**Fig. 2.3 B**, red). Similarly, direct visualization of the organic layer using secondary electron imaging and energy-filtered TEM (EF-TEM) shows no evidence

of CTAB patchiness variation on the long sides of the NRs (**Fig. 2.5**) that could be potentially another source of thickness variation of the NRs from carbon layer; which is also expected to have minor effect on EH images due to its relatively smaller V_{MIP} to gold.

The question arises now whether, the asymmetry of charge trapped in the facet defects or edges rather than CTAB, cause the loss of the central symmetry. Another possible artefact of similar nature, electron-beam-induced charging (*67*) should also be considered. One needs to remove the CTAB in order to test it. The complete removal of CTAB from dispersed AuNRs without losing colloidal stability is difficult (*70*, *71*). Therefore, we chose a different route and prepared a solid-state sample of AuNRs in a polymer matrix using layer-by-layer assembly (LBL). During LBL deposition, the rarefied layers of AuNRs anchored to the substrate by the previous polyelectrolyte stratum, are exposed to solution of poly(sodium 4-styrene sulfonate) (PSS). The negatively charged polyelectrolyte draws away and strips positively charged CTAB from surface of the NRs (**Fig. 2.11**). The removal is complete because PSS is present in the vast excess. Indeed, the annular electrostatic potentials disappeared from the holography image of AuNRs in the LBL matrix (**Fig. 2.3 C**) and the EH line profile of the phase shift (**Fig. 2.3 D**, blue) is now flat. Consequently, the $\phi(x)$ profile in **Fig. 2.3 B** reflects the actual potential gradient specific to charge accumulation in the CTAB-AuNR electronic system, V_{CP} (x,z), due to positive charge of the CTAB layer.

2.4 Asymmetric Capacitance Gradient of Gold Nanorods

Electrostatic fields around nanostructures can also be investigated by Kelvin probe microscopy (**Fig. 2.4**) which allows one to visualize the capacitance gradient, *dC/dz* related to $\phi(x)$ gradient with sub-nanometer resolution. The presence of the longitudinal gradient $\phi(x)$ can be independently confirmed by this technique. The *dC/dz* contrast relates to the dielectric permittivity (ε_r) being higher at locations with increasing permittivity (*72*). The contributions from several interfaces and materials, such as CTAB and gold, are manifested in *dC/dz* maps. The *dC/dz* map vividly shows the difference between the sides and ends of a NR, which should be attributed to different CTAB densities on the sides and ends (*62*, *63*, *73*). Importantly, consistent and large differences in *dC/dz* values *between the two ends*, *i.e.* for two dips in **Fig. 2.4 B**, are observed indicating electrostatic asymmetry of the NR ends. For statistical analysis of their differences, we performed a paired p-test for depths of the two dips for nine individual AuNRs. The difference is statistically considered extramurally significant based on the test result (**Fig. 2.4 D**, p value = 0.0002). Importantly, the dC/dZ profiles roughly matched the $\phi(x)$ of the charge potential (V_{CP} (x,z)) component which can be extracted from observed EH and HAADF profiles (**Fig. 2.4 C**).

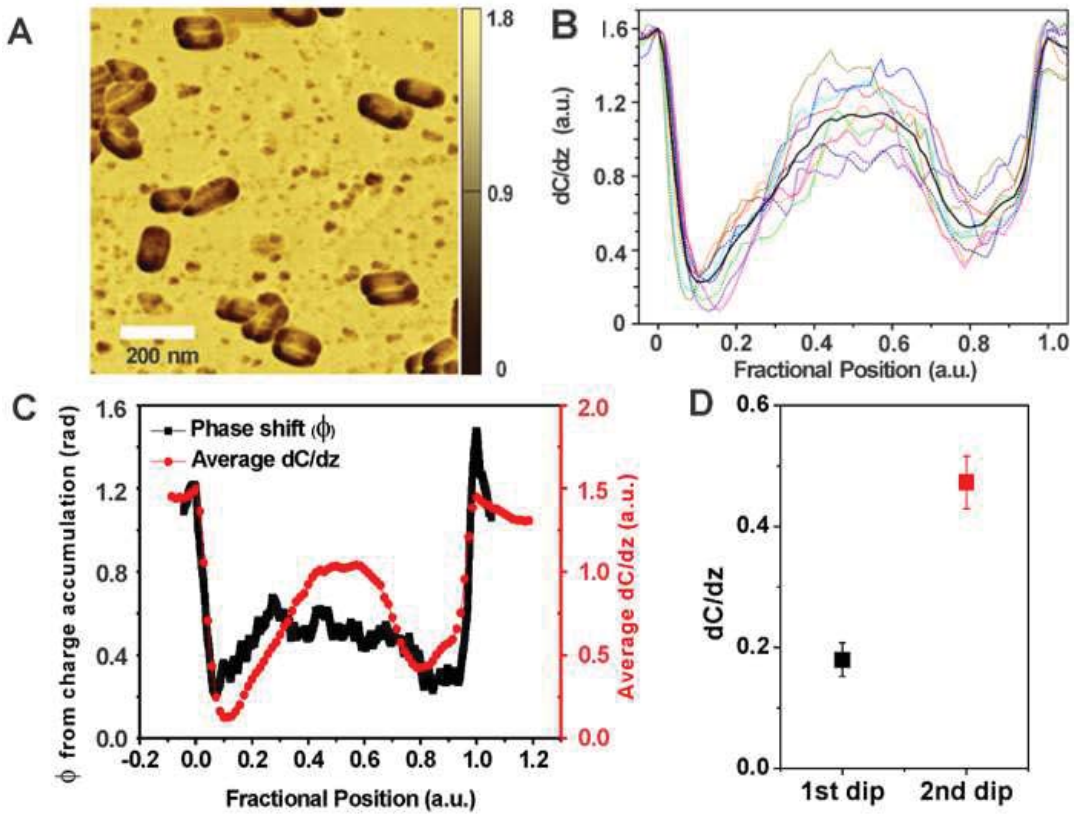

Figure 2.4 Analysis of capacitance gradient (dC/dz) profiles obtained by Kelvin probe microscopy. (**A**) Capacitance gradient (dC/dZ) image and (**B**) line profiles of individual (dashed) particles and average curve (solid, black) along long axis, obtained by Kelvin probe microscopy. (**C**) The phase shift caused by accumulated charge potential of AuNR (black) observed by electron holography and average dC/dz profile of AuNRs (red) taken by Kelvin probe microscopy. (**D**) Comparison of two dips shown in the capacitance gradient profile of individual AuNRs at their termini. Data represent mean ± SEM, n = 9. The difference is considered statistically significant with p value = 0.0002.

2.5 Uneven Distribution of Surface Ligand on Gold Nanorods

Being guided by the data described above, we acquired the direct evidence about unequal distribution of CTAB ligands on AuNRs. Aberration-corrected STEM with a secondary electron detector enables atomic-scale visualization of the CTAB layer. By comparing HAADF and SEM images of the same NR, one can see that the CTAB coverage on the two caps is different (**Fig. 2.5 A**, **B)**. Elemental mapping of carbon in the organic layer around the gold core by energy-filtered TEM (EF-TEM, **Fig. 2.5 C**) enabled quantitative analysis of CTAB density difference between two ends. Quantification of EF-TEM with the signal using a supporting carbon grid as the baseline showed that the NR has about 2.3 times more CTAB on one end than the other (**Fig. 2.5 H)**.

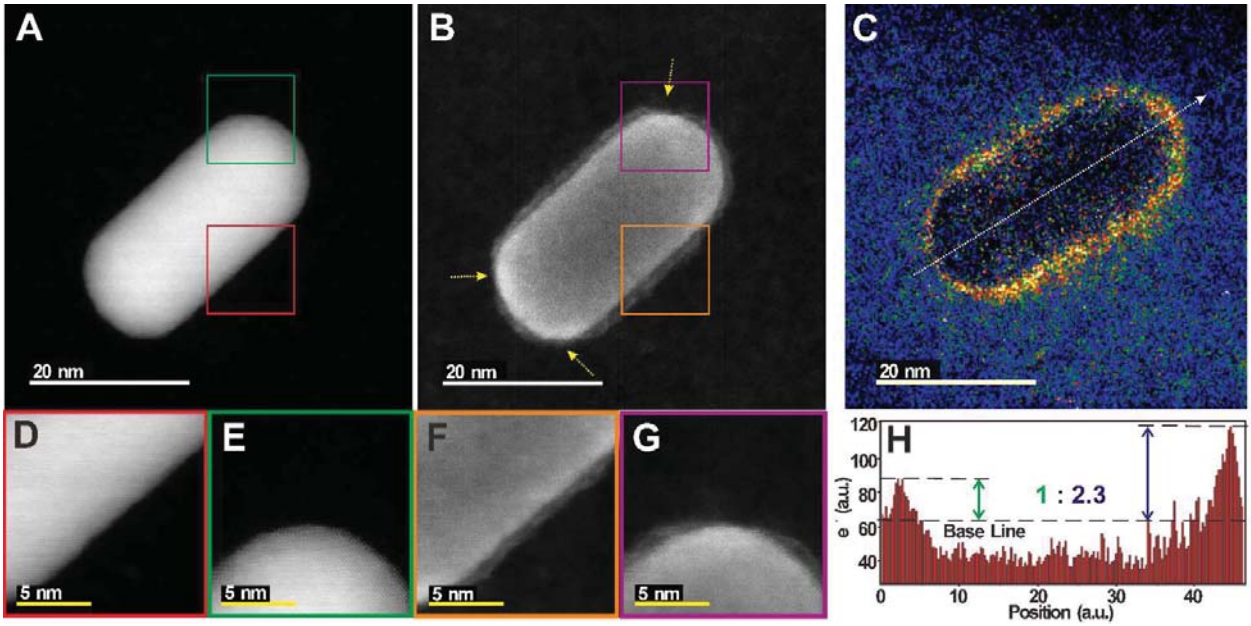

Figure 2.5 Non-centrosymmetric distribution of CTAB on AuNR. (**A, D, E**) STEM-HAADF and (**B, F, G**) SEM images of a same gold NR acquired simultaneously. (D-G) Atomic resolution images of the side (D, F) and end (E, G) sections of the Au NR. (**C**) Carbon element map and (**H**) carbon profile along the white arrow obtained by energy filtering (EF) TEM.

2.6 Study of Electrostatic Symmetry by Maxwell's Equations

The quantitative assessment of the unequal density of the CTAB layer at the termini of AuNRs (**Fig. 2.5 C, H**) enabled modeling of the asymmetrically charged NRs (**Fig. 2.6 A**). With an average surface charge density of the CTAB layer obtained via electrophoretic mobility measurement, electrical properties of NRs were computed by solving the stationary domain form of Maxwell's equations via finite element methods.

The surface and cross-sectional potential of the CTAB layer (**Fig. 2.6 C, D**) exhibits a spatial variation due to the asymmetric fixed surface charge on the CTAB layer (**Fig. 2.6 A)**. The profile of the calculated potential at the interface layer along the cylindrical body (**Fig. 2.6 C**) has a distinctive slope that matches the gradient $\phi(x)$ observed above (**Fig. 2.3 B**). The estimated voltage slope from their phase shift slope of 0.02 rad/nm shown in **Fig. 2.3 B** can be estimated to 0.11 V/nm since we confirmed that the phase shift gradient predominantly from charge potential gradient in the CTAB layer. This experimental electric field strength value is about doubled value of the calculated voltage slope shown in CTAB layer (0.049V/nm). Considering the fact that the hologram represents integrated potential through the short axis of AuNR, the observed and calculated results are accurately matched to each other.

Consequently, the asymmetric potential in organic shell must lead to a distinct surface charge polarization on gold surface to compensate the potential gradient. (**Fig. 2.6 E**). The maximum and minimum surface charge density on gold was calculated to be $7.9 \cdot 10^{-3}$ C/m^2 and –

$3.4 \cdot 10^{-3}$ C/m^2. By integration of surface charge density of gold core, the apparent "dipole" moment along longitudinal axis direction is calculated to be $2.4 \cdot 10^{-25}$ C·m, which corresponds to $7.2 \cdot 10^{4}$ *D*. Note, however, that NR "dipole" is fundamentally different from molecular dipoles. Unlike the latter there is no potential gradient in the metal core of the AuNRs due to the high polarizability of the metal and all potential drop occurs at the interfaces.

To test the validity of this model, the charge asymmetry of NRs with different aspect ratios was calculated and compared to the EH results. With a decrease in NR aspect ratio, the gradient of the potential linearly increased, although its absolute potential difference became smaller. The computed results matched the observed $\phi(x)$ data (**Fig. 2.6 F**).

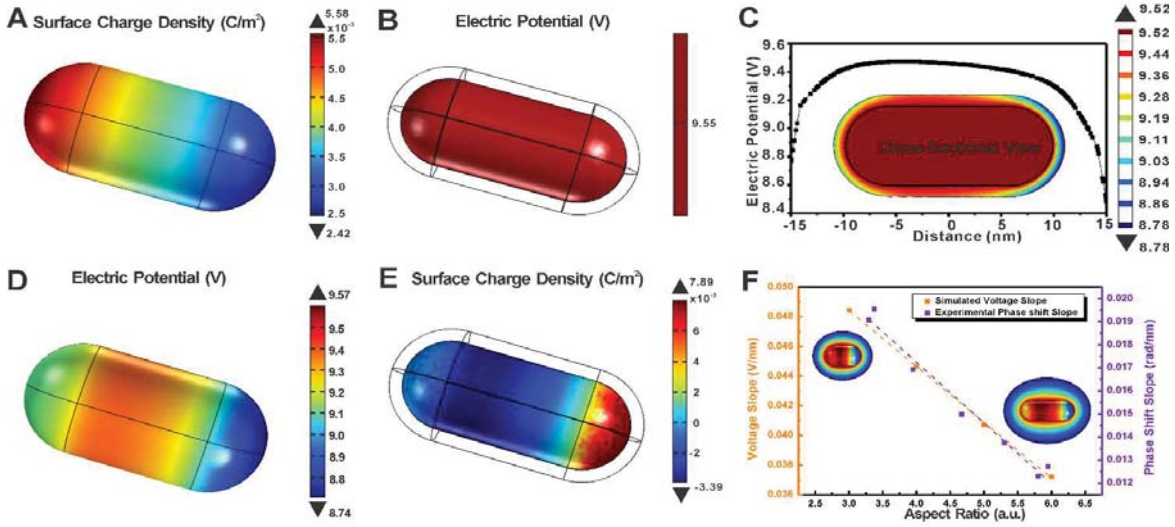

Figure 2.6 Computational analysis of electrostatic properties for AuNRs. (**A**) Surface charge density of CTAB layer. (**B, D**) Electric potential on surface of gold and CTAB layer, respectively. (**C**) Electric potential line plot in the CTAB layer and cross-sectional view of electric potential of CTAB-AuNR. (**E**) Surface charge density on surface of gold. (**F**) Voltage (orange) and phase shift (violet) slope of AuNRs with various aspect ratio obtained by computation and experimental electron holography data, respectively. Both values are linearly fitted as dashed lines with R square value of 0.999 (orange) and 0.971 (violet).

2.7 Asymmetric Optical Responses

2.7.1 Plasmon Mapping

In order to better understand the asymmetry observed during previous plasmon mapping (*46–48*), the electron energy loss was mapped in the 1.8-2.2 eV energy window, **(Fig. 2.7**, **Fig. 2.12 C**) which is associated with the longitudinal plasmon mode of AuNRs. Indeed, an EELS image also consistently showed asymmetry with brighter peaks on caps with smaller amounts of CTAB. As a control, we removed a part of the CTAB on the terminus with the denser surface ligand coating by focusing the electron beam for five minutes (**Fig. 2.12 A, B**). A distinct change in the EELS map, with plasmon intensity becoming symmetrical, was observed (**Fig. 2.7 C**). To quantify the degree of EELS asymmetry, the ratio between the two bright poles was obtained by integrating the intensity of 20 spectra from an area around the caps. (**Fig. 2.7 D**). The ratio change after *e*-beam treatment is turned to be statistically significant (p value = 0.015). These results indicate that the electrostatic asymmetry should be taken into consideration when interpreting EELS of metal nanoparticles.

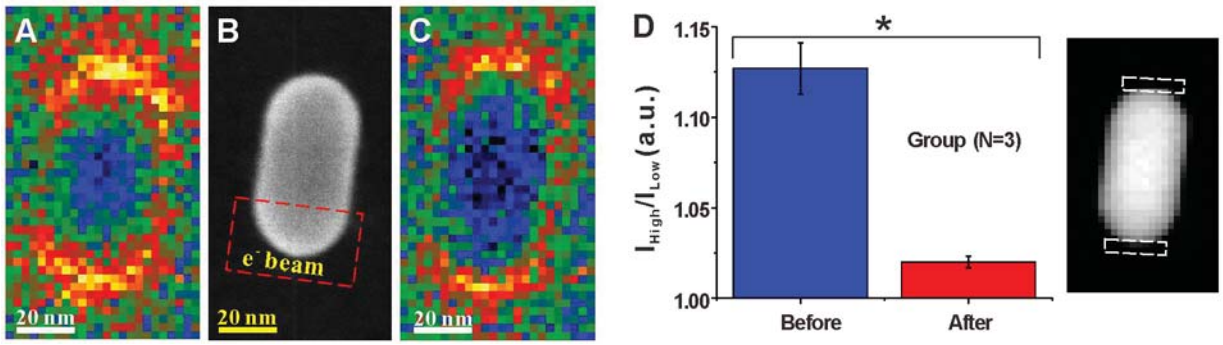

Figure 2.7 Asymmetry in plasmon mapping of AuNRs. (**A, C**) EELS mapping for the range of 1.8 eV-2.2 eV (longitudinal plasmon) before and after electron beam treatment, respectively. A paired t-test for these EELS data was performed; by conventional criteria, this difference of the intensity ratio between before and after treatments is considered to be statistically significant (p value = 0.015). (**B**) SEM image for the same AuNR with a red box indicating the area of electron beam ablation for 5 minutes. (**D**) Ratio between integrated intensities for two resonance poles before (blue) and after (red) electron beam treatment, respectively. Data represent mean ± standard error of mean (SEM), n=3. Integrated area is identified with white dashed box in image of AuNR (right).

2.7.2 Nonlinear Optical Activity

As we discussed earlier, conventionally, second-order NLO response is forbidden in materials for which the geometrical and material system retains centro-symmetry. The existence of the static dipole moments on the AuNRs shown here, however, can lead to break of inversion symmetry for the electrical system, which may rationalize strong SHG signal observed in the small seemingly centrosymmetric particles. To evaluate the population of AuNRs having optical asymmetry, we have prepared the dipolar Au NRs sitting on the cover glass in aqueous solution and recorded images in SHG and fluorescence (FL) mode simultaneously (**Fig. 2.8 A, B**). SHG of the dipolar AuNRs was exceptionally strong when they were excited at their longitudinal resonance, 850 nm, individual particle were vividly observable with a better noise-to-signal ratio compared to FL images (**Fig. 2.9**). The surprisingly strong signal to noise ratio of SHG imaging

at the near-infrared excitation also proposes that these dipolar NRs can be utilized as imaging contrast for biomedical imaging, where often the resolving small particle tracking is hampered by auto-fluorescence or penetration depth. The FL image can be used as a good reference to where individual AuNRs are located, thus enabling statistical analysis of population of AuNRs having optical asymmetry. The dominance of non-centrosymmetric Au NRs can be appreciated from the histogram describing the relative intensity of the SHG to FL for each individual NR. Although the SHG intensity varys, among the 119 of AuNRs identified with FL, 113 of AuNRs were found to exhibit SHG, which indicates that 95% of Au NR lack central symmetry.

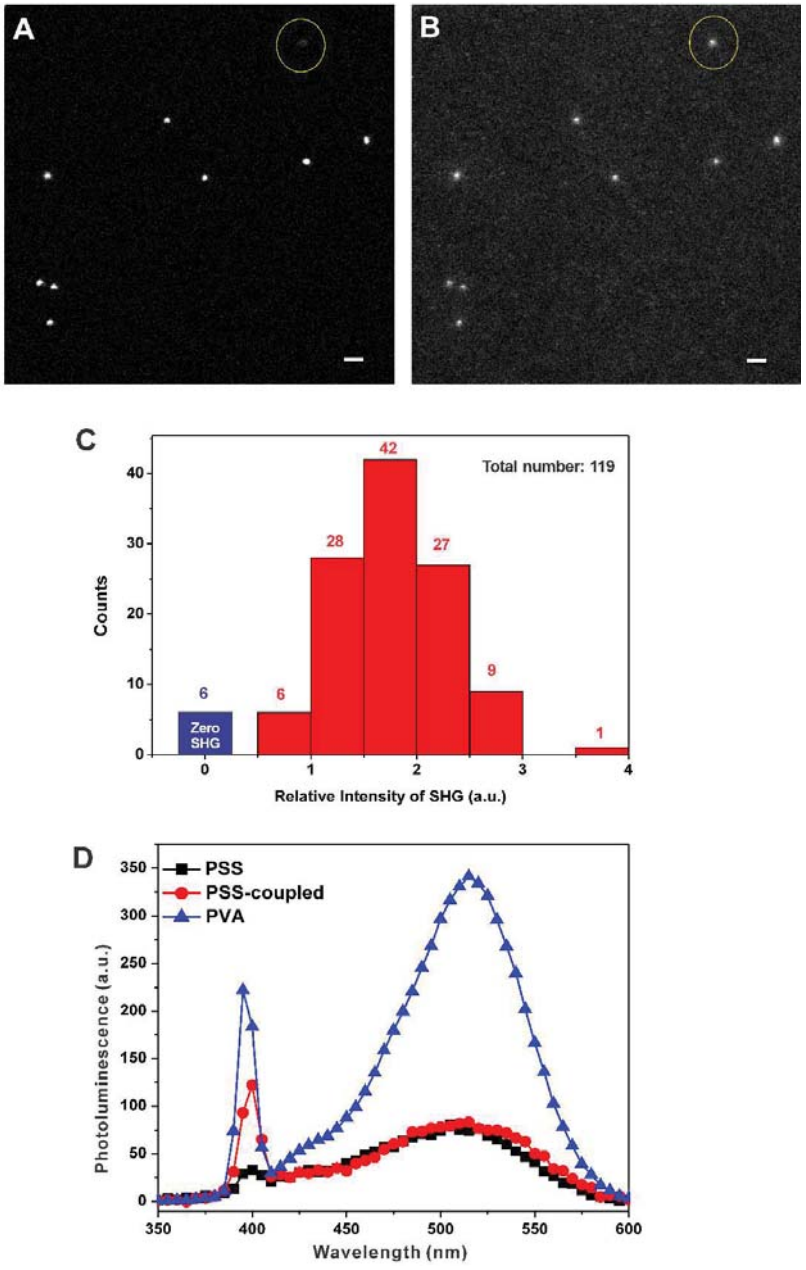

Figure 2.8 Asymmetrical optical properties of AuNRs. (**A, B**) Comparison of simultaneously obtained SHG and fluorescence images of AuNRs. Max intensity projection of same z stacks of SHG (A) and fluorescence (B) with same gray scale. (**C**) Histogram of relative intensity of SHG compared to fluorescence from 119 of individual AuNRs. Note that blue colored bar represents AuNRs having zero intensity. (**D**) Nonlinear photoluminescence from AuNRs embedded in PSS (black: decoupled; red: coupled) and PVA (blue) matrix.

To investigate the NLO properties in the context of electrostatic asymmetry of AuNRs, we prepared optically transparent films containing AuNRs with and without electrostatic asymmetry. In both cases, care was taken to avoid formation of NP pairs and other assemblies that could lead to transient asymmetry of coupled plasmons. The film containing asymmetrical AuNRs was made by drop-casting AuNR dispersions in uncharged poly(vinylalcohol) (PVA). The conserved CTAB layer on the AuNRs within this film was confirmed by X-ray photoelectron spectroscopy (XPS) (**Fig. 2.11 B**). The average distance between AuNRs in these films was 300 nm; these gaps, greatly exceeding the AuNR dimensions, are sufficient to decouple transient oscillating electrical dipoles. Another type of films containing symmetric AuNRs were made using LBL with negatively charged PSS polyelectrolyte, as described above **(Fig. 2.3 C** and **Fig. 2.11 A)**. In this case, films with both optically coupled and decoupled AuNRs were prepared by varying the distance between subsequent AuNR layers using spacer layers.

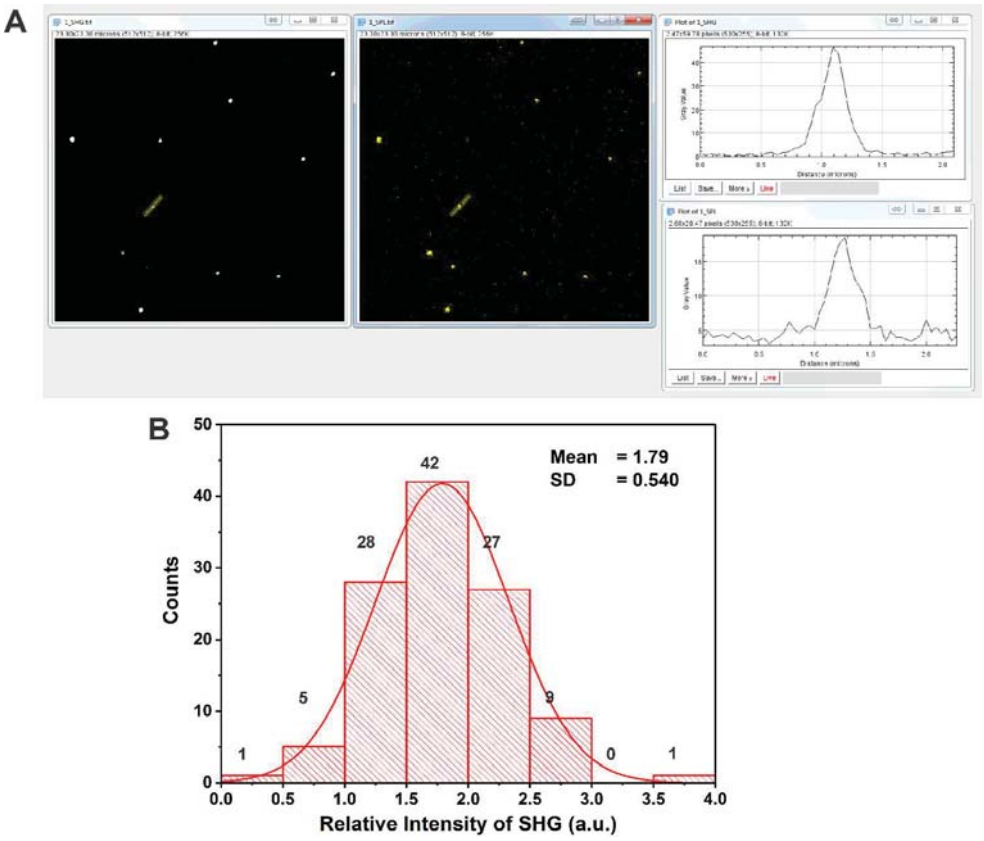

Figure 2.9 Intensity of individual AuNRs in SHG and FL mode imaging. (**A**) Signal-to-noise ratio difference between SHG and FL images of AuNRs. (**B**) Distribution analysis of relative SHG intensity to FL. No significant departure from normality was found in normality test (p value =0.078 > 0.05)

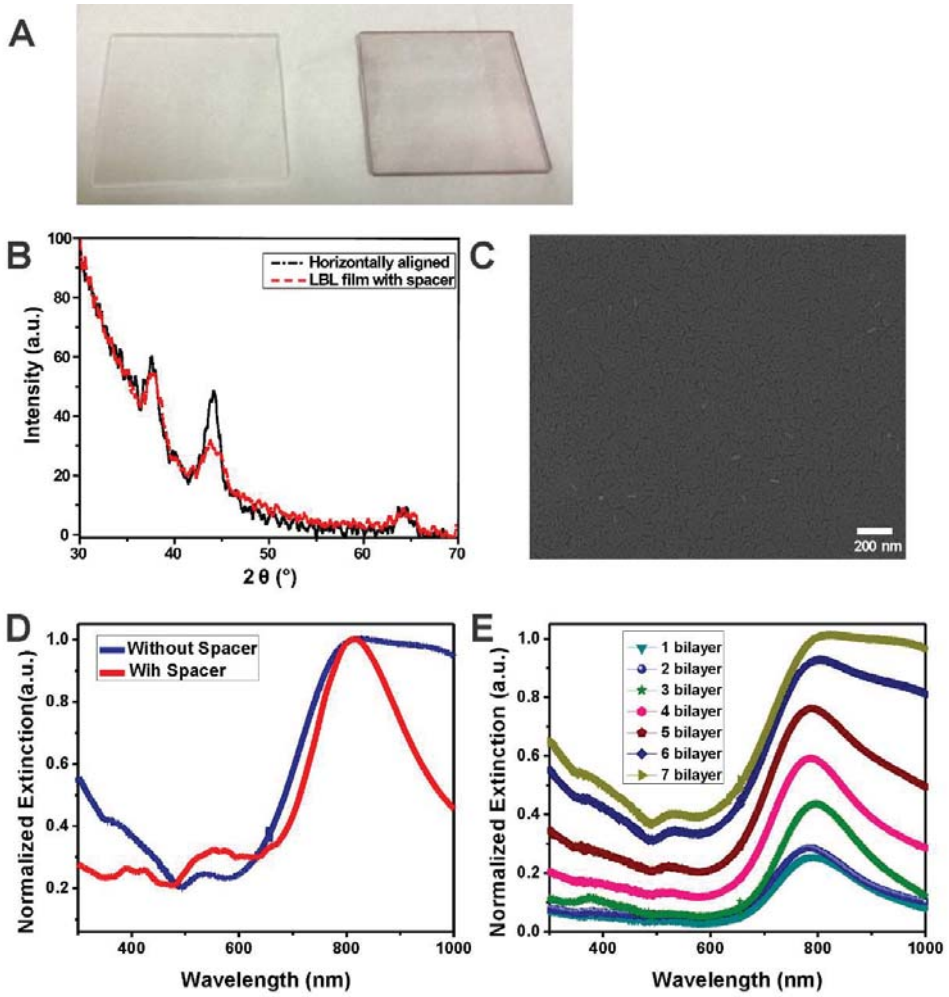

Figure 2.10. Layer-by-layer assembled AuNR/PSS films (**A**) Sample picture of decoupled AuNR composite and reference polymer film on quartz slides. (**B**) Grazing incident X-ray diffraction (GiXRD) measurement of decoupled AuNR composite and spin-coated AuNR quartz slides. (**C**) SEM image showing top-view of decoupled AuNR composite film. (**D**) UV-vis spectra of AuNR composite film with/without spacer. (**E**) UV-vis spectra change of coupled AuNR composites by addition of AuNR/PSS bilayers.

NLO properties of these samples were evaluated using high intensity 800 nm 100-femtosecond pulses, resonant with the longitudinal plasmon of the AuNRs. The two main nonlinear optical effects, second harmonic generation (SHG) and non-linear photoluminescence (NPL), can be

clearly seen for AuNRs imbedded in a PVA matrix at 400 nm and 530 nm, respectively (**Fig. 2.8 D**, blue). In contrast, the AuNRs imbedded in PSS with a PAA/PDDA spacer show weak or no SHG intensity at 400 nm and strong suppression of NPL (**Fig. 2.8 D**, black).

The second-order NLO response in centrosymmetric particles has been attributed to either surface or retardation effects (*58*). Since we have used same batch of AuNRs for both PVA/AuNR and PSS/AuNR films, the observed suppression of the SHG signal in PSS/AuNR films cannot be explained with such effects. Instead, SHG in these systems should be, at least in part, attributed to the second order nonlinear susceptibilities χ^2 arising from the breaking of inversion symmetry of AuNRs by the longitudinal electrostatic polarization. The electrostatic asymmetry also can be one of the overlooked factors influencing NPL, giving us a fresh look for previously puzzling NPL behavior (*59*, *74*). The even modes NPL emission can be mediated by this built-in electrostatic field in AuNRs (*55*, *75*). We found that removal of CTAB results in strong suppression of NPL (**Fig. 2.8 D**).

Some contribution to SHG may come from hybridized plasmon modes of multiparticle non-centrosymmetric assemblies, even though individual AuNRs are centrosymmetric. These expectations were indeed confirmed in the closely spaced LBL films that produce such assemblies (**Fig. 2.8 D**, red). Notably, the SHG peak by assemblies is enhanced while NPL remains the unchanged. This suggests that SHG and NPL can be 'tuned" independently when we take AuNR asymmetry into consideration.

2.8 Conclusion and Outlook

AuNRs are electrostatically non-centrosymmetric despite the appearance of the nearly perfect central symmetry in TEM images. While the electrostatic potential in the metal body remains flat (**Fig. 2.6 B**), the consistently uneven distribution of CTAB between the two ends leads to the gradient of the electrostatic potential at their surface, and therefore surface of gold is highly and unequally polarized on the two ends (**Fig. 2.6 E**). This origin of the asymmetry is consistent with normal distribution of relative SHG intensity in **Fig. 2.9 B** reflecting, among other factors, variability of the CTAB on the two ends of the NR. The reason for end-asymmetry of the AuNRs is likely to be associated with the dynamics of NR growth and slow reconstruction of the CTAB shell (*70*, *71*). In any case, the structural inequality between the two ends is not an aberration characteristic of singular NRs but a property-determining feature characteristic of their ensembles, as demonstrated by the strong non-linear optical activity. The unexpected lack of inversion symmetry of the AuNRs can be extended to other nanocolloids carrying surface ligands, in addition to the asymmetries originating from crystallography (*76*, *77*) and truncations.(*78*) The intrinsic electrostatic field gradient was also observed in semiconductor nanostructures (*79*, *80*). The estimated surface polarization of AuNR, however, has a five times higher polarity than same size wurtzite phase zinc oxide nanorods (*79*). The presence of surface charge asymmetry should be explored in relation to optical properties (*81*, *82*), electrical properties (*11*, *83*), and agglomeration behavior (*84*, *85*). For example, the electrostatic asymmetry of AuNRs and potentially other nanostructures emerging from this study shows a new pathway to explain and, therefore, control NLO properties. Besides NLO, the lack of

central symmetry is expected to play a role in, and be further exploited through, self-organization phenomena, including dissipative systems (*9*), chiral nanostructures (*86*), and catalysis (*51*).

2.9 Materials and Method

2.9.1 Materials

Gold chloride trihydrate ($HAuCl_4$, Cat.# 520918), silver nitrate ($AgNO_3$, Cat.# 204390), trisodium citrate dihydrate (Cat.# S4641), sodium borohydride ($NaBH_4$, Cat.# 480886), poly(sodium 4-styrenesulfonate) (PSSS, Mw = 1,000,000, Cat.# 434574), Poly(vinyl alcohol) (PVA, Mw=85,000-124,000, Cat. # 363146), Poly(diallyldimethylammonium chloride) solution (20 wt.%, Cat# 409014), cetyltrimethylammonium bromide (CTAB, Cat# H9151) and ascorbic acid (Cat.# A7506) were purchased from Sigma-Aldrich (Milwaukee, WI). The quartz slides (Prod # 26013) and ultrathin carbon film on lacey carbon support film, 400 mesh, copper grids (Prod # 01824) were purchased from Ted Pella (Redding, CA). Non-Porous Pure Silicon 5 nm thick TEM windows (Cat.# US100-A05Q33A) were purchased from TEMwindows.com. Ultrapure water from a Direct-Q3 system (18.2 MΩ·cm, Millipore; Billerica, MA) was used in this work.

2.9.2 Synthesis of gold nanorods (AuNRs)

AuNRs were prepared using a slightly modified literature method (*87*). Assisted by the surfactant CTAB, the seed-mediated growth of AuNRs occurred in aqueous solution. Briefly, an aqueous solution of $HAuCl_4$ (0.25 mL, 0.01 M) was added to the CTAB stock solution (9.75 mL,

0.1 M). After gentle mixing, a freshly prepared ice-cold $NaBH_4$ solution (0.6 mL, 0.01 M) was added with vigorous stirring. A brown seed solution was obtained after 2 min, and the seed solution was aged for 2 hours. AuNRs were grown by the injection of $HAuCl_4$ (0.4 mL, 0.01 M), various amounts of $AgNO_3$ (20-100 µL, 0.01 M), ascorbic acid (48 µL, 0.1M), and seed solution (9.6 µL) to the CTAB stock solution (8 mL, 0.1 M) in sequence. The solutions were gently mixed after each addition. The final mixture solution was kept without disturbance for 24 hours to ensure full growth of gold nanorods. Note that all reactions and aging were performed at a temperature of 30 ºC. The samples were purified by centrifugation (12000 rpm, 10 min) three times and redispersed in water.

2.9.3 Electron microscopy analysis

All electron microscopic investigations were done using a JEOL ARM 200CF apparatus equipped with a cold field-emission gun and double spherical-aberration correctors at the Brookhaven National Laboratory.

Sample preparation: Unmodified gold nanorod (CTAB-AuNR) samples were prepared by typical drop casting methods. The redispersed corresponding solution after synthesis was purified two times more with a 100 kDa centrifugal device (4000 rpm, 10 min), to remove excess CTAB in solution, and drop cast 5 µL of solution on thin carbon and pure silicon grid, respectively. Layer-by-layer (LBL) CTAB-AuNR samples were prepared by using poly (sodium 4-styrenesulfonate) (PSS) using previously-described LBL techniques to investigate the electrostatic properties of AuNRs as different electronic environments (*88*). Bilayer ultrathin

composite films composed of PSS and purified CTAB-AuNRs were fabricated on carbon and pure silicon grids, respectively. Note that electron holography, STEM HADDF, and EELS analysis was conducted with silicon grid samples whereas SEM and EF-TEM imaging was performed on the carbon grid samples in order to improve image resolution.

Off-axis electron holography: Holograms of AuNRs on the pure ultrathin (5 nm) silicon grid were acquired using the JEOL ARM 200CF as described above operated at 200 kV equipped with a biprism. Phase images were reconstructed using custom Gatan Digital Micrograph scripts (source code is available on request). The phase profiles presented in **Fig. 2.3 A** and **C** were calculated in Gatan Digital Micrograph using the line profile tool.

STEM HAADF: Atomic-resolution scanning transition electron microscopy has been used on the same silicon grid samples when holographic images are obtained simultaneously. All STEM measurements were performed with 200 kV electrons and collection angles for high-angle annular-dark-field (HAADF) detectors ranged from 68 to 280 mrad.

High-resolution SEM: A nanometer resolution SEM image has been acquired by utilizing a secondary electron detector in a high-resolution STEM. For better resolution images, which clearly show the CTAB layer around the AuNRs, samples on ultrathin carbon grids were used for analysis.

Energy Filtered-TEM (EF-TEM): For quantitative analysis of the variation of the CTAB layer around the AuNRs, we obtained EF-TEM images for individual AuNRs. The investigations were performed using the three-windows method (*89–91*); background subtraction was achieved

by using two images recorded by selecting two energy windows immediately before (pre-edge 1 and 2) the ionization edge and one image by selecting an energy window immediately after (post) the ionization edge. Since the pre- and post-edge images are acquired sequentially, the background subtraction algorithm accounts for specimen drift that occurs during the collection process.

2.9.4 Kelvin probe microscopy imaging of AuNR

Electrostatic fields around nanostructures were investigated by Atomic Force Microscopy with a scanning probe microscope NEXT (NT-MDT) and conducting Pt-coated Si probes of NSG-30/Pt type (NT-MDT). The AuNR solution was purified two times more as described in electron microscopy sample preparation section and drop-casted on a highly oriented pyrolytic graphite (HOPG) substrate. The map of capacitance gradient, *dC/dz*, of NRs has been achieved in single-pass technique using the probe response at 2^{nd} harmonic of 3 kHz frequency, at which electrostatic probe-sample force was stimulated (*72*).

2.9.5 Computational Analysis for Electrostatic Properties of AuNR

Theoretical calculation of electrostatic properties of AuNR was performed based on our hypothesis using the computing tool COMSOL Multiphysics. To account for the polarizability of a conductive particle with fixed surface charge, we treat gold as a dielectric with relative dielectric constant of 12000, much greater than that of the surrounding CTAB layer. We postulated that the potential on the gold surface is constant by adding a floating potential on the

gold surface (**Fig. 2.6 B**). With this approximation, the electrostatic potential, V, inside the AuNRs should obey the Laplace equation ($\nabla^2 V = 0$).

Estimation of average surface charge distribution on CTAB-AuNRs: Combining the experimental information obtained by EF-TEM and a zeta potential analyzer, we can estimate the surface charge distribution from CTAB. Due to the elongated structure of AuNRs, the zeta potential, generally used for estimation of surface charges of particles, cannot be used. Instead, we assumed that AuNRs are prolate spheroids (principle radii a and c, with c > a) and calculated their average charge density with their regulated geometrical factor, g(R), from their electrophoretic mobility experimentally obtained using a Malvern ZetaSizer.

The measured zeta potential and mobility of AuNRs were 36.3 mV and 2.847E-8 m^2/Vs, respectively. A relationship between effective mobility (μ_{eff}) and surface charge density (σ), regulated with geometrical factor g(R), can be described as such (*92*):

$$\mu_{\text{eff}} = (2a\sigma/3\eta) * g(R),\ g(R) = 1/4R^2 \cdot \left(R\sqrt{1-R^2} + \sin^{-1}(R)\right)\ln\left(\frac{1+R}{1-R}\right) \qquad \text{(Eq. 2.2)}$$

where R is the ellipticity of the modeled AuNR $\left(\sqrt{1 - a^2/c^2}\right)$ and η is the media viscosity. By determining the measured mobility of 2.847E-8 m^2/Vs for the batch of AuNRs, the mean surface charge density was determined to be 0.004 C/m^2. Since carbon concentration has a linear relationship with EF-TEM intensity, we could obtain information about the relative coverage of CTAB on the AuNRs; one end of a AuNR has 2.3 times more CTAB than the other (**Fig. 2.5 H**). We applied a linear charge distribution for the NR model (67234 x[m] + 0.004 C/m^2), retaining

average charge density with the 1 : 2.3 charge charge ratio between two ends observed in EF-TEM taken into consideration (**Fig. 2.6 A**).

Electrostatics Simulation: The structure, size, and electrostatic boundary conditions of CTAB-AuNRs are assigned based on experimental findings. The AuNR and its CTAB layer was modeled as a cylinder (width: 17 nm and length: 30 nm), end-capped with hemispheres (diameter:17 nm), and as an additional surface layer (thickness: 4 nm), respectively. Under static conditions, the electric potential V is defined by the equation $E = -\nabla V$. Combining this equation with the constitutive relationship between the electric displacement D and the electric field E, $D=\varepsilon_0\varepsilon_r E$, it is possible to represent Gauss' law ($\nabla(\varepsilon E)= \rho$) as a variant of Poisson's equation: $\rho = -(\varepsilon_0\varepsilon_r\nabla V)$

2.9.6 EELS imaging of AuNRs before/after e^- beam treatment

A light e^- beam shower (3 min) was applied to the sample to prevent hydrocarbon growth during collection of the EELS spectrum; this treatment may slightly reduce the overall CTAB density on AuNRs but did not remove its asymmetry. An EELS spectrum was obtained for every 1x1 nm point in the STEM image and signal intensities for 1.8-2.2 eV energy window were extracted to map the longitudinal plasmon mode of the AuNR. After taking the first plasmon map, SEM images of each particle were taken to find the end bearing excess CTAB. The e^- beam was focused on the end with excess CTAB to homogenize the CTAB distribution. This step resulted in a decrease of the overall density of CTAB but larger amount at the focused area (**Fig. 2.12 A, B**).

2.9.7 SHG and FL imaging of AuNRs

10uL of AuNR solution was dropped on a glass slide and was as flipped for 15 mins to stabilize NRs sitting on the cover glass. Sequential images in SHG and FL mode were taken by using 850 nm pulsed multiphoton and 405 nm UV laser sources with Confocal laser scanning microscope Leica TCS SP8 . From the sets of images obtained in two different modes, relative SHG intensities of individual AuNRs were calculated by dividing the integrated SHG with integrated FL using the particle analysis tool of ImageJ.(*93*)

2.9.8 Sample preparation of charge-asymmetric and symmetric AuNR composite films

To realize a random directionality, sufficient optical density, and controlled inter-particle spacing of AuNRs in the sample, we prepared AuNR composite films on quartz slides by two different methods. To prepare asymmetric AuNR samples, as polymer matrix we chose an uncharged polymer, poly(vinyl alcohol) (PVA), which has been proven to have almost negligible affinity to the surface of gold. The detailed information of their affinity to gold surface is followed in ligand exchange experiment section below. The symmetric AuNR samples are prepared by the layer-by-layer (LBL) method using poly(styrene sulfonate) (PSS) with/without spacers of poly(acrylic acid) (PAA) and poly(diallyldimethylammonium chloride) (PDDA). PVA/AuNR film samples (asymmetric AuNRs) were simply prepared by drop casting 1 OD of AuNR colloids redispersed in PVA (7.5 wt%) onto quartz slides (*94*). To prepare LBL AuNR films (symmetric AuNRs), 1 mm thick quartz slides were treated with piranha solution, pre-coated with one PAA/PDDA layer and finished with one PSS layer. For both coupled and

decoupled LBL samples, two bilayer of AuNR/PSS layer were deposited first. For a coupled LBL sample, five more bilayers of AuNR/PSS were simply added for coupled AuNR film (**Fig. 2.7 E**). For the decoupled LBL samples, however, three bilayers of PAA/PDDA were added as spacers between every two bilayer of AuNR/PSS. PDDA and PSS layer were put to make positive and negative charge before adding spacers or bilayers of AuNR/PSS, respectively. The six bilayers of AuNR/PSS were deposited in total. Reference films were made for each film with only polymer or polyelectrolyte components of the corresponding samples. For example, 0.5 mM pure CTAB solution was used for the AuNR deposition step.

2.9.9 Measurements of NLO properties of AuNR/PSS LBL and AuNR/PVA films

The excitation source was a Ti:sapphire mode-locked laser which delivers fs pulses with a repetition rate of 76 MHz at 800 nm. The excitation power was controlled by a programmable attenuator to study the intensity dependence. The beam was focused into the AuNR film on quartz slides, which contained AuNRs of diameter 25 nm and length 102 nm and resonant at 808 nm. Light scattered at 90^{o} from the excitation beam was filtered through a monochromator and detected using photon counting. The optical signal was collected by a side lens, sent to a spectrometer and then detected by a single-photon-counting photomultiplier to study the spectral features. The gated photon counting technique was applied.

2.10 Supplementary Information

2.10.1 Computational Analysis of Plasmon Mode Shift from Local Environment

Different plasmon modes of silver nanowires (AgNWs) were computed using the wave-optics module of COMSOL Multiphysics 5.1. The model was constructed based on the actual size of the silver nanowire (width: 15 nm and length: 375 nm) shown in previous literature (8). A series of plane-polarized electromagnetic waves traveling perpendicularly into the long axis of the AgNWs were applied to calculate electric fields of plasmon modes of NWs with/without spherical particles located along the long axis with a 20 nm gap. The shifts of the plasmon center by the neighboring spherical particle are negligible for all modes (from 500 nm to 1500 nm with 250 nm intervals, Extended Data Fig. 1a and b), and therefore suggest that the significant mode shift observed in the literature (17 nm) is unlikely to be generated by the local environment. We only observed a small intensity asymmetry for higher plasmon modes (wavelength = 500 nm, **Fig. S1C**).

2.10.2 Element Analysis of AuNR after Ligand Exchange of CTAB with PSS and PVA

To investigate the affinity of PSS and PVA on a gold surface during film sample preparation for optical property measurement, we examined the yield of CTAB ligand exchange for PSS and PVA as colloids. The concentrated CTAB-AuNR solution (3 OD) after the purification step was redispersed in 1 mL of 2 wt% PSS and PVA solutions, respectively. After 30 min stirring in room temperature, the solutions were centrifuged down (8000 rpm, 25 min) and redispersed in

DDI water. After 3 minutes vigorous stirring, the solutions are re-centrifuged down (4000 rpm, 10 min) and redispersed in 100 μL of DDI water to obtain purified concentrated AuNR solutions.

The concentrated solution was drop-cast on indium foil for X-ray Photoelectron Spectroscopy (XPS) analysis. The spectrum mode using the monochromated Al source was used to survey the energy range from 0 to 600 eV with energy resolution ~0.5 eV using a Kratos Axis Ultra X-ray photoelectron spectrometer (Michigan Center for Materials Characterization at University of Michigan). The AuNRs collected from PSS solution had negligible nitrogen peaks (**Fig. 2.11 A**), which proves chemically that the CTAB layers on the AuNRs had been effectively removed during the LBL process with PSS. In contrast, the sample from PVA had a nitrogen peak (**Fig. 2.11 B**), which indicates that only a passivation had occurred in PVA solution with a continued presence of CTAB layer on gold. Thus, we can conclude that the CTAB layer of AuNRs is preserved in PVA/AuNR composites, maintaining the asymmetric charge distribution.

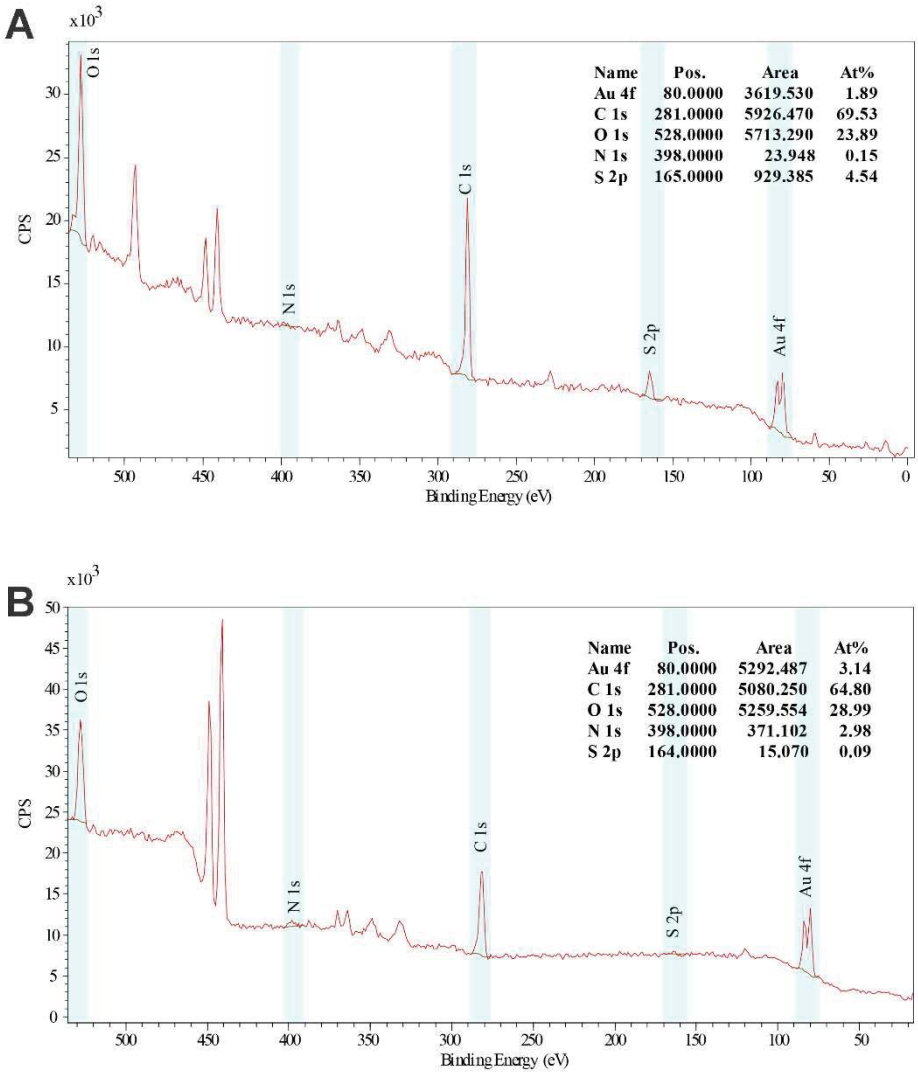

Figure 2.11 Ligand exchange of CTAB on AuNRs with PSS and PVA. XPS spectra of purified AuNRs after being dispersed in highly concentrated PSS (**A**) and PVA (**B**), respectively.

2.10.3 Orientation of AuNRs in film samples

The orientation of AuNRs in a polymer matrix could be one of the factors for the efficiency of nonlinear optical properties due to different likelihood of resonance or retardation. For instance,

if all AuNRs are parallel to the surface of the quartz slide, thus perpendicularly oriented to the incident beam direction, the retardation effect would be minimized, and depression of SHG is not surprising in this case. To confirm that our observation of SHG depression shown in **Fig. 2.8 D** is not caused by the arrangement of AuNRs, we analyzed a grazing incident X-ray diffraction (GiXRD) pattern (**Fig.** S**4B**) of a PSS/AuNR composite film.

GiXRD patterns from film samples were obtained using a Rigaku Ultima IV X-Ray diffractometer. To prepare the nearly horizontally-aligned AuNR sample, the bare AuNR colloid was spin-coated on a quartz slide. The same PSS/AuNR and reference samples for which we measured nonlinear optical responses were used to obtain their GiXRD patterns. All measurements were taken at 40 kV and 44 mA.

Compared with the GiXRD pattern of horizontally aligned AuNRs, AuNRs embedded in a PSS LBL matrix with spacer show weaker relative peaks for the side facet of AuNRs (200).(**Fig. 2.10 B**) This proves that the AuNRs in the LBL matrix are not horizontally aligned, thus depression of SHG cannot be attributed to the lesser retardation likelihood of AuNRs in the film. The direct observation of the surface of the PSS/AuNR film by SEM imaging also indicates the existence of AuNRs having almost perpendicular orientations to the quartz substrate (**Fig. 2.10 C**).

2.10.4 CTAB removal test with electron beam treatment

To investigate how a focused electron beam (*e* - beam) removes the CTAB layer, the intensity of SEM for a thick CTAB deposition area with exposure time to the e^- beam of 10 min was

recorded (**Fig. 2.12 D**). 10 min of e^- beam treatment removed approximately 20 percent of the CTAB, thus demonstrating the partial removal of CTAB on AuNRs by *e* - beam processing.

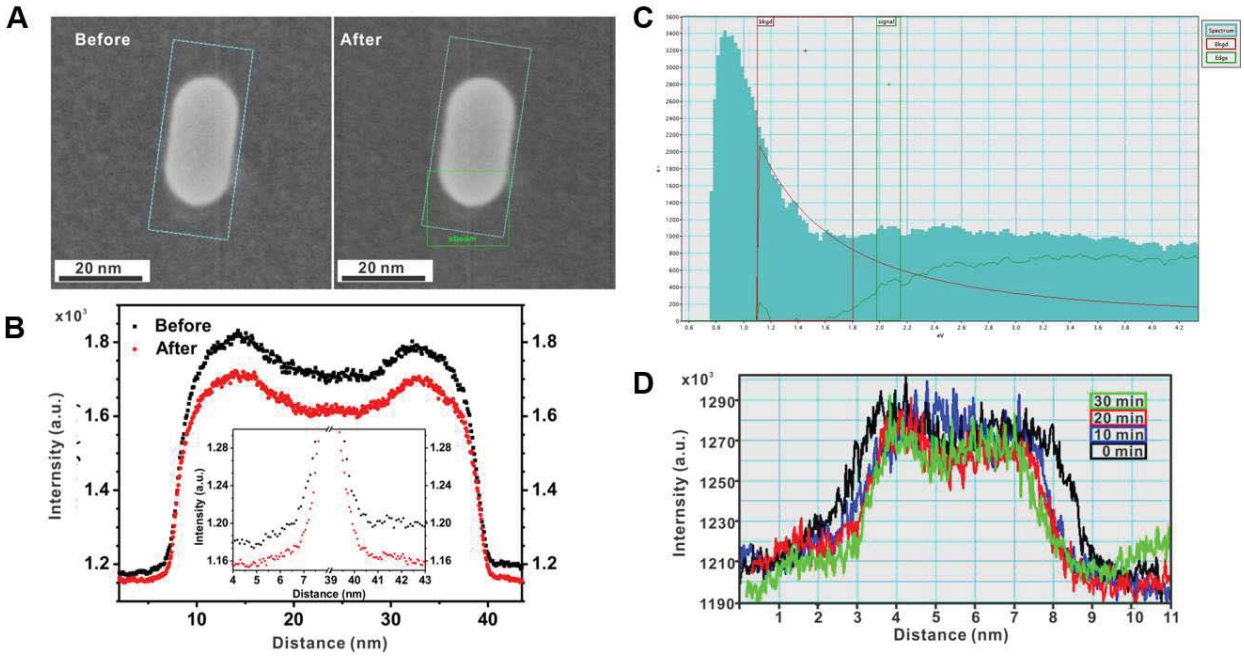

Figure 2.12 Electron beam (e-beam) ablation for selective removal of CTAB on single AuNRs. (**A**) SEM images and (**B**) intensity line profile of AuNRs (for light blue box area, with direction from top to bottom) before/after e-beam ablation (**C**) Example of EELS spectrum used for plasmon map constructuction. (**D**) SEM intensity profile difference of highly concentrated CTAB bridges between two AuNRs for different durations of e-beam ablation.

2.10.5 Computational Analysis of Plasmon Mode Shift from Geometrical Asymmetry

We commutated plasmon intensities ratio changes derived by geometrical asymmetry to examine if the intensity asymmetry observed in EELS map can be considered significant. We constructed two model of AuNRs with perfect centrosymmetry and asymmetry with the eccentricity of 0.6, and computed their plasmon map at the longitudinal resonance condition using Lumerical FDTD solution (**Fig. 2.13**). Even with this significant geometrical asymmetry, the integrated intensity

ratio of the same area was found to be about 8 %, smaller than observed in EELS experimental result. Moreover, our plasmon map computation with an adjunct particle (**Fig. 2.1**) also showed that local environment cannot rationalize the observed asymmetry. We believe that there must be a major contribution of electrostatic asymmetry by CTAB patchiness to this plasmon asymmetry, possibly 10 % out of 12.5 % considering corrected intensity ratio after e-beam treatment.

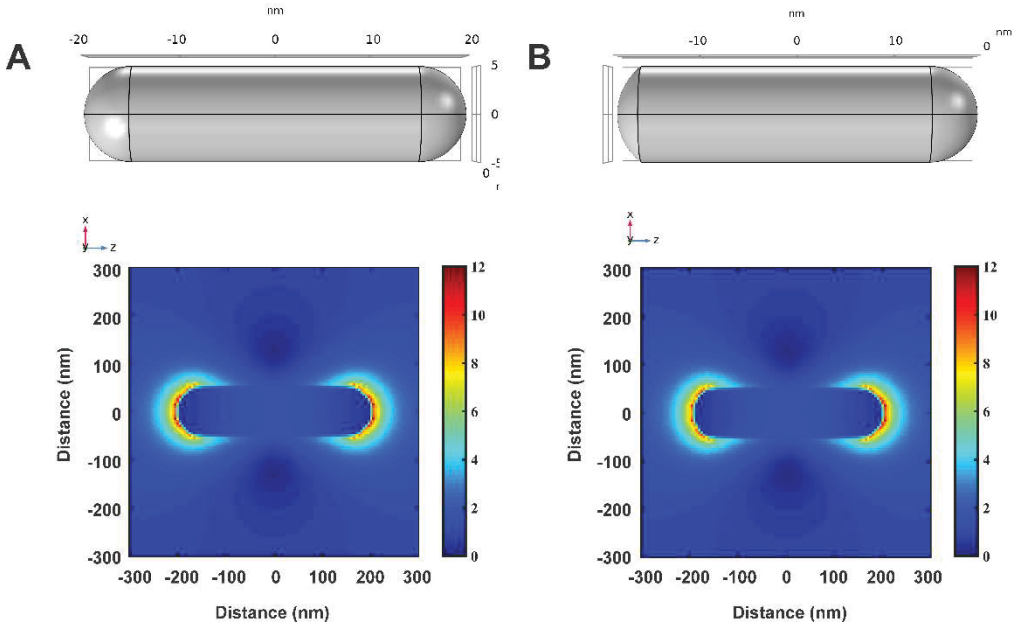

Figure 2.13 Computation of plasmon modes of AuNRs with and without centro-symmetrical gold core geometry. (**A**) Plasmon map (bottom) at resonance condition, 808 nm, with perfect centro-symmetric AuNR model (top). (**B**) Plasmon map (bottom) at resonance condition, 808 nm, with asymmetric AuNR model with one end cap having the eccentricity of 0.6 (top).

Chapter 3 Optical Asymmetry and Nonlinear Light Scattering of Gold Nanorods

Reprinted with minor modifications with permission from Lien, M.-B.; Kim, J.-Y.; Han, M. –G.; Chang, Y.-C.; Ferguson, H. J.; Zhu, Y.;Herzing, A. A.; Schotland, J. C.; Kotov, N. A.; Norris, T. B., "Optical Asymmetry and Nonlinear Light Scattering from Colloidal Gold Nanorods." *ACS Nano* **11**, 5925-5932 (2017). Copyright 2017 American Chemical Society.

Contributions: Norris, T. B. conceived the project. Under the guidance of Zhu, Y. and Kotov, N.A., Kim, J.-Y. and Han, M. -G. took off-axis electron holography and evaluate the electrostatics data. Lien, M.-B. prepared the samples to be characterized and developed the model. Ferguson, H. (George, H.) and Lien, M.-B. performed the optical experiments. Schotland, J. C. helped evaluation of the model by computation. Kim, J.-Y., You-Chia and Yu-Chun contributed on the physics discussion to develop the model. Norris, T. B. and Lien, M.-B. analyzed the data and wrote the manuscript.

3.1 Introduction and Background

Nanoscale noble metal structures, such as gold and silver nanoparticles, exhibit optical and electronic properties that are not observed in their bulk counterparts. The electromagnetic modes of these systems, known as surface plasmon resonances (SPRs), lead to strong interaction with light, and an enhancement of the optical field enabling nonlinear effects to be observed with low incident light intensity (*54*, *95*). The plasmon resonances and the field enhancement can be tailored through the choice of metal, the specific size and shape, the dielectric environment, and their mutual spatial arrangement (*96–98*). In fact, the

sensitivity of the resonances to the local dielectric and charge environment enables the SPR to serve as an optical interrogation of the environment and thus as an optical sensor. The attachment of chemical ligands enables selective sensing of chemical or biomedical targets. As a result, metal nanoparticles serve as important building blocks in the fields of modern chemical engineering (*99*), biosensors (*100*) and advanced microscopy (*101–103*). A fundamental understanding of the nonlinear optical response of metal nanostructures is thus essential for the development of optical applications of plasmonics.

The two principal nonlinear optical responses that can be observed on direct far-field excitation are multi-photon luminescence (PL) and harmonic generation (HG). Both phenomena have been investigated extensively. Early observations of two-photon luminescence (TPL) were reported by Boyd et al (*104*), and interpreted as the generation and recombination of electron–hole pairs involving the d-band and the conduction (sp) band. The luminescence efficiency of gold nanoparticles can be remarkably high (*105*), suggesting applications to biological labeling and imaging (*106*). More recently, harmonic generation from metal nanoparticles has received considerable attention. Lippitz et al. reported the first observation of third-harmonic generation (THG) from individual gold colloidal particles down to 40 nm diameter (*28*), and third harmonic imaging experiments with gold nanorods was demonstrated in (*28*, *29*). The theory of second harmonic generation (SHG) from

spherical metallic centrosymmetric particles was treated phenomenologically by J. I. Dadap et al (*31*, *32*). Starting with the second order nonlinear surface susceptibilities, they presented a general electro-magnetic theory of SH Rayleigh scattering (SHRS) for spheres within the small particle limit, including the contribution from the bulk nonlinear response compatible with isotropic symmetry. They predicted a quadrupolar-type radiation pattern, as the second order process is in principle dipole-forbidden in centrosymmetric material with centrosymmetric geometry, consistent with experimental results on hyper-Rayleigh scattering from silver nanospheres by Hao et al (*60*) and a series of polarization analysis experiments performed by Brevet et al (*52*, *56*, *57*).

3.2 Motivation and Hypothesis

On optical excitation with ultrashort optical pulses, gold nanorods (AuNRs) exhibit hyper-Rayleigh scattering (SHG and THG) as well as a broadband feature attributed to PL. An example of the scattered light spectrum under 800-nm 50-fs excitation in our experiments (discussed in detail below) displays these features as shown in Figure 1(a). These responses have been respectively interpreted in terms of conventional nonlinear optical processes (*28*, *53*) and multi-photon interband luminescence processes (*50*, *61*, *105*, *107*). There are, however, features of the data whose interpretation is problematic with these physical models. The SHG signal, for example, is surprisingly strong, whereas in the small

particle limit SHG should be forbidden given the assumed centrosymmetry of the system; this has been attributed to the effects of either metal-media interface or retardation (*31*, *32*, *52*, *56*, *57*, *60*). Additionally, the SHG and THG signal from AuNRs can show saturation-like characteristics in the power scaling (see Fig 1b and 1c), which has been ambiguously attributed to damage of nanoparticles (*29*). The broadband spectral feature that has been attributed to PL in gold nanoantennas has recently been shown to depend primarily on the nanoscopic geometry, and does not in fact arise from the gold band structure (*59*). Finally, the nonlinear response has been theoretically predicted to exhibit unusual scaling with excitation intensity due to surface confinement effects on the electrons undergoing collective oscillation in the SPR (*108*).

Among the most common forms of structure used for studies of nanoplasmonics are chemically synthesized AuNRs, grown in aqueous solution guided by the surfactant cetyltrimethylammonium bromide (CTAB).(*109*) These structures exhibit a high degree of structural symmetry and crystallinity, as can be seen from the atomic-resolution high-angle annular dark-field images and convergent beam electron diffraction pattern of a single AuNR of the sample used in these experiments in **Fig. 3.1 A, B**. A spatial analysis of the electrostatic potential around the AuNRs was recently performed using off-axis electron holography.(*110*) In the absence of magnetic field, the phase shift $\phi(x, y)$ in an electron wave after passing

through a specimen is proportional to a line integral of the electrostatic potential along the propagation direction.(*111*) The reconstructed phase shift $\phi(x, y)$ map obtained for a AuNR shows a considerable asymmetry and a distinctive slope along the long axis of the rod as seen in **Fig. 3.1 C, D**, indicating the presence of a static dipole moment. In a recent companion study,(*24*) we have found that non-uniform coverage of the surfactant CTAB induces a static dipole moment, which breaks the inversion symmetry and leads to an optical asymmetry. This has far-reaching consequences, since for an optically symmetric nanoparticle, SHG is forbidden to lowest order, and can arise only through the effect of retardation and quadrupole radiation. Motivated by these considerations, we have performed a systematic series of nonlinear light scattering experiments, with the goal of obtaining a physical model that can simultaneously, self-consistently, and quantitatively explain all the major features of nonlinear light scattering observed in Chapter 2.

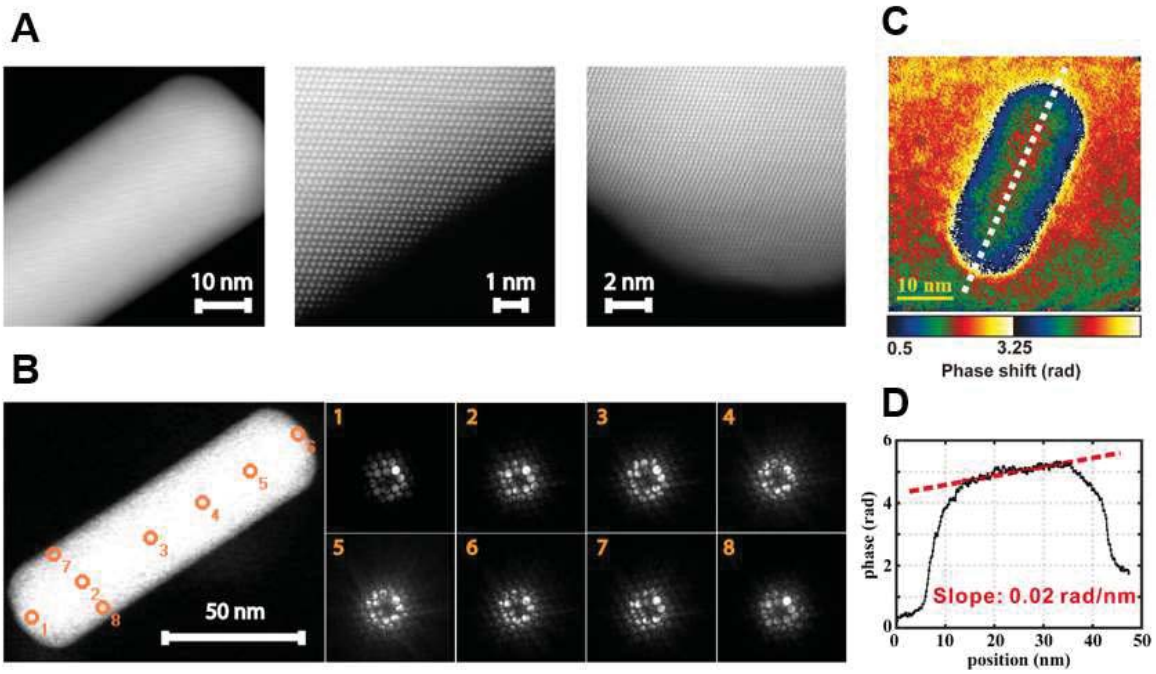

Figure 3.1 Structural symmetry and electrostatic asymmetry of AuNR. (**A**) Atomic-resolution high-angle annular dark-field (HAADF) images of a single AuNR used in the optical experiment and (**B**) convergent beam electron diffraction (CBED) pattern collected with beam positioned at various locations (orange markers) in the AuNR. Results indicated consistent structure in all areas of the rod and showed the high degree of structural symmetry of the AuNRs. (**C**) False-color reconstructed phase shift image and (**D**) its line profile along the long axis (white dashed line in d) of the AuNR.

3.3 Experimental Setup

The experimental setup is shown in Figure **Fig. 3.2**. The excitation source is a Ti:sapphire mode-locked laser, which provides 800-nm, 50-fs pulses at a repetition rate of 76 MHz. The excitation power is controlled by a variable attenuator consisting of a half-wave plate mounted on a programmable rotator and a Glan-Thompson polarizer. The laser pulses pass through a prism compressor so the pulses will be transform-limited at the beam focus. A

small fraction of the beam is sampled and monitored by a photodiode to measure the incident power and its fluctuations. In addition, a 780 nm high-pass filter is also placed before the focusing lens to ensure there is no residual SHG or THG in the excitation beam. The beam is focused in the center of a cuvette containing an aqueous solution of AuNRs resonance at 808 nm. Light scattered at 90° to the excitation direction is collected by an $f^{/\#}$=1 uv-coated lens and filtered through either BG filters (BG-39, BG-40 color filters) or 267 nm band-pass filters to remove the linear 800 nm scattering. The collected signal is focused on the entrance slit of a monochromator and detected by a single photon counting photomultiplier. A chopper is placed in the excitation beam path to modulate the excitation beam in order to subtract background dark counts from the signal in gated photon counting mode.

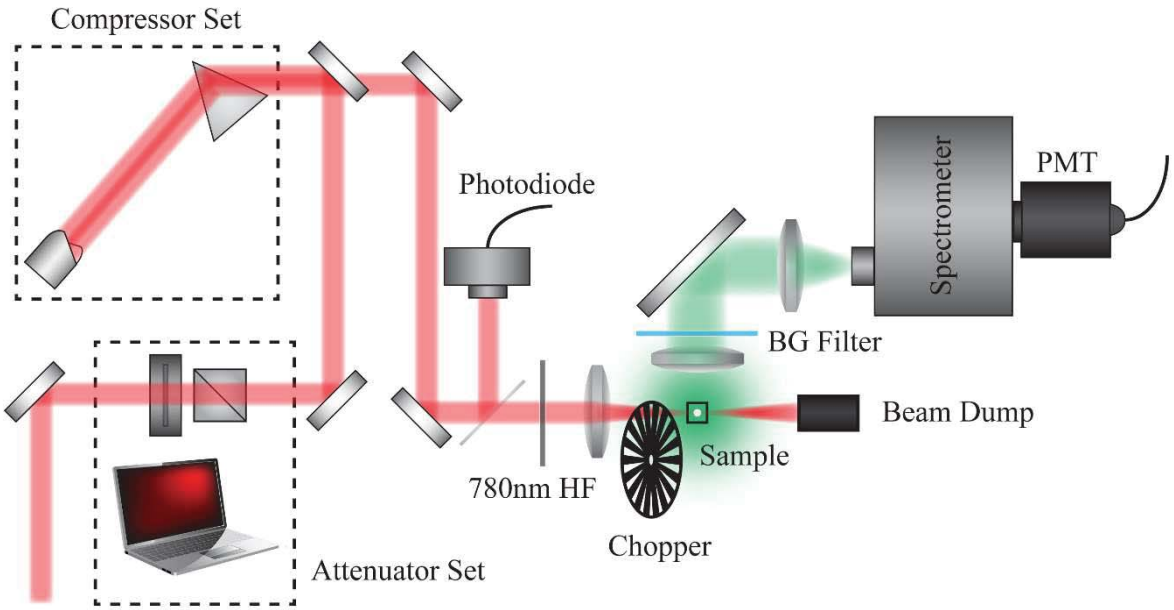

Figure 3.2 The experimental setup for the study on the nonlinear light scattering from AuNRs. The dynamic sampling of optical signal for the defined SNR is enabled by the programmable attenuator set; spectral and intensity dependence studies were performed.

3.4 Unexpected scaling of Harmonic Generation (HG) in the experimental results

A typical nonlinear scattered light spectrum is shown in **Fig. 3.3 A**, showing clearly three main components: THG and SHG peaks (hyper-Rayleigh scattering) and a broadband feature that is generally referred to as PL. We note that the SHG peak overlaps with the broadband photoluminescence. A key experiment to determining the physical processes underlying the light scattering is the scaling of the various spectral components with excitation intensity (or fluence, for fixed pulse duration). **Fig. 3.3 B and C** shows the measured scaling of the SHG and THG peaks. On the basis of the standard perturbation

theory of nonlinear optics (*112*), the SHG should scale exactly as the square of the intensity, and the THG as the cube.

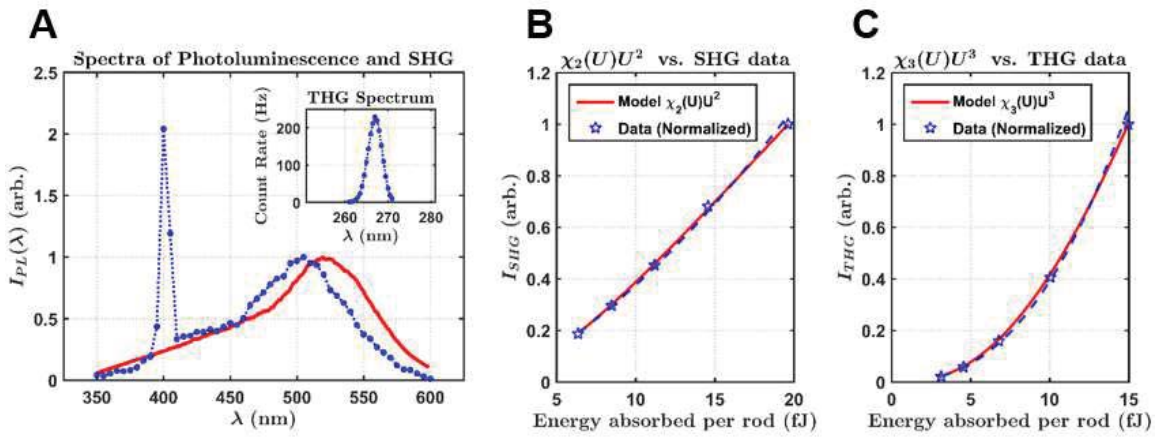

Figure 3.3 Nonlinear optical response on resonant excitation with 800-nm ultrashort pulses. (**A**) the spectral components include SHG, THG (inset) and a broadband PL. The red curve is the calculated spectrum with the proposed model (**B**) the unconventional intensity scaling of SHG (with the background PL subtracted) and (**C**) THG (background free). The blue dashed lines are the exponential fittings of the data and the red curves are the calculated SHG and THG with optically induced damping of the longitudinal SPR model. Notice the red curves fit the data better than the exponential fitting.

The THG signal has a well-defined spectral peak at 267 nm and is background-free (Figure 1 inset). A fit to a scaling curve of the form $I_{sig} = a(I_{ex})^b$ yields an exponent of 2.46 (±0.022), quite different from the expected value of 3. The SHG peak at 400 nm sits on top of the broad PL background. To determine the SHG scaling, we subtract the PL before integrating the area under the 400-nm peak (the assumption that the PL spectrum is smooth

is fully justified by the model below). The background-subtracted SHG scales with an exponent of 1.49, far from its conventional expected value of 2.

3.5 HG with optically induced plasmon damping

The unexpected scaling of the SHG and THG signals can be explained quantitatively by optically induced damping of the longitudinal SPR by hot electrons. (*113*, *114*). In a model of the SPR mode of the AuNR as a classical anharmonic oscillator, the second and third order nonlinear susceptibilities χ_2 and χ_3 are related to the linear susceptibility χ_1 by

$\chi^{(2)}(\omega) \propto \chi^{(1)}(2\omega)\left[\chi^{(1)}(\omega)\right]^2$ and $\chi^{(3)}(\omega) \propto \chi^{(1)}(3\omega)\left[\chi^{(1)}(\omega)\right]^3$ where

$\chi^{(1)}(\omega) = \frac{N(e^2/m)}{\epsilon_0 D(\omega)}, D(\omega) = \omega_0^2 - \omega^2 - 2i\omega\gamma$ and ω_0 is the material resonance frequency

The factor $D(\omega)$ contains the resonance frequency of the system (corresponding to 808 nm wavelength for the longitudinal plasmon mode of the gold nanorod) and the damping rate γ. It has been shown in (*114*) that scattering of the nanoparticle plasmon from single-particle excitations of the electron gas is the dominant nonlinearity in the optical response, as γ depends on the electron temperature. Following the Fermi liquid model of (*114*), we find the intensity scaling will be modified by the pump-induced electron heating according to

$I_{SHG} \propto \chi^{(2)}(\omega) I^2 \propto \left[I/\gamma_p\right]^2$ and $I_{THG} \propto \chi^{(3)}(\omega) I^3 \propto \left[I/\gamma_p\right]^3$ where

$\gamma_p \propto \langle \gamma_{ee} \rangle = \frac{\int_0^\infty f(\varepsilon)\gamma_{ee}(\varepsilon)d\varepsilon}{\int_0^\infty f(\varepsilon)d\varepsilon}$ is the total electron-temperature-dependent scattering rate and

$\gamma_{ee}(\varepsilon, T_e) = \gamma_0 + \frac{K(\pi k_B T_e)^2 + (\varepsilon - \varepsilon_F)^2}{1 + \exp[-(\varepsilon - \varepsilon_F)/k_B T_e]}$.

The model has only two fitting parameters, namely γ_0, the electronic-temperature-independent part of γ_{ee}, and U_{abs}, the absorbed pulse energy per gold nanorod that results in heating the conduction band electrons (*115*). The SHG and THG scaling fit the model very well (data fits are 1.49, 2.46 and the model predictions are 1.47, 2.41 for SHG and THG respectively) for a single value of $\gamma_0 = 0.067$ (fs^{-1}) and $U_{abs} \approx 0.267 U_{th}$, where U_{th} is the absorbed energy estimated from the estimated incident intensity and a classical model of the absorption cross section of a gold nanorod (*97*). In fact, it can be seen in in **Fig. 3.3 B and C** that the Fermi liquid model fits the scaling data better than an assumed power law scaling. We conclude that the SPR damping induced by a hot thermal distribution of single-particle excitations quantitatively accounts for the unexpected scaling of the nonlinear optical response of the AuNR longitudinal plasmon resonance.

3.6 Origin of the broadband photoluminescence

We now discuss the broadband scattered light; the literature has generally attributed this signal to PL arising from the recombination of d-band holes with conduction band electrons excited by multiphoton absorption. Our key new experiment is the complete spectral dependence of the intensity scaling of the broadband emission, as shown in **Fig. 3.4**. The scattered light scales with an exponent of approximately 3.6 at 375 nm to 2.5 above 550 nm; i.e. the shorter wavelength emission exhibits a more highly nonlinear behavior. Interestingly, the total signal at 400 nm (i.e. the sum of the coherent SHG and the broadband signal) does not follow the general trend, but scales with an exponent of 1.92. While multiphoton PL from an interband process can account for some features of the spectrum (*54*, *55*, *101*, *105*), others are inconsistent with PL as the source of the broadband emission. In particular, the spectral features of the broadband spectrum from AuNRs do not really match well with those from their bulk counterpart, though some previous work has attempted to attribute these features to recombination processes between conduction band electrons and d-band holes near the X and L symmetry points in the gold band structure (*50*, *61*, *101*, *107*). Recent experiments comparing PL from gold nanoantennas fabricated from single crystals and polycrystalline films, however, have suggested that it is the nanoscale geometry of the plasmonic structures that determines the shape of the emission spectra (*59*),

and not the band structure. Most importantly in this study, we performed an additional set of experiments in which the AuNRs were excited directly with 400-nm fs pulses (generated by frequency doubling the Ti:sapphire laser), which should induce one-photon absorption energetically equivalent to 2-photon absorption at 800 nm. The threshold for absorption from the d bands in Au is 1.8 eV; hence 800-nm excitation from the d-band requires two- or three-photon absorption, while linear absorption of 400-nm light can excite d-band holes. We found there was only negligible emission from the AuNRs under 400-nm excitation even at the highest accessible excitation intensity; this indicates unequivocally that the broadband emission under 800-nm excitation does not arise from interband transitions as is usually thought. Our results are consistent with those of (*59*)

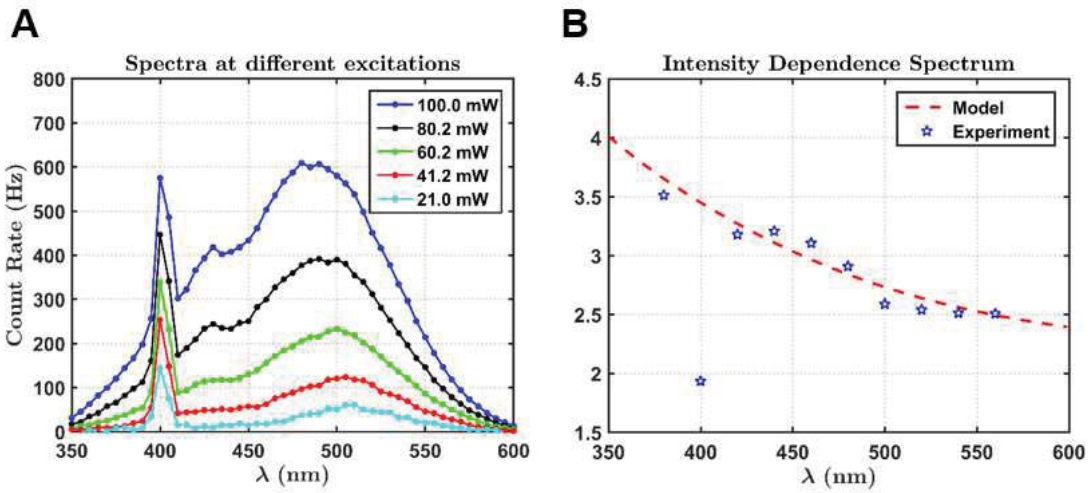

Figure 3.4 Measurement of the spectral dependence of the intensity scaling of the PL. (**A**) The spectra of nonlinear optical responses measured at different excitation intensities (**B**) The spectrally resolved intensity dependent scaling. Notice the scaling at 400 nm is close to 2. The red dash curve is generated from the proposed model.

3.7 New model for the broadband photoluminescence

Given that the broadband emission is not in fact interband PL, we propose a new model in which the nonlinear light scattering arises from an interplay of the plasmon damping and the optical anisotropy due to the static dipole on the AuNRs. On illumination with 800-nm pulses, the gold nanorod's longitudinal plasmon mode is resonantly excited, corresponding to a collective oscillation of the electrons along the long axis of the particle. The charge asymmetry associated with the static dipole along the nanorod axis gives rise to a nonzero $\chi^{(2)}$; the second-order nonlinear polarization along the nanorod axis excites the asymmetric second-order longitudinal plasmon mode, which can efficiently scatter with the background free electron gas just as the fundamental plasmon mode scatters, as described above.

The process is illustrated in Figure 5(a), indicating how two longitudinal plasmons excited by the pump give rise to a fluctuating polarization P_ω due to scattering from the free electron gas. Physically, electrons oscillating in opposite directions in the asymmetric second-order longitudinal mode scatter with free carriers, producing dipole fluctuations along the transverse gold nanorod axis, see **Fig. 3.5 B** inset. The emission arises as radiation from P_ω, and the coupling of these dipole fluctuations to free-space electromagnetic modes is

enhanced by the transverse plasmon mode of the AuNRs. A continuum of radiation is produced since the scattering of an electron with initial energy $\varepsilon - \Delta/2$ to a final state with energy $\varepsilon + \Delta/2$ results in a shift Δ of the emission relative to the second harmonic of the 800-nm excitation; the broadband spectrum arises from an integral over all possible initial and final free-carrier states with occupations f_i and f_f determined by the Fermi function for a carrier gas with electron temperature T_e, which is well-known from the scaling experiments on SHG and THG discussed above. Since the nonlinear light scattering is driven by scattering of plasmons from free carriers, the total emission should be proportional to the plasmonic damping rate, $\gamma_p \propto \langle \gamma_{ee} \rangle$. Finally, the scattered spectrum $I(\omega)$ will be proportional to a lineshape factor $L(\omega)$ given by the Fourier transform of the dipole-dipole correlation function, and by the fluctuation-dissipation theorem this is proportional to the imaginary part of the susceptibility, i.e. the absorption spectrum (*116*, *117*); in the calculation we use the actual experimental absorption spectrum of the gold nanorod sample. Putting all these elements together, the broadband scattered light will be given by the expression

$$I(\lambda, U) = I(\omega, T_e) \propto \int f(\varepsilon - \Delta/2)[1 - f(\varepsilon + \Delta/2)]\, d\varepsilon \cdot \gamma_{ee}(T_e) \cdot L(\omega) \quad \text{(Eq. 3.1)}$$

where $\Delta = 2\hbar\omega_{800\,\mathrm{nm}} - \hbar\omega$ and $f(\varepsilon) = \frac{1}{1+\exp\frac{(\varepsilon-\varepsilon_F)}{k_B T_e}}$

is the Fermi function with electron temperature $T_e(U)$.

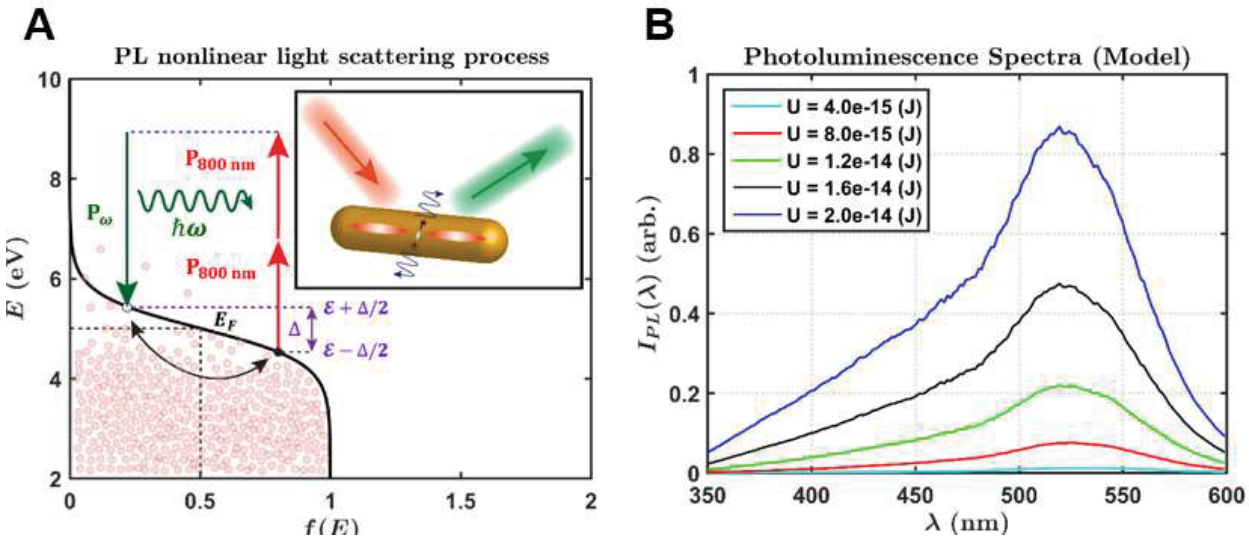

Figure 3.5 Picture of the PL nonlinear light scattering process and the reproduced PL spectra. (**A**) Energy diagram of the PL nonlinear light scattering process and (inset) a physical illustration of the 2nd order plasmon excitation and the PL generation. (**B**) Calculated scattered light spectrum using the values of γ_ee and U_abs obtained from the SHG and THG experiments. The spectral line shape is determined by the (structure dependent) absorption spectrum of AuNRs, i.e., the measured UV-VIS spectrum.

Fig. 3.5 B shows the calculated scattered light spectrum using the values of γ_{ee} and U_{abs} obtained from the SHG and THG experiments; **Fig. 3.3 B and C** shows the close match of the theory (red line) and experimental (blue dots) line shapes. Note that the spectral smoothness around the SHG position justifies the interpolation and subtraction of the background from the SHG peak around 400 nm discussed above. Most critically, we can also generate from the calculation the intensity scaling as a function of wavelength; the result shown as the red curve in **Fig. 3.4 B**, and shows excellent agreement with the data. This is a strong

confirmation of the model, indicating that intraband PL processes do not play a significant role in the multiphoton broadband emission, but that second-order nonlinear light scattering mediated by damping of the second-order longitudinal plasmon resonance is mainly responsible for the scattered light. It should be noted the only fitting parameter in the calculation is the value of the Fermi level; the fitting leads to $\varepsilon_F = 5.4$ (eV), which is very close to the bulk value of 5.5 (eV), and the slight difference may be due to pump-induced heating. A final confirmation that the second-order light scattering mechanism described above is correct is the observation that excitation at 400 nm only leads to negligible broadband emission; excitation at 400 nm does not induce an excitation of the second order plasmon mode which could then scatter into a fluctuating dipole transverse to the nanorod.

3.8 Conclusion and Outlook

In summary, we have performed a systematic series of experiments on nonlinear light scattering from AuNRs under resonant excitation of the longitudinal plasmon mode, with detailed measurements of the spectral dependence of the intensity scaling across the SHG, THG, and broadband components. From measurements using electron holography in Chapter 2, we know that the structurally symmetric gold nanorods are in fact electrically and optically anisotropic due to charges on the ligands used to guide their self-assembly. This optical asymmetry leads to strong second-order polarizability $\chi^{(2)}$ and hence the significant

SHG signal. The SHG and THG nonlinear susceptibilities are intensity dependent, through the optically induced damping of the SPR linear susceptibility, corresponding to scattering of the plasmon with hot electrons; this damping is quantitatively understood through the electron temperature dependence in the Fermi liquid model. Because of the nonzero $\chi^{(2)}$, the second-order longitudinal mode is excited. Scattering of this mode from the electron gas results in a fluctuating polarization along the transverse direction of the nanorod, which radiates a broadband spectrum. The spectrum as well as the intensity scaling are understood through a self-consistent model of light scattering. Interband processes apparently play no significant role in the light emission. We note finally that the model incorporates the actual SPR spectrum through the fluctuation-dissipation theorem and assumes scattering from a perfectly thermalized electron gas, and hence does not account for the individual microscopic scattering processes responsible for the radiation. It thus cannot account for the possible role of coherence in the scattering process, which may be important for the complete interpretation of the emission around 400 nm; the nearly quadratic scaling of the total signal at 400 nm (SHG + broadband component) is highly suggestive, and remains the subject for additional study.

3.9 Methods

3.9.1 GNR sample and the damage testing

The data presented in this paper are from samples consisting of aqueous solutions of AuNRs purchased from Nanopartz. The solution concentration is approximately 1 nM, sufficiently low that particle interaction effects are neglible. The AuNRs have diameter 25 nm and length 102 nm, leading to a transverse plasmon resonance at 517 nm and longitudinal plasmon resonance at 808 nm. The solution sample is placed in a UV transparent cuvette during the optical excitation to avoid the absorption of the scattered nonlinear optical signal.

We rule out the possibility of rod melting by monitoring the difference between the initial and final UV-VIS spectra of the gold nanorod solution sample. Gold nanorods in solution can be melted into spherical nanoparticles by excitation with intense femtosecond laser pulses of sufficient energy. If the energy absorbed by the rods are strong enough such that the rods are partially melted before diffusing out of the focal volume, the longitudinal absorption band would blue-shift, as the aspect ratio of the rods would decrease. If the absorbed energy is even larger such that the rods completely melt into spheres before diffusing out of the focal volume, the intensity of the longitudinal absorption band would

decrease, while the intensity of the transverse absorption band would increase, suggesting the depletion of the gold nanorods and the formation of spherical nanoparticles. This phenomenon has previously been observed and reported as a valid method to monitor the rod shape change (*118*). Indeed, even with the most intense excitation in our experiment, no blue-shift or the decrement of the longitudinal absorption intensity in the final UV-VIS spectrum was observed, indicating that no rod melting occurred.

3.9.2 Intensity dependence measurement

The measurement of the intensity scaling corresponds to the determination of γ from $y = ax^{\gamma}$ where y represents the optical signal and x represents the excitation intensity. The task is essentially the extraction of the fitted linear slope from the data points in a log-log plot, which must be performed in such a way as to obtain a well-defined error in the determined scaling coefficient. Consider several data points measured with increasing incident intensities. The integration time at each incident intensity is varied to control the error bar on each of the data points, such that the error bars on the log-log plot have equal width. This can be achieved by making the signal-noise-ratio (SNR) the same at every data point via the number of measurements at each data point. Let μ be the population mean, $\bar{x}$ be the sample mean, σ^2 be population variance and s^2 be sample variance. With n samples, we have

$\mu = \bar{x} \pm t_{n-1}\frac{s}{\sqrt{n}} = \bar{x} \pm \Delta x$ for 95% confidence under t-distribution, and we define $SNR = K = \bar{x}/\Delta x$. Now $\bar{x}$ and s can be obtained through measurements and the estimated number of samplings n to reach the desired $SNR = K$ is $n = \left[\frac{K \cdot t_{n-1} s}{\bar{x}}\right]^2$. With these definitions, we developed the following procedure to reach a desired $SNR = K$:

1. Take $n_0 = 10$ measurements and calculate $\bar{x}_{10}$ and s_{10}. In our case we collect photon counts in 5 sec segments for 10 times.
2. Compare $K_{10} = \bar{x}_{10}/t_{10-1}\frac{s_{10}}{\sqrt{10}}$ to the desired SNR, K, where $t_9 = 2.262$. If $K_{10} > K$, we conclude that the desired SNR is reached and take $\bar{x}_{10}$ as the signal count rate.
3. If $K_{10} < K$, we enlarge n_1 by $n_1 = \left[\frac{K \cdot t_{10-1} s_{10}}{\bar{x}_{10}}\right]^2$
4. Take additional $n_1 - n_0$ points. Calculate $\bar{x}_{n_1}$, s_{n_1} and K_{n_1}. Note $\bar{x}_n$ and s_n will converge as $n \to \infty$.
5. Repeat 2 – 4.

The procedure ensures that on each data point, the error bars on the log-log plot are with equal width $\log\frac{K+1}{K-1}$, hence minimizing the variance of the extracted fitted linear slope on the log-log plot.

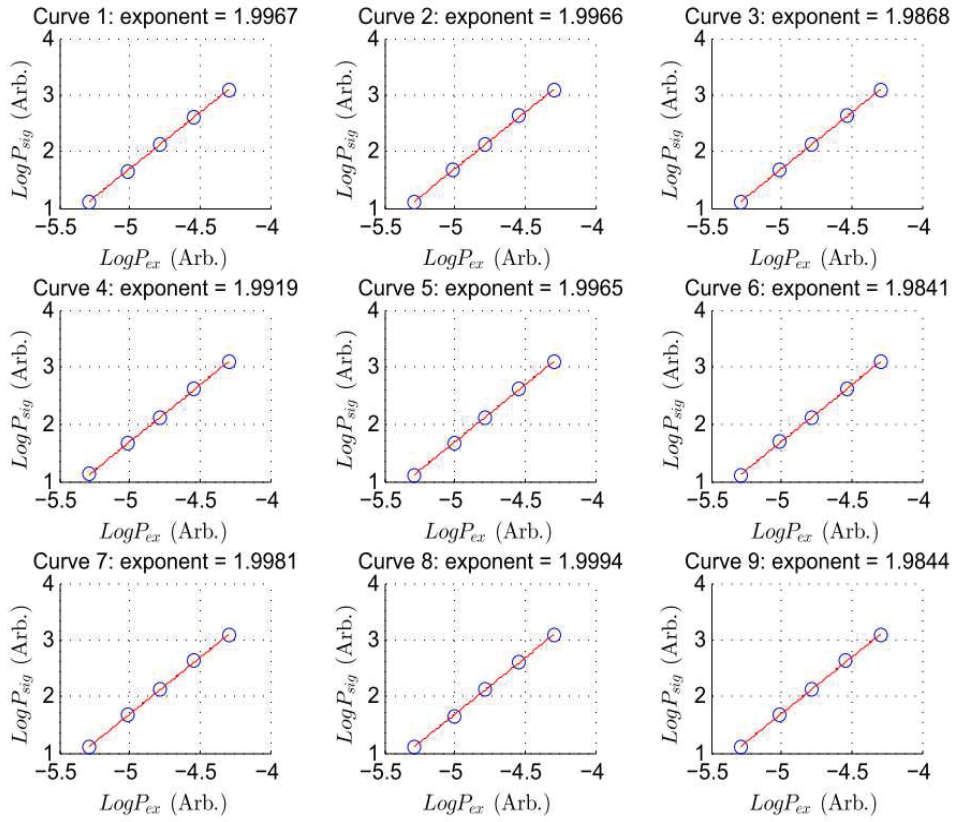

Figure 3.6 Intensity dependence measurements of Rhodamine 6G. The measurements serve as the validation of our statistical analysis and the proposed sampling strategy.

Chapter 4 Ligand-directed Nanoparticle Assembly for Homochiral Structures

Portions of this chapter are reproduced, with modifications, from Feng, W.; Kim, J.-Y.; Wang, X.; Calcaterra, H.A.; Qu, Z.; Meshi, L.; Kotov, N.A. "Homochiral Semiconductor Helices at the Mesoscale." Science Advances 3, e1601159 (2017), with permission from AAAS.

4.1 Introduction and Background

Previous methods of preparation of nano-/microscale particles and assemblies from various materials (ZnO (*119*), ZnS (*120*), InP (*121*), InGaAs/GaAs (*122*), CdS (*123*)) mostly yielded racemic mixtures that did not display chiroptical activity, with the exception of chiral MoS_2 nanofibers formed under vortex stirring (*124*). Chirality (*125*) and optical circular dichroism (*126*) of carbon nanotubes has long been recognized and theorized, with chiroptical properties of enantiopure carbonaceous nanotubes being experimentally determined (*127*). Chiral silica fibers were reported to be chiroptically active in the UV region by diffuse reflectance circular dichroism (*128*). Chiral silica thin films are potentially useful as templates for producing diverse chiral inorganic films, as well as in catalysis, enantioselective separation and tunable reflective filters and sensors (*129*).

In this study, cysteine (Cys) was used as the stabilizer or crosslinker for the various inorganic NPs and composite materials. Self-assembly of L-Cys- or D-Cys-stabilized NPs yielded homochiral mesoscale assemblies whose handedness was solely dependent on the Cys

enantiomer: D-Cys NPs assembled into right-handed structures, whereas L-Cys NPs afforded left-handed structures. These homochiral asemblies at the mesoscale present a rare opportunity to unambiguously establish the relationship between their geometry and chiroptical activity for various materials.

4.2 Self-Assembled Homochiral Cadmium Telluride (CdTe) Helices

Contributions: Kim, J.-Y. and Feng, W. carried out CdTe NP synthesis, assembly, and characterization. Kim, J.-Y. and F Feng, W. developed the models for computations. Feng, W., Wang, X., and Calcaterra H.A. performed Lumerical simulations. Feng, W. and Qu, Z. studied 3D tomography of helices. Meshi, L. carried out TEM studies on CdTe NPs. Kotov, N.A. supervised the project. Feng, W. and Kotov, N.A. analyzed the data and co-wrote the paper. All authors discussed the results and commented on the manuscript.

4.2.1 Introduction

Assemblies of plasmonic NPs with characteristic lengths of 10−1000 nm acquire chiral geometries when assembled using antibody-antigen recognition (*130*), DNA bridge (*131*), or embedded in nematic liquid crystal phase (*132*). Strong polarization rotation in nanoscale assemblies has enabled highly sensitive biological analysis of environmental toxins, cancer biomarkers, and DNA (*130*, *131*).

While significant progress has been made towards understanding the relationship between the optical activity and geometrical parameters of plasmonic nanostructures, knowledge about such relationships in semiconductor nanomaterials remains cursory (*133–137*). Versatility in tuning chemical, physical, and biological properties, as well as methods (*37*, *124*, *137*), to

produce chiral semiconductor nanomaterials in large enantiomeric excess (e.e.), make them attractive candidates for polarization-based optical devices and catalysts. In this work, we intend to advance current understanding of the geometry-property relationship of chiral semiconductor nanomaterials, knowledge that will guide the materials design of inorganic nanostructures with application-adapted chiroptical properties. Chiroptically active semiconductor nanomaterials can be made using self-assembly processes that are sensitive to small anisotropies in inter-particle forces (*138*). The CdTe helices prepared here displayed broad-band Vis-NIR rotatory activity, a critical prerequisite for a wide array of applications including biomedical diagnostics (*139*), telecommunications (*140*), and hyperspectral imaging and sensing (*141*, *142*). The anisotropy (g) factor approaches 0.01, an improvement of two orders of magnitude compared to the individual NP building blocks. Computational simulations also assist in deciphering the complex relationship between geometry and optical activity by analyzing the effect of individual structural modifications on chiroptical response.

4.2.2 Self-Assembly of Helices

The strength of interactions between CdTe NPs depends on their solvation environment. Due to reduced ionization of carboxyl and amino group, the attractive forces between polar NPs become stronger than the repulsive electrostatic ones when media around NPs was changed from water to methanol. Therefore, Cys-stabilized CdTe NPs in methanol undergo a self-assembly process forming well-defined helices. Unlike other known processes of enantioselective synthesis which yield products of modest optical purity (*137*, *143–145*), this collective multi-

particle assembly process is nearly monolithic in respect to chiral preference of the products. As-formed semiconductor helices are homochiral (**Fig. 4.1A, B**), with a singular handedness corresponding to the specific handedness of the Cys molecule used during the NP synthesis: L-Cys corresponds to an exclusively left-handed geometry, whereas D-Cys leads to right-handed helices. STEM 3D tomography revealed that the helices had negative Gaussian curvatures (**Fig. 4.1 C,D**). These helices are at the mesoscale, as the thickness falls below 100 nm but the average diameter reaches 300 nm and the length is on the micron scale (up to 6 μm). The chirality of the ligand was found to be important in helix formation: When an achiral stabilizer such as thioglycolic acid was used as the stabilizer for CdTe NP synthesis, assemblies formed under identical experimental conditions appeared to have no observable helicity (**Fig. 4.2**).

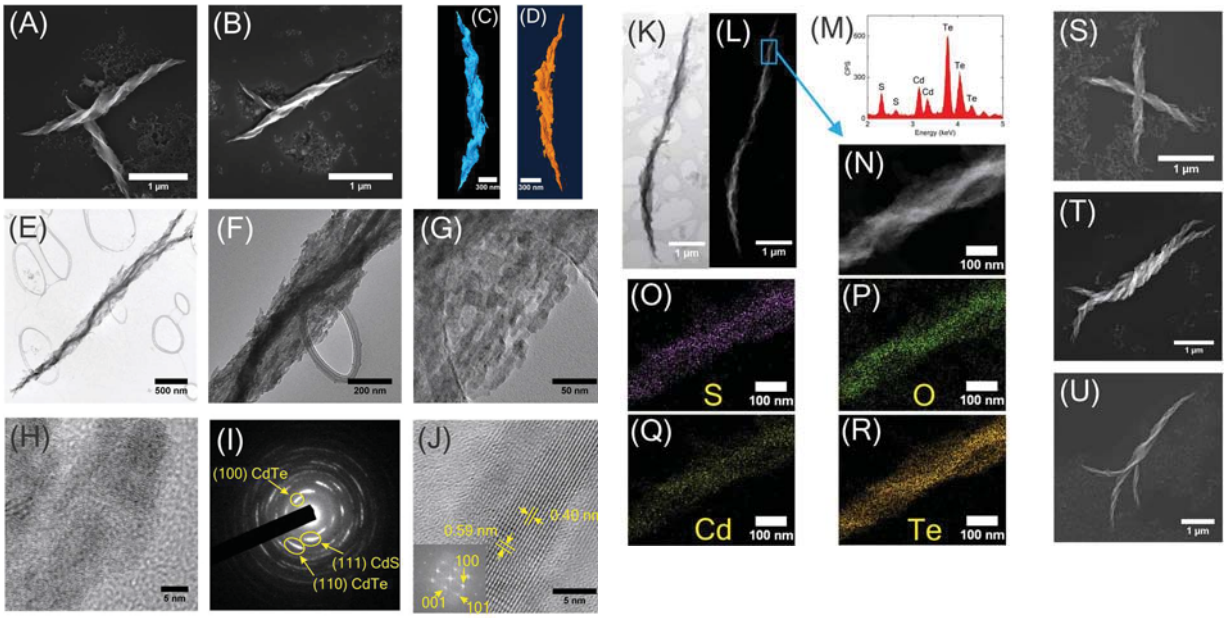

Figure 4.1 Structural and Elemental Analysis. SEM images of (A) R-helix assembled from D-Cys CdTe NPs, and (B) L-helix assembled from L-Cys CdTe NPs. STEM tomography of (C) R-helix and (D) L-helix. TEM images of an R-helix at (E) low magnification, (F) medium magnification, and (G) high magnification; (H) HRTEM of helix boundary; (I) SAED graph; (J) HRTEM of nanowire core (inset, FFT graph). (K) BF-STEM and (L) HAADF-STEM imaging of a R-helix; (M) STEM-EDX spectrum; (N) HAADF-STEM image of a highlighted region from image (L); (O)-(R) Elemental mapping of sulfur (S), oxygen (O), cadmium (Cd) and tellurium (Te), respectively. SEM images of hierarchical assemblies of (S) intercrossed helices, (T) intertwined helices, and (U) dendritic twists.

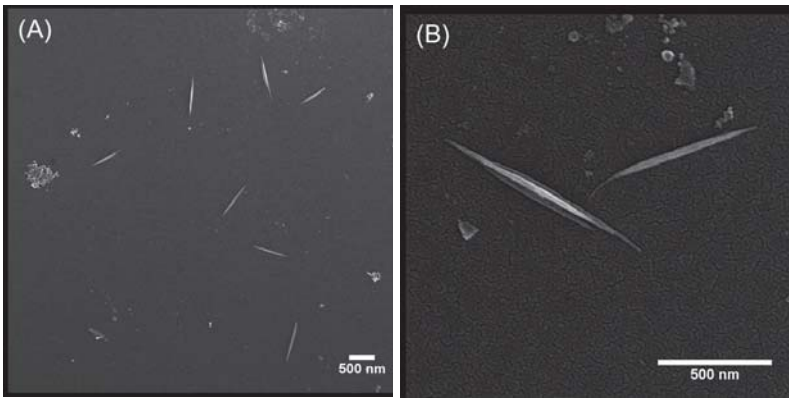

Figure 4.2 Assembly from TGA-CdTe NPs. SEM images of assemblies from achiral TGA-CdTe NPs, at different magnifications.

Large quantities of helices (> 100) were surveyed by scanning electron microscopy (SEM) at random regions of a dropcast sample to determine e.e. for L- and D-Cys CdTe assemblies, respectively. The e.e. approaches 100% for both: L-Cys CdTe NPs assembled into 100 L-helices and one R-helix (e.e. = 98%); D-Cys CdTe NPs produced 101 R-helices and no L-helix (e.e. = 100%). The rare helix with "abnormal" handedness (e.g. the R-helix formed within L-Cys CdTe assemblies), has a distinct morphology of rotating platelets along a common axis (**Fig. 4.3**). Similar chiral branched structures have been reported for other semiconductor materials where the helicity is attributed to the elastic strain of the axial screw dislocation (*146*).

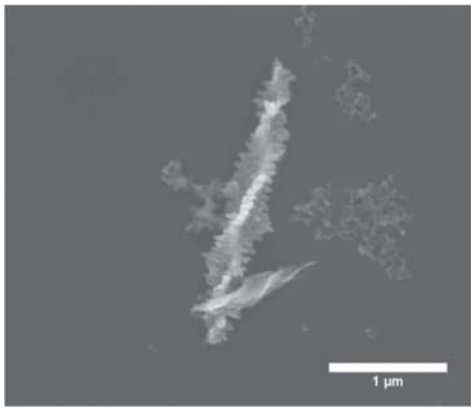

Figure 4.3 Helical structure of opposite handedness found among helices assembled from L-Cys CdTe NPs. A regular helix to its bottom right serves as a comparison in morphologies.

The helix appears to contain a nanowire core under transmission electron microscopy (TEM, **Fig. 4.1 E**). The nanowire diameter is ~60 nm with a twisted morphology (**Fig. 4.1 F**). Attached to the nanowire core are polycrystalline grains (**Fig. 4.1 G**), oriented in a preferred direction along the helix axis (**Fig. 4.1 H**). Selected area electron diffraction (SAED) analysis (**Fig. 4.1 I**) shows partial ring patterns, a signature of oriented polycrystalline materials, and can be indexed

to CdS (JCPDS card No.75-0581) and CdTe (JCPDS card No.19-0193). The exposed part of the nanowire core shows lattice spacing of 0.40 and 0.59 nm (**Fig. 4.1 J**) which correspond to the (100) and (001) phases of hexagonal tellurium (Te, JCPDF card No.36-1452). Fast Fourier transform (FFT) diffraction (inset, **Fig. 4.1 J**) indicates a single crystalline material with (001), (100), and (101) phases of hexagonal Te. The complexity of the final assembly structure, with its outward helical shape and twisting nanowire core, is highly unusual. Previous work involving self-assembly of chiral CdTe NPs in water yielded cylindrical assemblies with a mostly straight Te nanowire core (*143*). Questions arose as to how the assembly process produced helical structures and how the nanowire core twisted. Similar morphological selection has recently been observed for amyloid fibers (*147*), where the competition between inter-filament and intra-filament forces tilted the balance for either cylindrical or helical structures. Analogously, we think that the helices acquired their shape due to geometric frustration between inter-grain strain and intra-grain bending ("grain" refers to oriented CdTe polycrystalline grains attached to the nanowire core). When the costs of inter-grain strain overwhelm intra-grain bending, an equilibrium morphological transition occurs from cylinders to helices. For the previously reported cylindrical CdTe assemblies, there is possibly only low inter-grain strain so the cylindrical assembly persists and the nanowire core experiences little bending. The helical assemblies, on the other hand, appear to have a higher extrinsic structural chirality than cylindrical ones. This is also reflected in the greater anisotropy (g) factor obtained for the helices ($g = \sim 0.01$) compared to the cylinders ($g = \sim 2\times10^{-4}$). This higher structural chirality may impart higher inter-grain strain to the point that the inter-grain strain is dominant over intra-grain

bending, leading to a morphological transition from cylinders to helices. The highly helical arrangement of CdTe attaching to the nanowire core, introduced mechanical stress that the nanowire core can only accommodate by structural bending. The end result of the push-and-pull within the CdTe grains themselves and between the grains, is a helical structure with a twisting nanowire core.

Scanning transmission electron microscopy (STEM) imaging also shows a twisting nanowire core that is higher in contrast than the rest of the helix (**Fig. 4.1 K-L**). The STEM energy dispersive X-ray (EDX) spectrum shows an excess of Te compared to Cd (**Fig. 4.1 M**), due to the existence of the Te nanowire core. Elemental mapping indicates that O, S, Cd, and Te are present in the helix (**Fig. 4.1 N-R**). In particular, the higher contrast region in the Te elemental map coincides with where the nanowire core was observed in imaging, confirming that the nanowire core consists of Te. Such a transformation from CdTe NPs to Te nanowires has been previously reported, where the Te^{2-} ions were oxidized by oxygen in solution and eventually converted to Te nanocrystals (*148*, *149*). Combining structural and elemental studies, we have shown that the helix is comprised of a Te nanowire core, to which CdTe grains are attached.

Hierarchical assemblies of helices emerge from primary helical structures (**Fig. 4.1 S-U**). These hierarchical assemblies retain the handedness as their primary helical structures. This phenomenon of multiple intertwining helical structures can be useful for engineering materials with additional structural complexity and functionality.

4.2.3 Formation Mechanism

A fundamental understanding of the assembly mechanism is required to explain the helical morphology and the extraordinary enantioselectivity. A recent report showed that Cys-CdTe NPs in a different solvent (water) assembled into cylindrical supraparticles, each one consisting of a Te core with CdTe attachment around it (*143*). Modeling in that work showed that when two Cys-CdTe NPs approach by dipole-dipole attraction, the collective chiral interaction between two NP faces exerts a geometrical twist, the direction of which is dependent on the exact enantiomer of the stabilizer. Similarly, for our system, this initial enantiomer-sensitive twist is expected to be the origin of the observed enantioselectivity. Through collective multi-particle interactions, Cys-CdTe NPs can then assemble into helical CdTe attachments around the Te nanowire core.

We follow the self-assembly process with TEM studies to gain insight into the formation mechanism. At the beginning of the assembly process, random aggregates with no specific geometrical shape were observed (**Fig. 4.4 A**). At 1 hour, a short thin Te nanowire (265 nm long and 14 nm wide) with some CdTe attachment emerges (**Fig. 4.4 B**). The Te nanowire exhibits the characteristic lattice fringes of 0.40 and 0.59 nm (**Fig. 4.4 C**) corresponding to the [100] direction of hexagonal Te (JCPDF card No.36-1452). At 3 hours, the Te nanowire grew longer and wider (656 nm long and 23 nm wide) with a slight bend (**Fig. 4.4 2D**). At 5 hours, the Te nanowire was observed to grow even larger (1846 nm long and 30 nm wide). The bending in the nanowire is more severe than that at 3 hours (**Fig. 4.4 E**). Tapering of the helix (the diameter of

the helix decreases towards its end) is obvious at this stage, where the 1D growth of the Te nanowire is accompanied by simultaneous attachment of CdTe, kinetically limiting the amount of CdTe attachment at the two ends of the nanowire. At 6 hours, fully formed helices emerged with a highly twisted Te nanowire core (3550 nm long and 61 nm wide) (**Fig. 4.4 F**). From this point on, the helices appear to be relatively stable in form as verified by comparing 6-hour assembled helices to 8-hour assembled ones (the Te nanowire length was slightly longer at 4071 nm and the width remained at 62 nm) (**Fig. 4.4 G**). This TEM study demonstrated that fast growth of the pre-helix assembly structure occurs during the first 6 hours of assembly, followed by a relatively slow growth of the helices as they are fully formed. The helix is formed through chiral arrangement of CdTe along a Te nanowire, during which the Te nanowire underwent mechanical deformation.

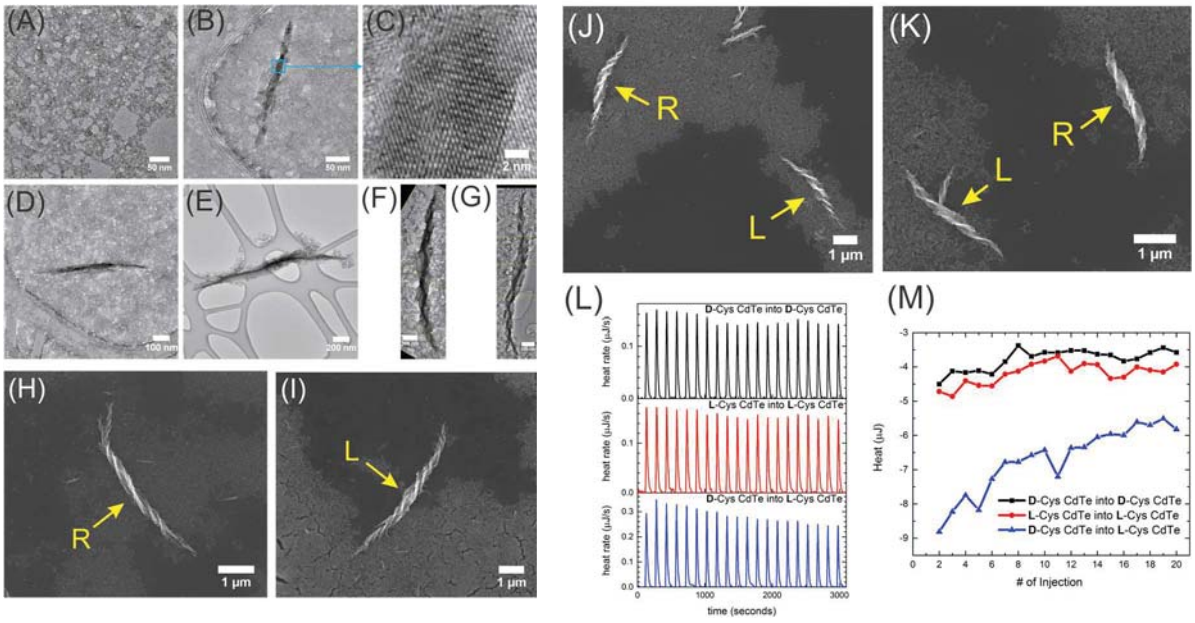

Figure 4.4 Formation Mechanism. TEM images: self-assembly of D-Cys CdTe NPs at (A) 0 hr, (B)1 hr, (C) 1 hr at higher magnification of the Te wire, (D) 3 hr, (E) 5 hr, (F) 6 hr, and (G) 8 hr. The yellow dashed lines in (F) and (G) represent the edges of images that were assembled together to display the entire helix. SEM images: (H) D-Cys CdTe NP assembly, (I) L-Cys CdTe NP assembly, (J) D,L-Cys CdTe NP assembly, and (K) D-Cys CdTe/L-Cys CdTe NP assembly. The arrows point to the helices with designated handedness (L: left-handed helix; R: right-handed helix). ITC experiments: (L) Heat rate and (M) total heat (integration of peak area) per injection. In (M), the first (small volume) injection is discarded.

To further elucidate the assembly mechanism, we prepared two types of racemic CdTe NPs for self-assembly under identical conditions. For the first racemic type, we used D,L-cysteine as the ligand for NP synthesis ("racemic by synthesis"). The second racemic type was made by mixing 1:1 volume ratio of D-Cys CdTe NPs with L-Cys CdTe NPs ("racemic by mixing"). We anticipated several possible assembly morphologies: Non-helical structures, helical structures where partial left-handedness and right-handedness co-exist within one helix, or helices of pure left-handedness or right-handedness. Assemblies prepared from original chiral NPs consist of highly enantiopure left-handed or right-handed helices (**Fig. 4.4 H-I**). Interestingly, for both

racemic cases, the assembled structures contain both left-handed and right-handed helices with an e.e. that correlates well with the starting NP e.e. (**Fig. 4.4 J-K, Table 4.1**). The D- and L-alone samples are chiroptically active, whereas both chiral racemics are not due to mutual cancelation (**Fig. 4.5**). This points to the power of chiral self-sorting among these NPs. Here chiral self-sorting refers to the phenomena of enantiomeric NPs preferentially recognizing themselves but not their mirror images (*150*), resulting in the formation of large-scale helices of uniform chirality. No intrahelical racemization was observed in any of these chiral or chiral racemic compositions, indicating a strong selection toward homochiral helices even in the presence of competing enantiomer. Similar chiral self-sorting has also been observed for fibrous protein hydrogels co-assembled from *N*-terminally protected amino acid Fmoc-(D/L)Glu and (D/L)Lys (*151*), as well as for chiral columns constructed via supramolecular helical organization of enantiomeric and racemic dendronized cyclotriveratrylene crowns (*152*). Although chiral interactions are generally considered to be weak, the collective behavior of NPs amplifies the effect of seemingly small energetic perturbations in potential of mean force (*138*). It is this collective action that secures the preservation and enhancement of the original chirality through supramolecular assemblies.

	L-helices	R-helices	Helices e.e.	NPs e.e.
Racemic by Synthesis	56	53	0.028	0
Racemic by Mixture	84	74	0.063	0.068

Table 4.1 Statistical analysis of racemic NP assemblies.

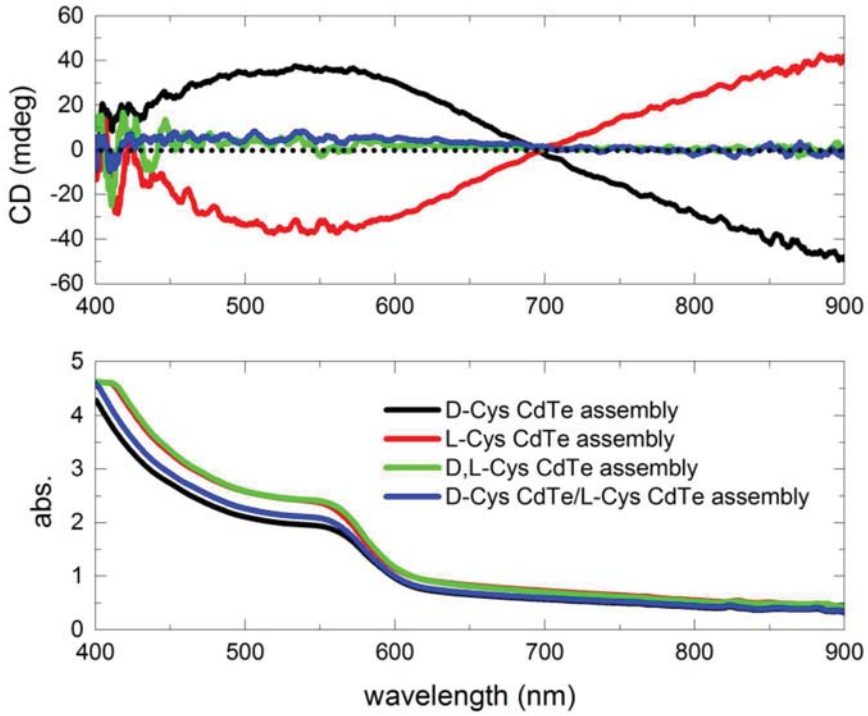

Figure 4.5 Chiroptical spectra of different NP assemblies.

The self-sorting phenomena clearly demonstrated the preferential interaction between CdTe NPs of the same handedness. To understand the chiral interactions at the NP level, isothermal titration calorimetry (ITC) was used to elucidate the energetics of chiral interactions between D/D, L/L, or D/L NPs (**Fig. 4.4 L-M, Fig. 4.6, Table 4.2**). The reaction between the same handedness NPs was found to be more spontaneous (more negative ΔG) than that for opposite handedness ones. ITC studies showed that NPs of the same chirality interact more strongly than those with opposing chirality, which correlates well with the self-sorting findings and contributes to our understanding of chiral interactions at the particle level.

	Length (nm)	Diameter (nm)	Pitch (nm)	# of Pitches	Thickness (nm)	Corresponding Figures
D-Cys helices	2580±343	312±46	604±53	~4 (2580/604≈4)	25	fig. S14, Fig. 5A
L-Cys helices	2541±750	299±64	674±168	~4 (2541/674≈4)	37	fig. S15, Fig. 5A,5C
L-Cys helices	1176±224	257±35	<1176	~0.5	72	fig. S16, Fig. 5C

Table 4.2 Statistical analysis of geometrical parameters of helices obtained from SEM images.

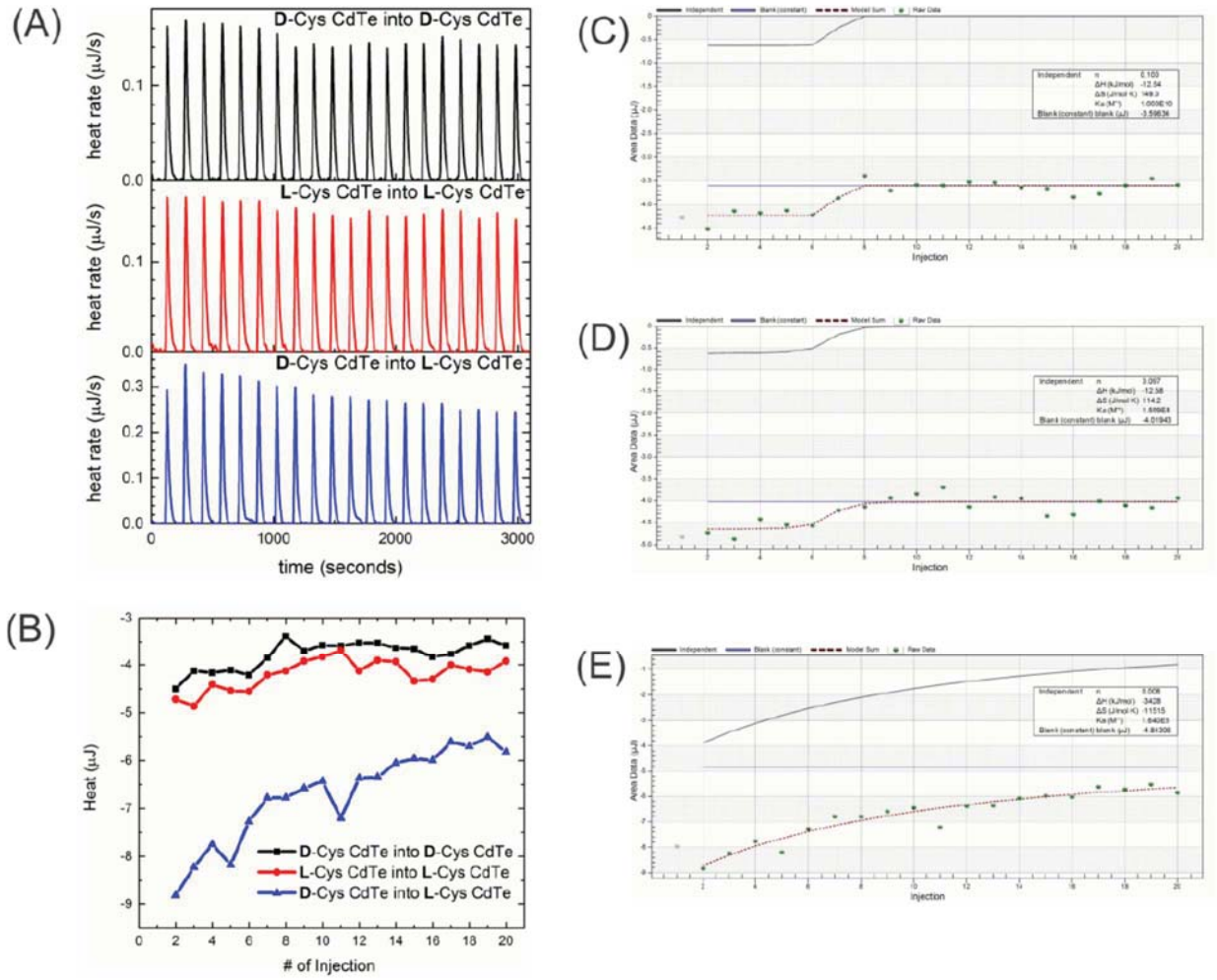

Figure 4.6 ITC data for chiral interactions and their fitting with thermodynamic models. (**A**) Heat rate and (**B**) total heat (integration of peak area) per injection. The first (small volume) injection is discarded. Modeling of (**C**) D-Cys CdTe into D-Cys CdTe, (**D**) L-Cys CdTe into L-Cys CdTe, and (**E**) D-Cys CdTe into L-Cys CdTe. It should be noted that the non-sigmoidal curve shape in (E) presents uncertainty in the determination of binding stoichiometry. For this fitting, we allowed the binding stoichiometry to freely vary during fitting and obtained the thermodynamics with binding stoichiometry = 0.008 and ΔG = -29 kJ/mol. If we assume that the actual binding stoichiometry is higher at 0.100 (the same binding stoichiometry as in the cases of D-Cys into D-Cys and L-Cys into L-Cys), best-fit ΔG becomes -32 kJ/mol, similar to that obtained with no restraints on binding stoichiometry. Therefore, the non-sigmoidal curve shape does not significantly impact the ΔG value determined from ITC data.

The helical shape of the assembled structures appears to be similar to the nanofibers spontaneously formed from peptides (*153*), protein units in the capsids of tobacco mosaic virus (*154*), or chiral macromolecules (*155*). One significant difference compared to these organic nanoscale materials is that inorganic NPs undergo lattice-to-lattice mergers reminiscent of oriented attachment (*85*).

4.2.4 Chiroptical Properties

The helices exhibited characteristic bisignate CD spectra. D- and L-Cys CdTe assemblies displayed mirror-image, opposite-sign CD bands (**Fig. Fig. 4.7 A**). The assemblies retained their rotatory power after one month of storage in the dark at 4 °C (**Fig. 4.8**). After storage, the sample exhibited increased absorbance compared to the original solution, presumably due to the formation of long CdS fibers (**Fig. 4.9**). Co-existing random aggregates, with no observable chiral arrangements, were found to contribute only marginally to the overall rotatory power (**Fig. 4.10**).

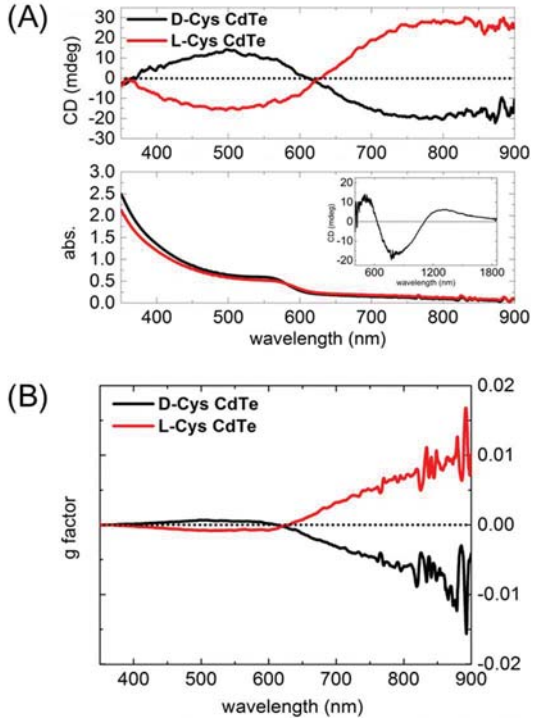

Figure 4.7 Chiroptical Response. (**A**) CD and absorption spectra of D- and L-Cys CdTe assemblies in water (inset shows CD spectra of D-Cys CdTe assemblies in D_2O); (**B**) *g*-factor spectra of D- and L-Cys CdTe assemblies.

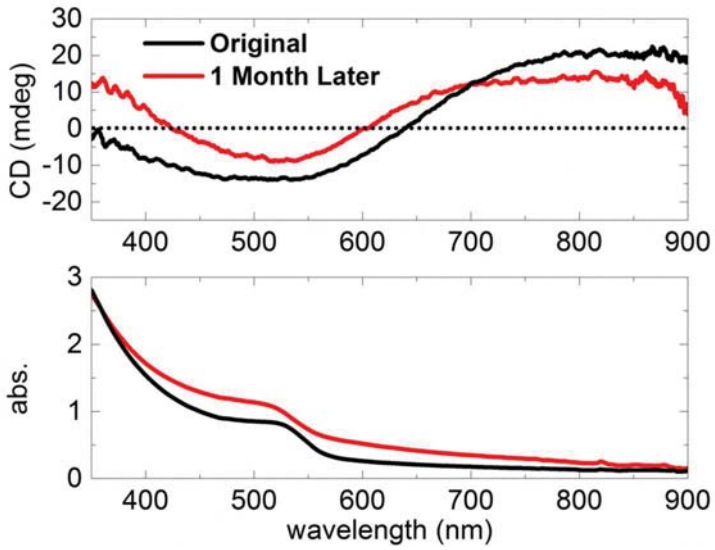

Figure 4.8 Long-term stability of homochiral mesoscale helices. CD and absorbance spectra of an L-Cys CdTe assembly, in the original state and after 1 month of storage at 4 °C in the dark.

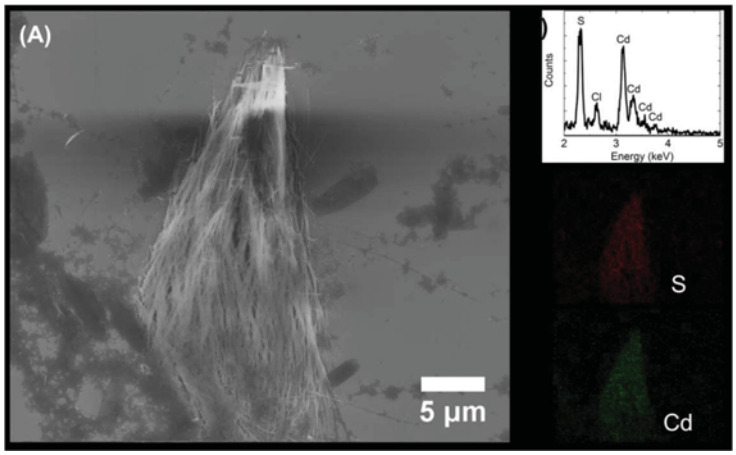

Figure 4.9 CdS nanofibers observed after long-term storage of the CdTe NP dispersions. (**A**) SEM image of bundled CdS fibers forming after 1 month of storage at 4 °C in the dark. As a comparison of size and morphology, note the one helix to the left of the bundle in bright contrast. (**B**) SEM-EDX spectrum showing the presence of Cd, S and Cl (Cl is from the starting material cysteine hydrochloride). Note the absence of Te signal in the range of ~3.7−4.7 keV. (**C**) Elemental mapping of S. (**D**) Elemental mapping of Cd.

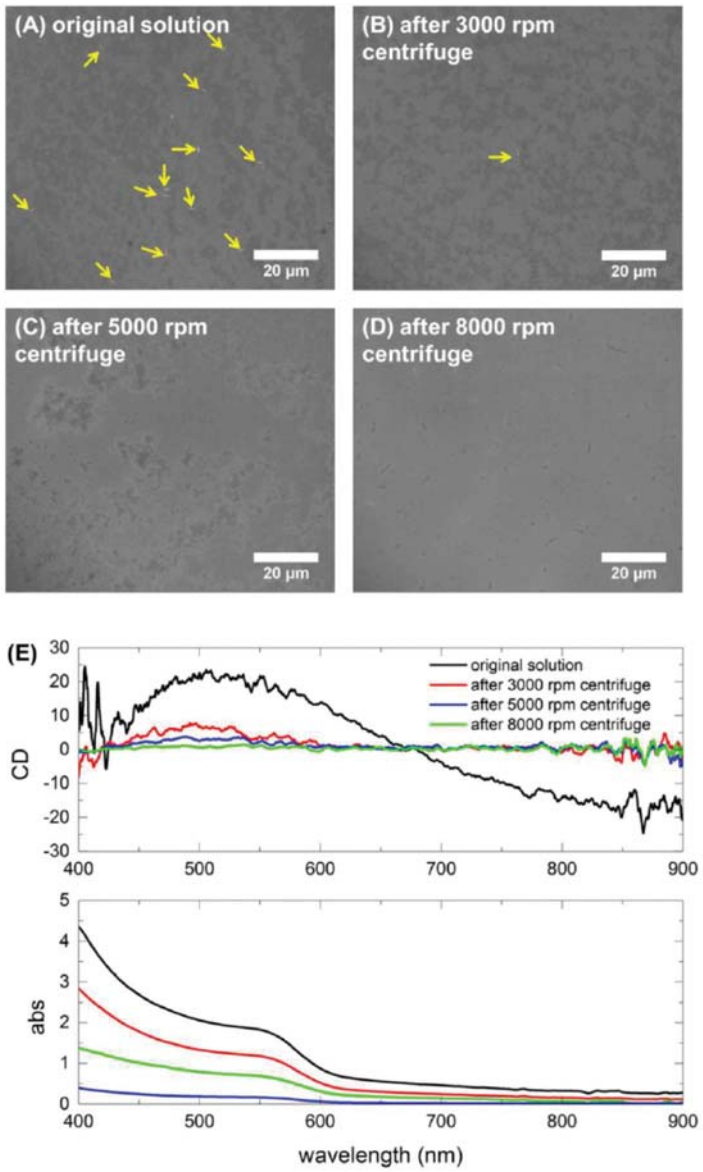

Figure 4.10 Contribution of random aggregates to the overall chiroptical activity. SEM images of (**A**) original assemblies, as well as after (**B**) 3000 rpm centrifugation, (**C**) 5000 rpm centrifugation, and (**D**) 8000 rpm centrifugation. Yellow arrows point to the helices. (**E**) CD and absorption spectra of the corresponding dispersions. The helices present in the original dispersions were mostly removed after centrifugation at 3000 rpm. Subsequent centrifugations of higher speeds reduced the volume density of the random aggregates.

CdTe assemblies showed broad-band Vis-NIR rotatory activity from 350 to 1800 nm (inset **Fig. 4.7A**; **Fig. 4.11**). This specific polarization-active wavelength range may offer unique opportunities in biomedical applications (biological optical window is 650−1350 nm). Considering that the most commonly used wavelengths in optical networking and telecommunications are 1.3 and 1.55 μm, these helices may also find potential use in telecommunication fiber amplifiers (*140*).

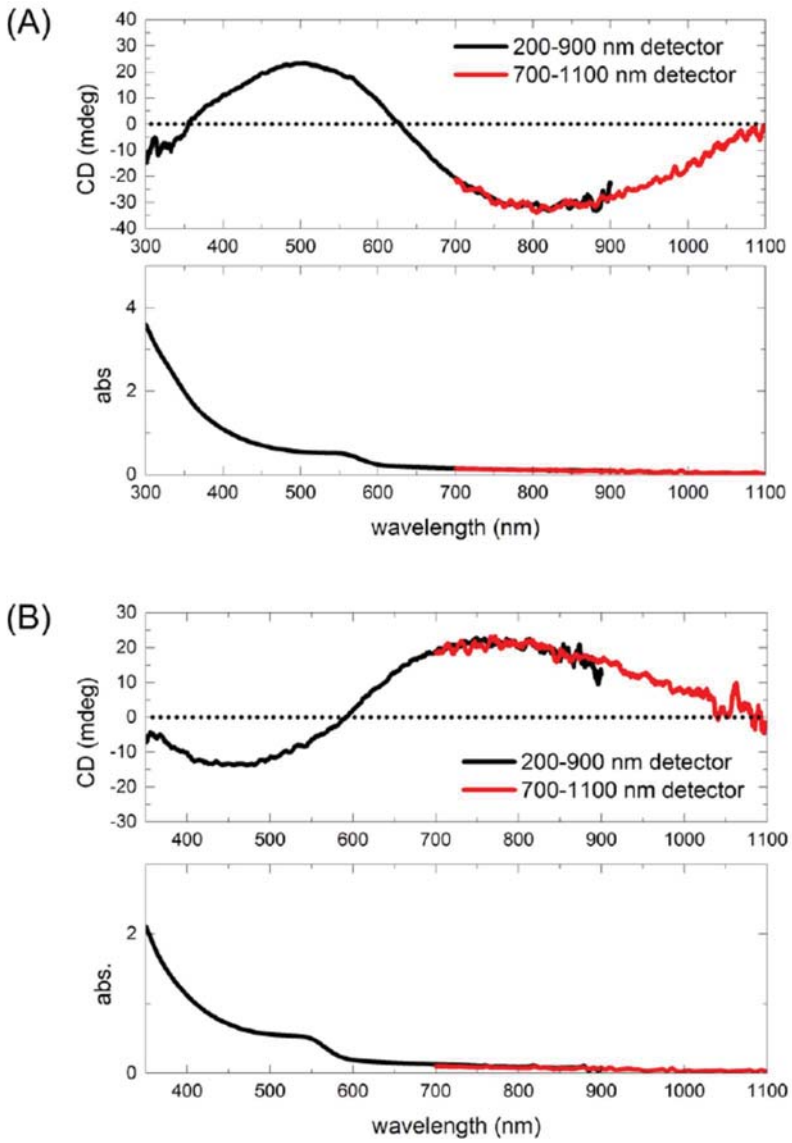

Figure 4.11 Vis-NIR chiroptical response of mesoscale helices. CD and absorbance spectra of (**A**) D-Cys CdTe and (**B**) L-Cys CdTe assemblies in water, using two separate detectors on a Jasco J-815 CD spectrophotometer.

Individual CdTe NPs generally have weak chiroptical activity and low *g* factor values on the order of 10^{-5} (**Fig. 4.12**). Upon assembling into CdTe helices, the *g* factor for both L- and R-helices can reach ~0.01 at λ = 900 nm (**Fig. 4.7B**), which is two orders of magnitude higher than

that of the NPs and a significant improvement over previously reported chiral CdTe nanostructures (*137*, *143*). The *g* factor value is comparable to those reported for chiral nanoscale assemblies based on metallic components such as Au/Ag pyramids (*156*) and Au helices (*23*), as well as helical organic polymers including protein secondary structures (*157*) and polyacetylene derivatives (*158*).

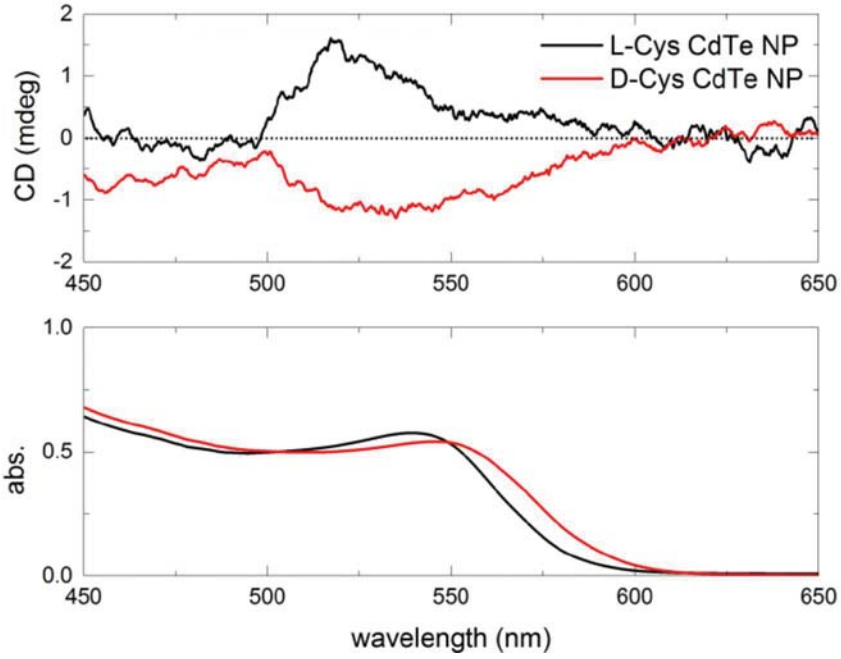

Figure 4.12 CD and absorption spectra of CdTe NPs.

4.2.5 Geometry- and Materials-Driven Chiroptical Response

To understand the relationship between the helix structure and its chiroptical properties, simulations were carried out to examine the influence of each geometrical parameter on chiroptical activity. A finite-difference time-domain (FDTD) Maxwell solver was used to analyze the interaction of circularly polarized photons with model structures employing wavelength scale features.

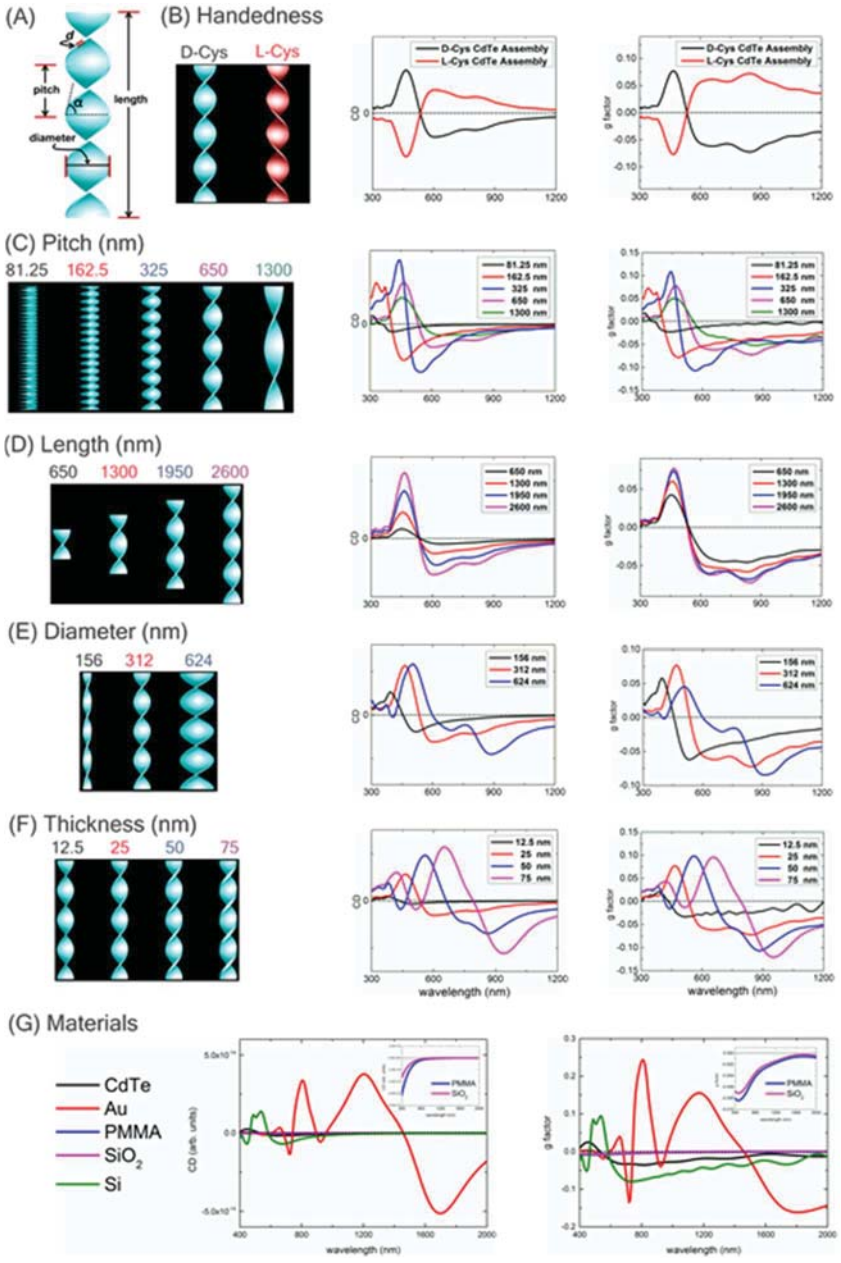

Figure 4.13 Simulations. (A) Illustration of the various geometrical parameters in a typical CdTe helix (*d* represents thickness). Simulated CD and *g* factor spectra with geometrical parameters of variable (B) handedness; (C) pitch; (D) length; (E) diameter; and (F) thickness. (G) Simulated CD spectra and *g* factor spectra for helices of CdTe, Au, PMMA, SiO_2, and Si. The simulated structure is a right-handed helix, pitch size = 650 nm, length = 325 nm, diameter = 312 nm, and thickness = 25 nm.

The five geometrical parameters of interest include handedness, pitch, length, diameter, and thickness (**Fig. Fig. 4.7A**). We kept all geometrical parameters constant except for the one being evaluated, thereby enabling independent investigations into each parameter's effect on CD and *g* factor spectra. Addition of a Te nanowire core within the CdTe helix was found to have no significant impact on the chiroptical response (**Fig. 4.14**), thereby the nanowire core was omitted for clarity. The CdTe helix model structure is as follows: R-helix, pitch = 650 nm, length = 2600 nm, diameter = 312 nm, and thickness = 25 nm. Refractive index, an important optical property used in the simulations, will also be discussed.

Handedness. Opposite handed helices exhibited CD and *g* factor spectra with opposite signs (**Fig. 4.7B**). This validated our simulation setup, which calculates the absorption and scattering cross sections in response to circularly polarized light.

Pitch. Helical pitch size, or the distance for one complete helix turn measured parallel to the helix axis, has a significant influence on structural chirality and rotatory power. To quantitatively study the effect of pitch change on the overall rotatory activity, five helix models were constructed with various pitch sizes (**Fig. 4.13C**). The *g* factor reached a maximum at a pitch size of 325 nm. This can be understood by examining the smallest and largest pitch size models presented here. At a very small pitch size (62.5 nm) or a very large one (1300 nm), the helix increasingly resembles either a solid cylinder or rectangular slab, both of which should exhibit

no rotatory power. Therefore, it is expected that there is an ideal pitch size for optimal *g* factor between these two extremes. The CD spectra shifted moderately to the red with increasing pitch sizes.

Length. The length of the helix does not appear to have a noticeable effect on CD spectral wavelengths (**Fig. 4.13D**). A possible rationalization is that longer helices can be essentially regarded as repeating units of shorter helices with no change in helicity. However, as the helix becomes longer the rotatory power intensifies, which can be explained by considering the longer helices as shorter helices coupled along the ends of the helix.

Diameter. As the diameter of the helices increases, the CD spectra shift to longer wavelengths (**Fig. 4.13E**). To understand this spectral red-shift, we introduce an additional geometry parameter, pitch angle (α), defined as the angle between the helical coil and the base. Looking back at various helical pitch sizes in **Fig. 4.13C**, it is evident that α, pitch and rotatory power are intercorrelated: At pitch sizes above 325 nm, the rotatory power increases as α decreases. Therefore, it is reasonable to expect that when the helix diameter increases, α decreases which ultimately leads to an enhanced rotatory power.

Thickness. The thickness of the helix appears to be closely associated with the CD spectral position (**Fig. 4.13F**). There is a significant red-shift for the CD spectra as the thickness increases: For every 25 nm increase in thickness, there is a corresponding red-shift of ~130 nm. In addition, CD intensity and *g* factor values increases with thickness, suggesting an

enhancement of rotatory power as the helices become thicker. Thicker helices can be regarded as thinner helices coupled along the long axis, inducing the corresponding spectral changes.

Material. An in-depth understanding of the differences between semiconducting, metallic, and organic helices is critical for the application-driven design of chiroptical materials. We compared the simulated CD and *g* factor spectra (**Fig. 4.13G**) for helices of the same geometrical parameters but computationally "substituted" with materials of various refractive indices (**Fig. 4.15**). They included semiconductors (CdTe and Si), metals (Au), ceramics (SiO_2), and organic materials [poly(methyl methacrylate), PMMA]. Si helices, a semiconductor material, have a similar bisignate chiroptical response as CdTe helices. Au helices, on the other hand, show significant differences in CD and *g* factor spectra compared to the semiconductor helices. This is due to strong chiroptical responses from multipole plasmon resonances of Au helices (**Fig. 4.16**) (*159–162*).

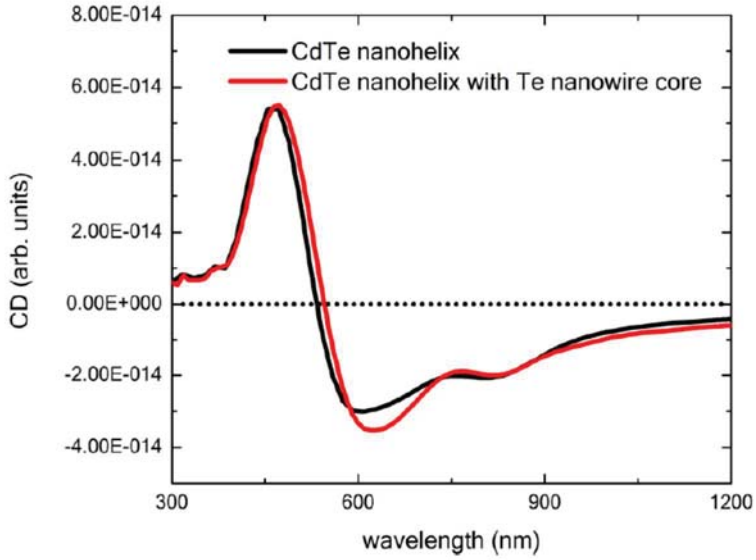

Figure 4.14 Calculated CD spectra of CdTe helix with or without a Te nanowire core. Comparison of simulated CD spectra of a CdTe helix with and without a Te nanowire core (nanowire diameter is the same as the thickness of the helix, nanowire geometry follows the rotation of the helix through the center).

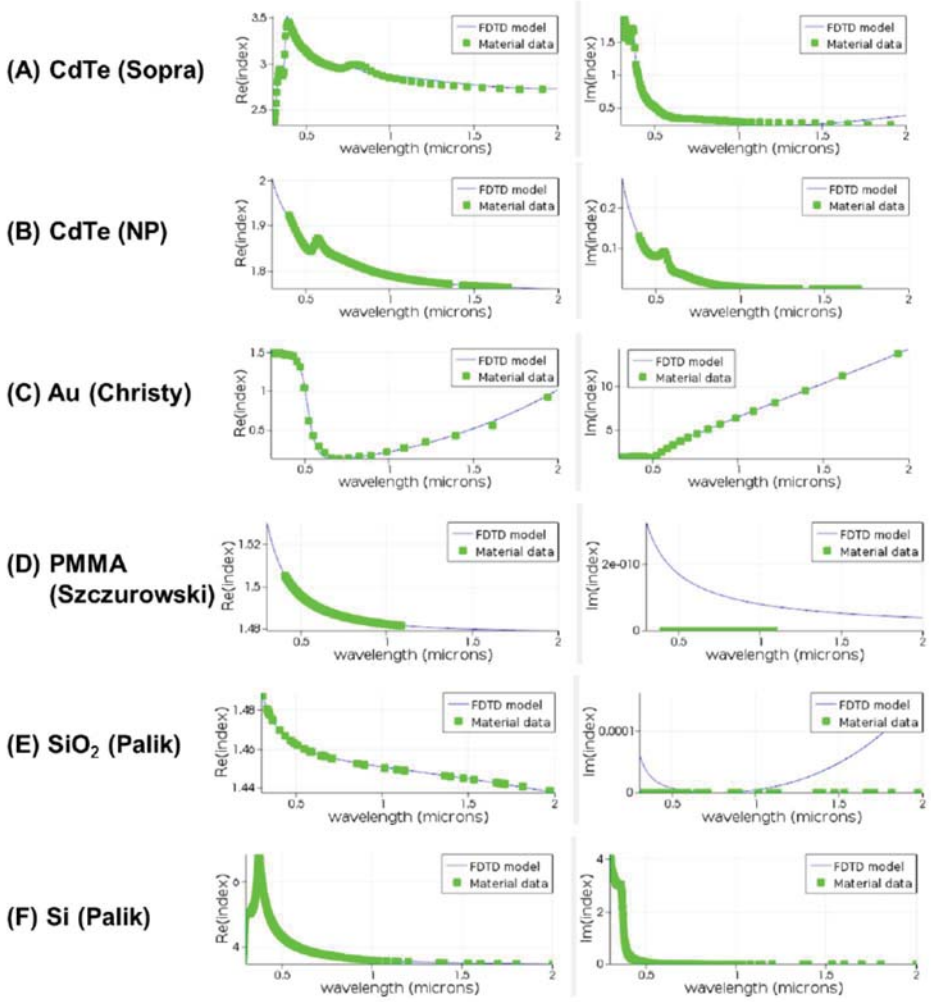

Figure 4.15 xractive index data sets. Real and imaginary parts of the refractive index for (**A**) CdTe (Sopra Material Database), (**B**) CdTe (nanoparticle dataset), (**C**) Au (Johnson and Christy, Lumerical) (**D**) PMMA (Szczurowski, 2013), (**E**) SiO_2 (Palik, Lumerical) and (**F**) Si (Palik, Lumerical). The FDTD model fitting is shown alongside the original dataset. Note that the FDTD fitting of the imaginary refractive index of PMMA and SiO_2 does not adhere to the zero value reflected in the original dataset. This is due to a limitation of the fitting model for zero imaginary refractive index materials. A closer look reveals a very small residual for these fittings (below 10^{-4}), indicating that a good fit is indeed accomplished.

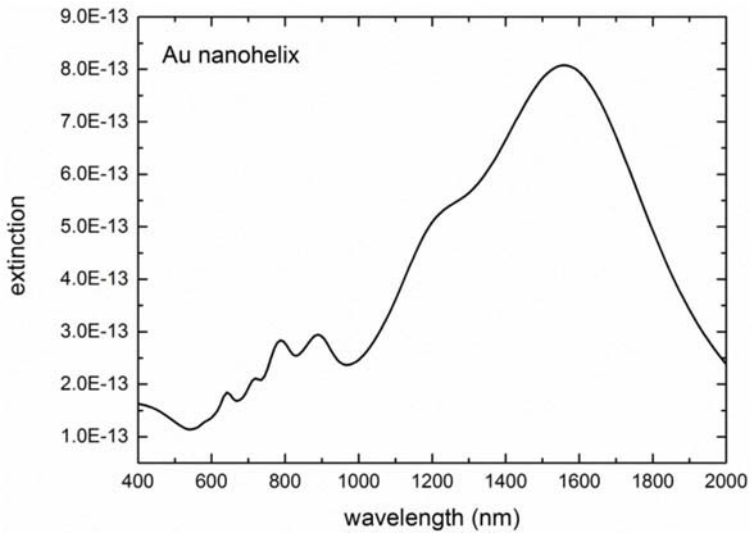

Figure 4.16 Extinction spectrum of Au helices.

Ceramic (SiO_2) or polymer (PMMA) helices show weak chiroptical responses due to the small difference in refractive indices compared to the medium ($n_{SiO2} \approx n_{PMMA} \approx 1.5$; $n_{water} = 1.33$) and the lack of absorption within the materials ($k_{SiO2} = k_{PMMA} = 0$). Non-racemic SiO_2 helices were reported to yield no observable chiroptical response within instrumental sensitivity (*163*), which strengthens the conclusion that the chiroptical response for SiO_2 helices response for SiO2 helices is weak and verifies the calculations in Fig. 4G.

The relative contribution of the absorption and scattering to chiroptical properties is essential for understanding the chiroptical effects observed here and for other chiral inorganic nanostructures. First, by comparing semiconductor and plasmonic helices of identical geometries, one can see that the absorption/scattering ratio under CPL is significantly different (fig. S13). For CdTe helices, this ratio is 1:1.6 and 1:0.9 for left-handed CPL (LCP) and right-handed CPL (RCP), respectively.When it comes to Au helices, the scattering is much stronger

than absorption, with absorption/scattering ratios of 1:5.4 and 1:7.6 under LCP and RCP irradiation, respectively. In the case of ceramic and polymeric helices, scattering is a singular contributor to the chiroptical response, unless the ceramic or polymeric helices are doped with lightadsorbing species. For semiconducting helices, the large contribution of absorption to chiroptical response represents an additional modality in controlling light-matter interaction suitable for fast polarization modulation in optical devices.

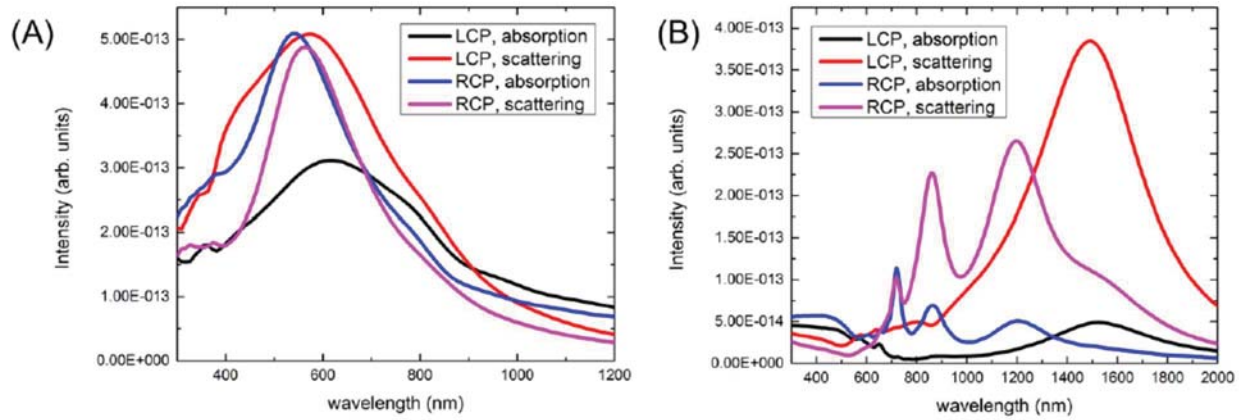

Figure 4.17 Absorption and scattering spectra of Au and CdTe helices. Absorption and scattering spectra of (**A**) CdTe and (**B**) Au helices under LCP and RCP irradiation.

4.2.6 Comparison of Experimental Results and Simulations

The geometry (length, diameter, and pitch) of model helices in simulations is based on statistical analysis of SEM images of experimental helices (**Table 4.2**, **Fig. 4.18**).

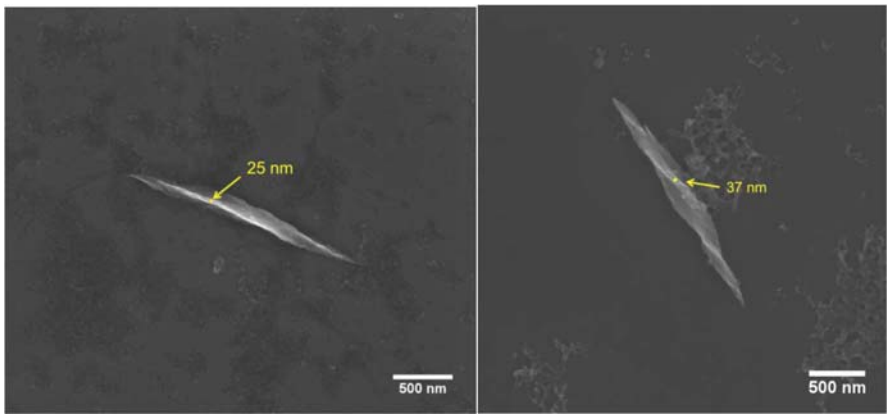

Figure 4.18 Helix thickness. SEM images of R-helix (Left) and L-helix (Right) with thickness highlighted and measured.

The CD spectra calculated with these geometrical parameters demonstrated a nearly perfect match with experimental CD spectra, reproducing the overall shape, spectral positions, and the peak-to-valley intensity ratio (**Fig. 4.19**, **A** and **B**). The broader peaks in the experimental spectra are likely due to some polydispersity of the helices in dispersions (*164*).

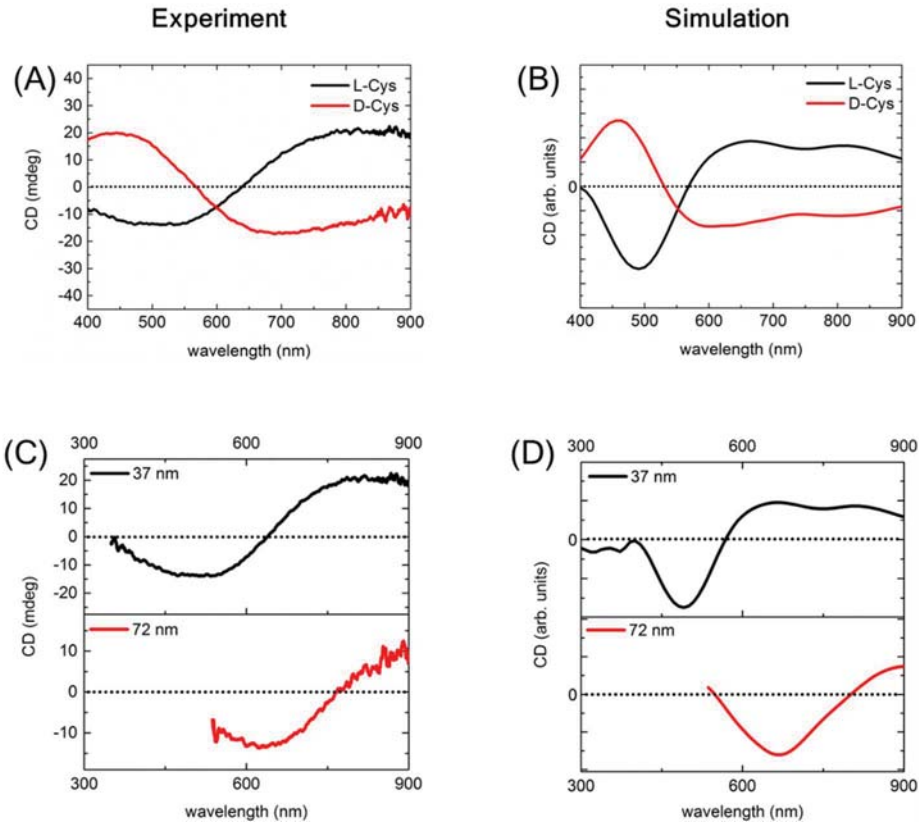

Figure 4.19 Experiment-Simulation Comparison. (**A**) Experimental and (**B**) simulated CD spectra of L- and R-helices. (**C**) Experimental and (**D**) simulated CD spectra of R-helices with a thickness of 37 and 72 nm, respectively.

Experimentally, we observed that for NPs aged for different periods of time, the CD spectra of the resulting self-assembled helices experience a bathochromic shift (**Fig. 4.19**, **C** and **D**). Simulated CD spectra using averaged geometry data yielded similar redshifts. Taking into account that the two geometries differed mainly in thickness (**Fig. 4.18**), it can be concluded that the thickness is the main contributor to this experimental redshift, in agreement with predictions in Fig. 4F. Thickness-dependent chiroptical redshifts have also been reported for Ag deposited on SiO2 helices(*163*), which matched those calculated in Fig. 4G. These findings and

comparisons with literature data further validated the simulation-derived structure-property relationships.

4.2.7 Light-Matter Interaction

Electric field profiles at selected wavelengths provide additional insight into light-matter interaction (**Fig. 4.20**). Strong absorption was expected to occur within the helix at wavelengths below 500 nm because of a large *k*. Indeed, the electric field within the helix is almost zero at 400 nm. The strongest electric field enhancement occurred at 691 nm, close to the helical pitch size (650 nm), demonstrating that light-matter interaction is the most intense when relevant dimensions of the helices draw close to that of the incoming light wavelength. Herein it would be informative to compare the electric field profiles generated by a metallic (Au) or ceramic (SiO_2) helix. When an Au helix is subject to circularly polarized light (CPL) irradiation, strong absorption at all wavelengths is observed within the helix due to very large *k*. At longer wavelengths, the electric field enhancement at the Au helix and water boundary is significantly larger than that for CdTe helix: The electric field enhancement for the Au helix at 927 nm is > 30 (compared to just ~3 for the CdTe helix), most likely due to plasmon resonance (**Fig. 4.16)**. Ceramic (SiO_2) helices, in contrast, exhibit poor electric field enhancement at the helix-water boundary, in addition to a lack of absorption inside the helix ($k = 0$). The comparison of electric field profiles among different helix materials validates the understanding that semiconductor chiral nanomaterials display unique chiroptical responses to circular polarization compared to their metallic or ceramic counterparts.

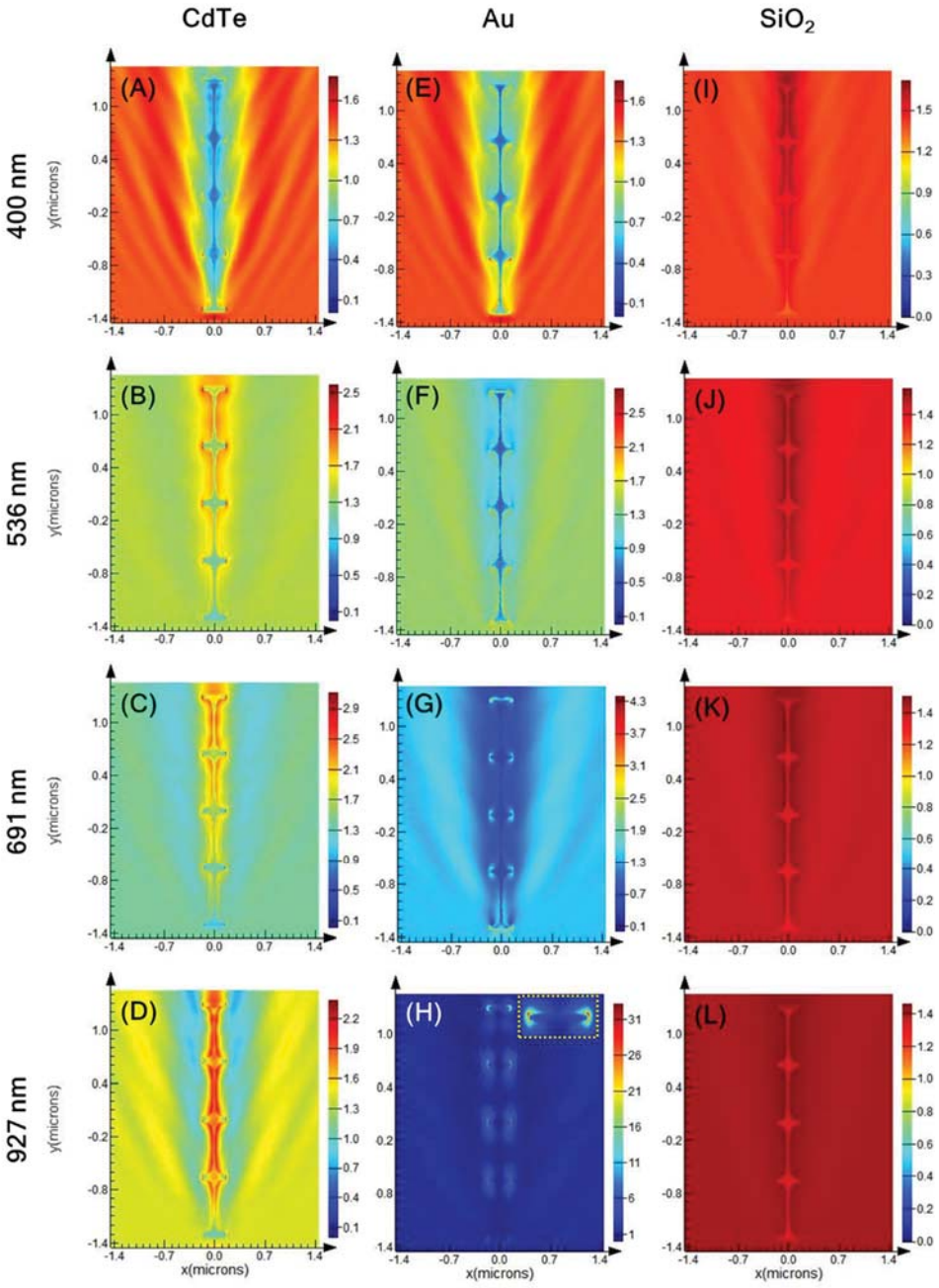

Figure 4.20 Experiment-Simulation Comparison. (**A**) Experimental and (**B**) simulated CD spectra of L- and R-helices. (**C**) Experimental and (**D**) simulated CD spectra of R-helices with a thickness of 37 and 72 nm, respectively.

Electric field profiles are compiled into time-domain animations of electric field isosurfaces (EFIs), three-dimensional (3D) surface representation of equal electric fields. EFIs curl as the electromagnetic pulse travels along the nanostructure, in addition to gradually losing power as light is absorbed and scattered (movies S3 and S4). The curl direction is dependent on the extrinsic chirality of the helix, demonstrating strong modulation due to the difference of electromagnetic properties between the helix and water. The residual electric field after passing through the helix is different for LCP and RCP: RCP irradiation of R-helices showed weaker residual electric field than LCP (**Fig. 4.21**). As expected, achiral structures were subject to identical irradiation conditions, and the resulting EFIs appeared to be discrete without curling (**Fig. 4.22**).

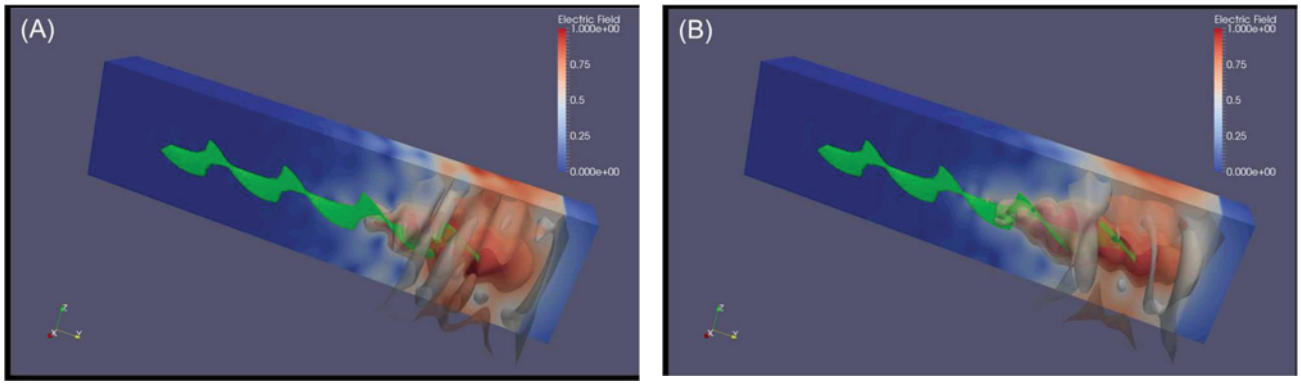

Figure 4.21 EFI movie snapshots. Electric field isosurface (EFI) movie snapshots with (**A**) LCP and (**B**) RCP irradiation of an R-helix.

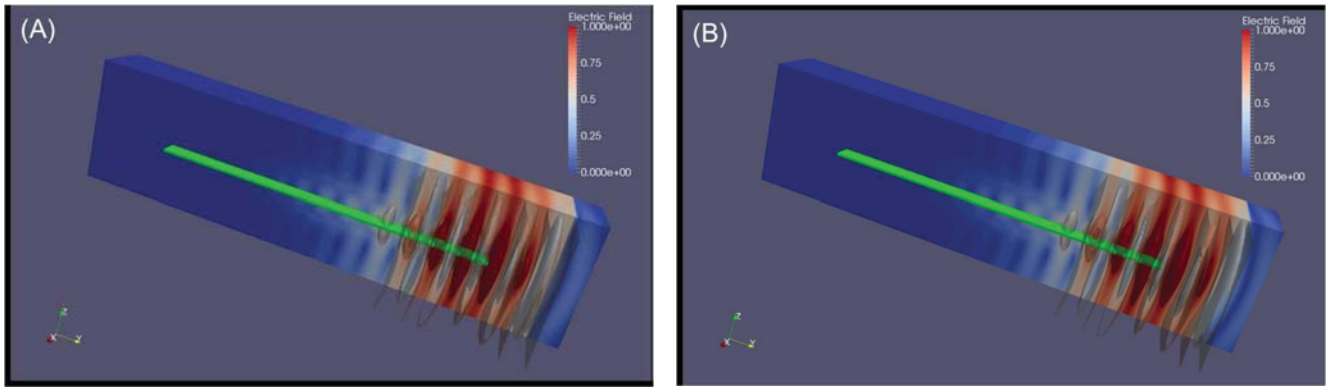

Figure 4.22 EFI movie snapshots. Electric field isosurface movie (EFI) snapshots with (**A**) LCP and (**B**) RCP irradiation upon an achiral nanoribbon. The dimensions of the semiconductor achiral ribbon, are analogous to those of the helix, with a length, width and height of 2600 × 312 × 25 nm3.

4.2.8 Conclusion and Future work

A helix consists of a series of nanorods placed infinitely close, and at an angle to each other (**Fig. 4.23A**). In order to understand the CD spectra of a CdTe R-helix, we constructed a series of right-handed CdTe nanorod dimer (2NR), trimer (3NR), and tetramer (4NR) models. If these simplified models could reasonably reproduce the chiroptical response of the helices, they can then be used to gain physical insight into helix chiroptical properties.

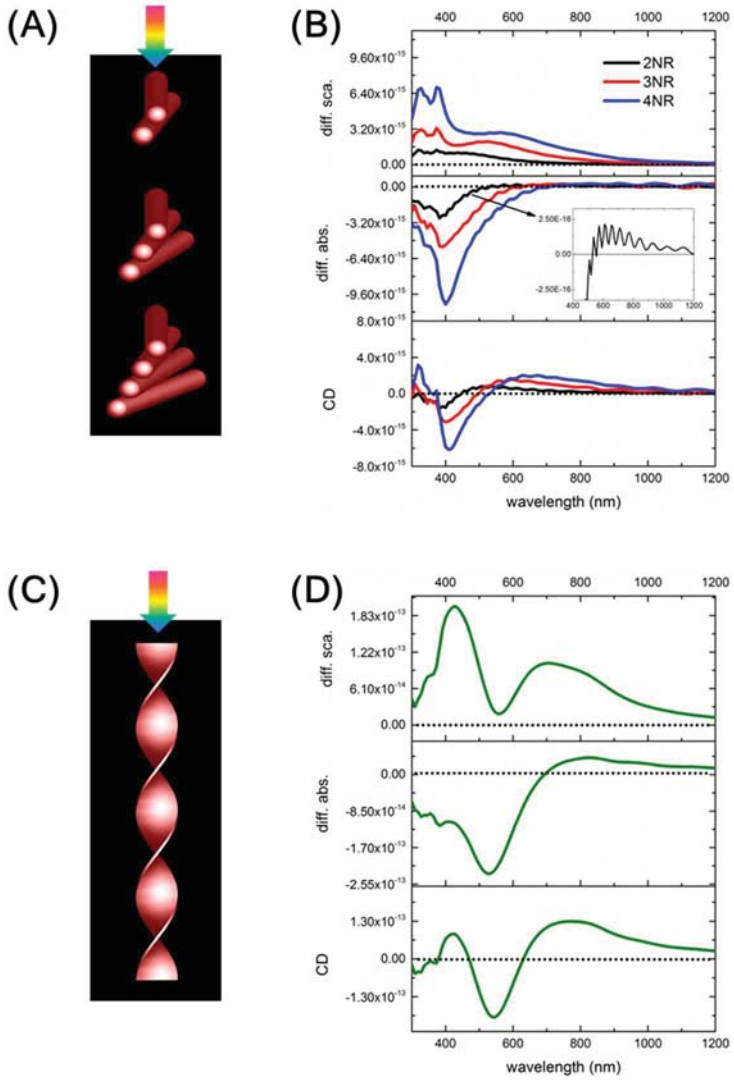

Figure 4.23 Simulated Deconstruction of a Helix. (A) Schematic of CPL irradiating a series of NR dimers (2NR), trimers (3NR), and tetramers (4NR), (B) Differential scattering, differential absorption (inset shows a magnified view for dimer) and CD spectra for 2NR, 3NR, and 4NR, (C) Schematic of CPL irradiating onto a helix, and (D) Differential scattering, differential absorption, and CD spectra for the helix. Nanorod models are 312, 40, and 4 nm in length, diameter and inter-nanorod spacing, respectively, with a 10° dihedral angle.

As the number of nanorods increases from two to four, the bisignate CD spectra of the nanorod models are red-shifted, and increasingly resembled the CD spectrum of the helix (**Fig. 4.23B**). This is confirmation that the deconstruction of a helix into stacked nanorods is valid in reproducing the chiroptical response of the original helical structure.

Now we examine the simplest nanorod model - the dimer model. CdTe dimer exhibits a bisignate CD spectrum. The spectral shape appears similar to that reported for certain Au dimers, which has been explained by dipole coupling theory (*165*, *166*). It may appear that CdTe and metallic dimers share similar chiroptical responses, however, further simulations by substituting CdTe dimers with Au or Ag dimers while retaining the original dimensions proved such assumptions premature: Both Au and Ag dimers show complex multipole plasmon resonances (**Fig. 4.24A**). The apparent discrepancy between previous reports and our work is due to the fact that the size and aspect ratio (length = 312 nm, width = 40 nm, aspect ratio ≈ 8:1) used in our simulations were larger than those previously reported. At this specific size and aspect ratio regime, multipole plasmon resonances gain provenance (*159–162*) and therefore the dipolar model that predicts a simple bisignate CD spectrum is simply not applicable.

Contrary to the multipole plasmon resonances observed for metallic dimers, semiconductor dimers of various materials (CdTe, Si, or GaAs) all produced a bisignate CD spectral shape (**Fig. 4.24B**). This arises from the inability of semiconductors to generate multipole resonances even at large sizes and aspect ratios, presumably because semiconductors generally have lower free electron density compared to metals (*167*).

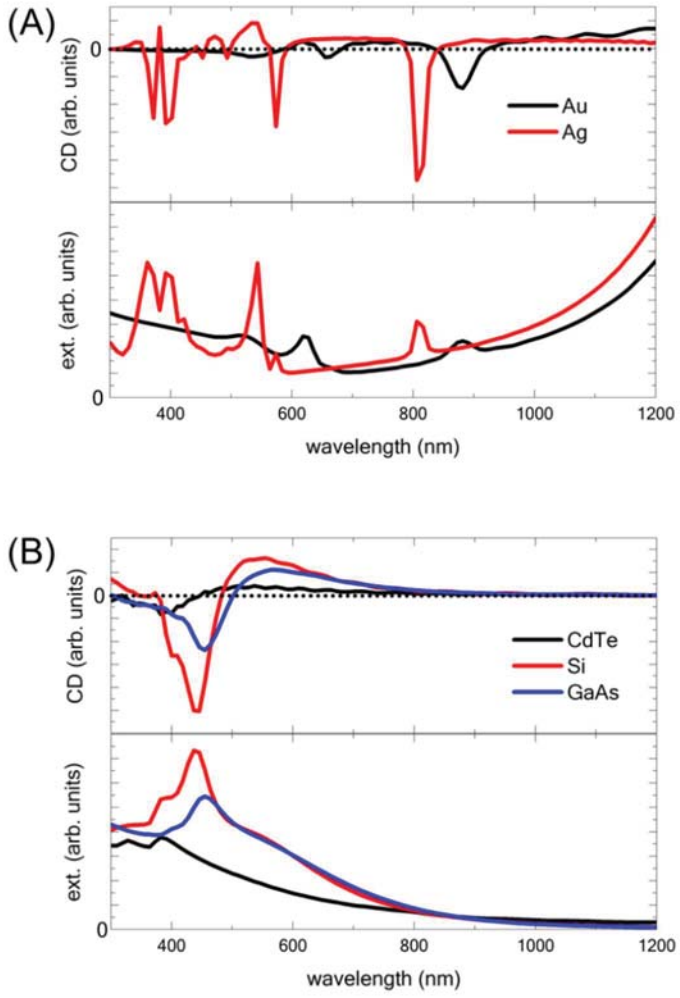

Figure 4.24 Nanorod dimer simulations. (**A**) Simulated CD and extinction spectra of Au and Ag nanorod dimers. (**B**) Simulated CD and extinction spectra of CdTe, Si and GaAs nanorod dimers.

4.2.9 Materials and Methods

4.2.9.1 Synthesis of Cys-CdTe NPs

The synthetic procedure was adapted from a previous report (*168*) with modification. Briefly, $Cd(ClO_4)_2 \cdot 6H_2O$ (0.985 g) and D- or L-cysteine hydrochloride monohydrate (0.990 g) were

dissolved in 125 mL deionized water, followed by adjusting the pH to 11.2 with 1 M NaOH. This solution was placed in a three-neck round-bottomed flask and purged with N_2 for 30 min. H_2Te gas (generated by reacting 0.05-0.10 g Al_2Te_3 with 10 mL of 0.5 M H_2SO_4) was slowly passed through the solution. The solution was then allowed to reflux under N_2 at 100 °C for 60 min to obtain the Cys-CdTe NPs used in this work. For storage, the NP solution was thoroughly purged with N_2 for at least 30 min and then kept in the dark at 4 °C.

For both D- and L-Cys CdTe NPs, TEM analysis showed similar size distribution and electron diffraction where the observed d-spacing exists in both zinc blende (cubic) and wurtzite (hexagonal) structures, with the zinc blende structure being predominant (**Fig. 4.25**). The size of the NPs was ~3.2 nm. The size was further confirmed by empirical fitting functions (*169*) with the wavelength of the first excitonic absorption peak (~550 nm).

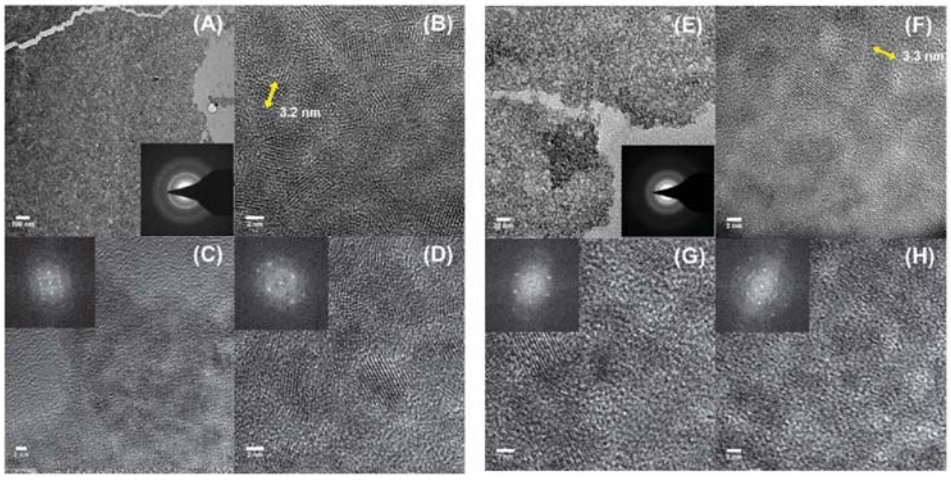

Figure 4.25 TEM images and crystal lattice of CdTe NPs. TEM image of D-Cys CdTe NPs at (**A**) low magnification, (**B**) high magnification, (**C**) with electron diffractogram corresponding to a [100] hexagonal structure (also possible to index as a twinned cubic structure), and (**D**) with electron diffractogram corresponding to a [211] cubic structure. TEM images of L-Cys CdTe NPs at (**E**) low magnification, (**F**) high magnification, (**G**) with electron diffractogram corresponding to a [111] cubic structure, and (**H**) with electron diffractogram corresponding to a [110] cubic structure.

4.2.9.2 Preparation of Helical Assemblies

An aging process of the original aqueous NP solution was found to be critical for the preparation of helical assemblies. Assembly into helices only occurred when the original NP aqueous solution was allowed to age under dark at 4 °C for one day or more. Residual oxygen was expected to react with NPs. Black precipitates could be observed at the bottom of the container as aging proceeded. The aging process, accompanied by a decrease in NP size, could be followed spectrally by a blue-shift of the first excitonic absorption peak (**Fig. 4.26**). The rotatory power of the NPs appeared relatively stable over the same period (**Fig. 4.27**).

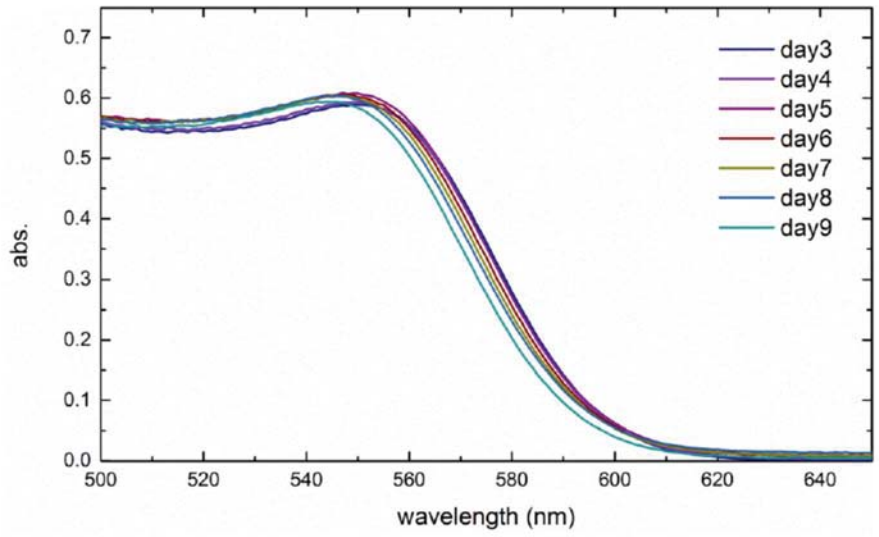

Figure 4.26 Absorption spectra of CdTe NPs during aging. UV-vis absorption spectra of D-Cys CdTe NPs over the course of six days.

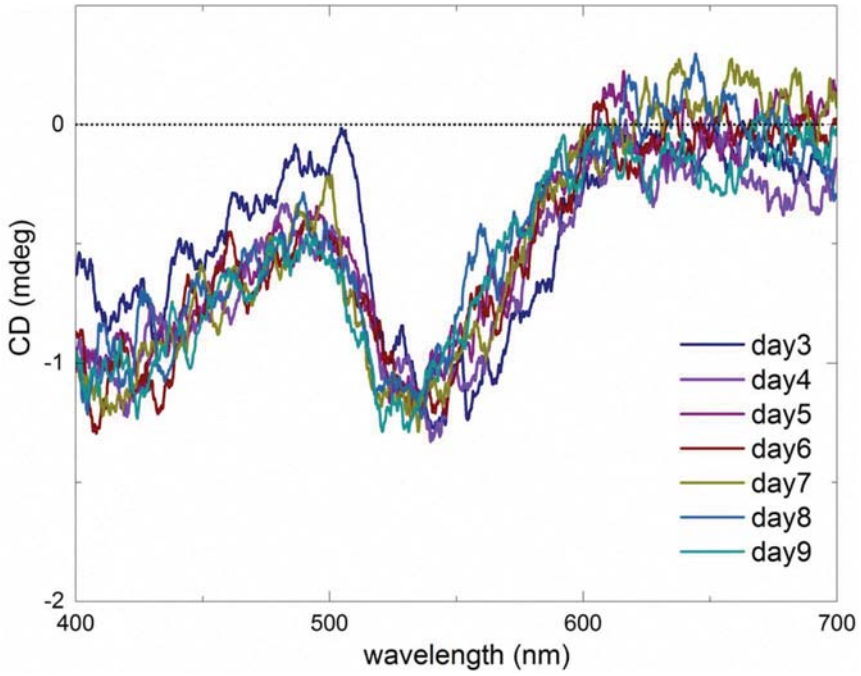

Figure 4.27 CD spectra of CdTe NPs during aging. CD spectra of D-Cys CdTe NPs over the course of six days.

When the NPs were sufficiently aged to be assembled, a solvent exchange step was performed to transfer the NPs from water to methanol. The NP aqueous solution and methanol were mixed at a volume ratio of 1:1.5 to precipitate the NPs. This solution was then placed in a centrifuge at 1500 rpm for 3 min, the supernatant discarded, and the precipitate re-dispersed in methanol. At this point, the excess Cys ligand was removed and the NPs were considered "activated" for assembly. Solution CD measurements demand relatively high solution transparency, therefore the as-assembled helices in methanol were transferred to water where they were dispersed with ease. To achieve this, the methanolic solution was placed in a centrifuge at 1500 rpm for 3 min, the supernatant discarded, and the precipitate re-dispersed in water. This aqueous solution was then

subjected to another centrifugation step (2000 rpm, 3 min) with the supernatant being used for CD studies (this additional centrifuge step was skipped for formation mechanism studies presented in **Fig. 4.4 A-K**. The entire procedure for the preparation of helical assemblies is illustrated in **Schematic Figure 1**. It should be noted that D_2O was used as the solvent instead of water for the NIR CD measurement in the inset of **Fig. 4.7A**, because D_2O absorbs less in the IR region than water and therefore is ideal for CD data collection with a wider usable wavelength range.

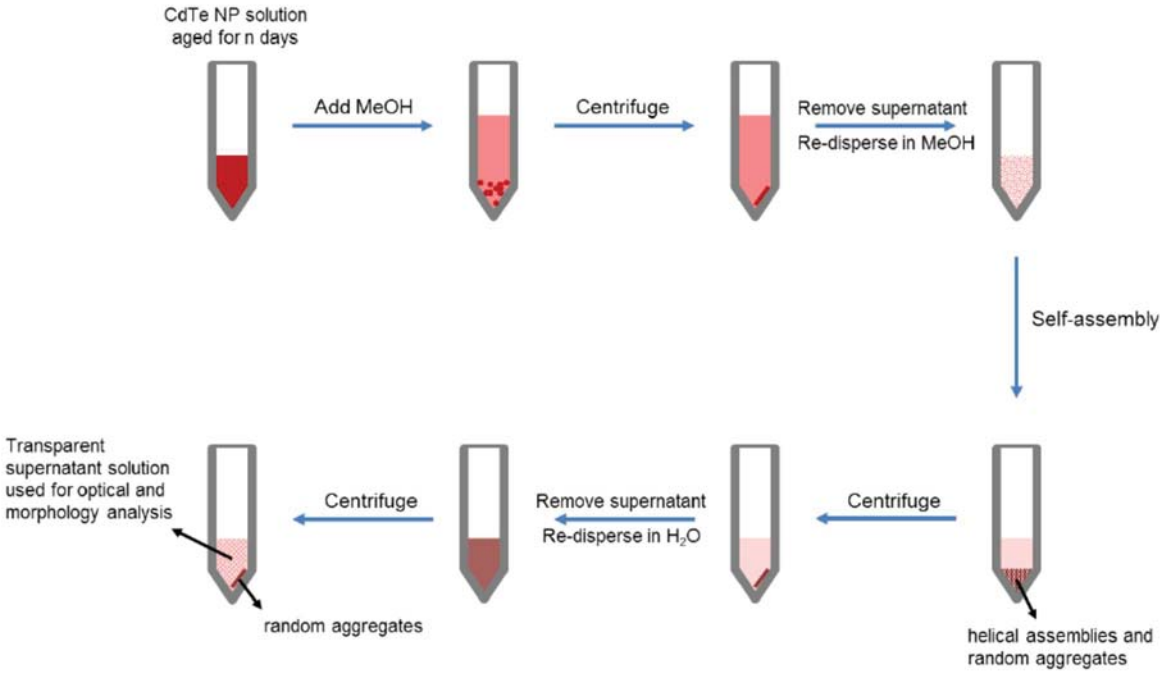

Figure 4.28 Experimental methods. Preparation of helical assemblies in Eppendorf vials.

4.2.9.3 CD Instrumentation

JASCO J-815 (two PMT detectors of 200–900 and 700–1100 nm ranges) and J-1700 (one PMT detector of 200–800 nm range and two InGaAs NIR detectors of 800–1600 and 1600–2500 nm ranges) CD spectrophotometers were used for CD studies. Typical scanning parameters were as follows: scanning speed = 100 nm/min, data pitch = 0.1 nm, bandwidth = 1 nm (NIR bandwidth = 20 nm), digital integration time (D.I.T.) = 4 s, and one accumulation. The anisotropy (g) factor was calculated according to the following equation: $g = \frac{CD}{32980 \times abs.} = 0.0000303214 \times \frac{CD}{abs.}$ $g\ \text{factor} = \frac{CD}{32980 \times abs.} = 0.0000303214 \times \frac{CD}{abs.}$. CD spectra were stopped at wavelengths where the high tension voltage on the PMT detector exceeded the maximum (800 V) allowed for reliable CD data collection.

4.2.9.4 Imaging

All electron microscopic images were taken with facilities of Michigan Center for Materials Characterization at University of Michigan. FEI Nova 200 Nanolab Dualbeam FIB was used for SEM imaging and EDX elemental analysis. JEOL 3011 was used for TEM imaging and SAED analysis. JEOL 2100F was used for STEM imaging and EDX elemental analysis. Tomogram reconstruction software (eTomo) and visualization software (Amira) were used to generate 3D tomography.

4.2.9.5 ITC Studies

TA Instruments Nano ITC Low Volume isothermal titration calorimeter was used. The excess ligand in the original NP aqueous solution was removed by centrifuging at 1500 rpm for 3 minutes and then re-dispersed in water. Both D-Cys and L-Cys CdTe NPs have the same size (3.2 nm), concentration (0.02 mM) and pH value (9.9). The NP solution in the sample cell and the syringe has the same concentration (0.02 mM). The syringe volume is 50 μL, with 2.5 μL per injection (20 injections in total) and an injection interval of 150 seconds. An initial baseline was collected for 100 seconds before the first injection. The temperature is set to 22 ℃. The stirring rate is 350 rpm. NanoAnalyze software was used to analyze the raw heat rate graphs and to model with a constant blank model and an independent model.

4.2.9.6 Simulations

The CD and g factor spectra were calculated using a commercial FDTD software package (Lumerical Solutions Inc., http://www.lumerical.com/tcad-products/fdtd/). We used total-field scattered-field (TFSF) sources that surround the structure being modelled. Circularly polarized light was generated by positioning two TFSF sources along the same forward axis at 90° angle and with a phase difference of either -90° (left-handed circularly polarized light) or 90° (right-handed circularly polarized light). Two analysis groups utilizing box power monitors monitored the absorption and scattering cross sections (extinction is the sum of absorption and scattering). The FDTD simulation region was defined by a larger box monitor with stretched coordinate perfectly matched layer (PML) and non-uniform mesh type. Frequency profile monitors were inserted in the total field region to calculate electric field enhancement in 2D. The accuracy of

the simulation model was verified and validated with a chiral gold nanorod dimer structure reported in (*131*), where the simulated CD spectrum (**Fig. 4.29**) produced an excellent match with the experimental one with positive-negative bisignate wave-shape at similar wavelength region. The refractive index for water is 1.33. The refractive index for CdTe is derived from the Sopra Material Database (http://www.sspectra.com/sopra.html). For comparison, another CdTe refractive index dataset derived from individual CdTe NPs (with first excitonic absorption peak at 550 nm) was used to simulate a helix (see refractive index datasets in **Fig. 4.15**. The resulting CD spectrum fails to yield the characteristic bisignate spectral shape observed experimentally (**Fig. 4.30**). This discrepancy can be explained by the difference in both the real and imaginary part of two refractive index datasets. The unsatisfactory match obtained using the refractive index for individualistic CdTe NPs also provides indirect evidence that CdTe NPs within the assembly were closely packed and strongly coupled, and that it is no longer appropriate to consider them individualistic.

Helices may adopt random orientations during CD measurement, therefore simulations took this into account except when explicitly stated otherwise). Simulations of random orientation were achieved as follows: The helix was allowed to rotate along the y-axis every 30° from 0 to 150° as well as along the z-axis every 30° from 0 to 330°, and the final CD and g factor spectra were averaged over a total of 72 orientations (multiplication of 6 rotations along y-axis and 12 rotations along z-axis). Convergence tests with different mesh sizes were performed to determine the best balance between computational time restraints and simulation accuracy. Simulations on one orientation of the CdTe helices (CPL on axis with helix) with 25 nm or 10 nm mesh size

produced similar CD spectra, therefore we used 25 nm mesh size for CdTe helix simulations. There is an exception to this mesh size in constructing electric field profiles, where a finer mesh size of 5 nm was adopted to enhance the profile resolution.

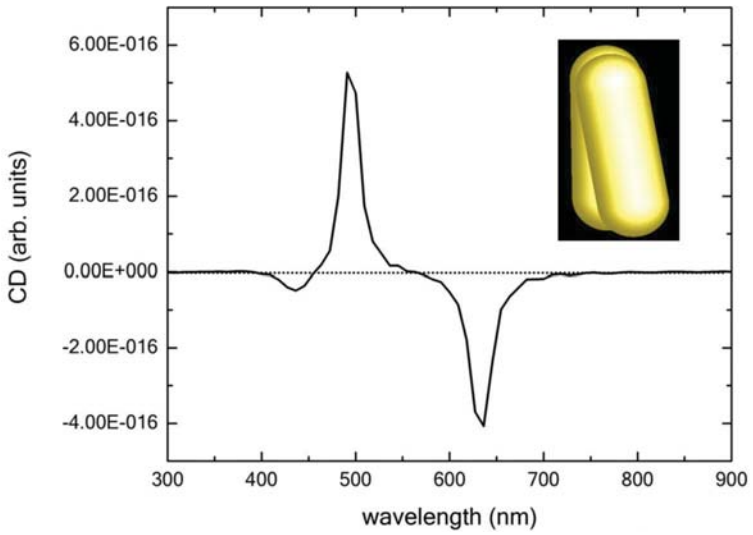

Figure 4.29 Verification of the computational model. Both the positive-negative bisignate spectral shape and the wavelength region match up well with the reported experimental CD spectrum.

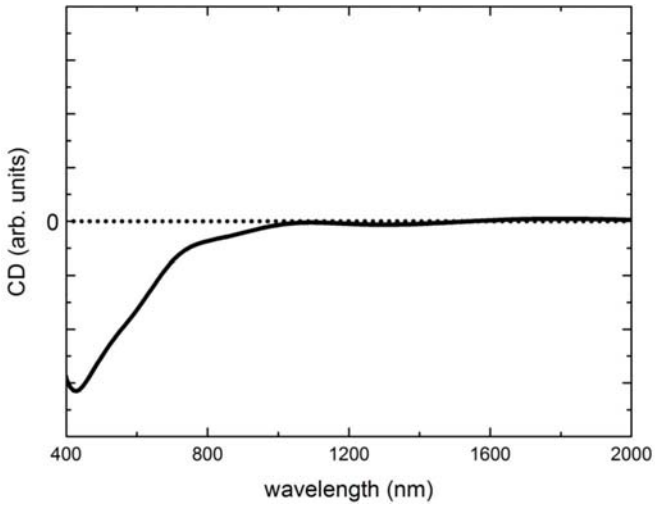

Figure 4.30 Simulations using CdTe NP refractive index. Simulated CD spectrum of an R-helix using CdTe NP refractive index (dataset supplied by Dr. Evren Mutlugun).

In the discussion of refractive indices, the simulated structure was a right-handed helix, pitch size = 650 nm, length = 325 nm, diameter = 312 nm, and thickness = 25 nm. The relatively small model size was intended to reduce the computational time for Au, which has a small real refractive index. Consequently, very small mesh sizes and longer simulation times were required to provide accurate results for Au. Convergence tests with three different mesh sizes of 5, 2.5, or 1.25 nm yielded very similar CD spectra, indicating that a mesh size of 5 nm was sufficient for accurate simulations under reasonable simulation time.

The mesh size for nanorod models (2NR, 3NR, and 4NR) was 0.5 nm, though a larger mesh size such as 1 nm did not yield significantly different spectra.

3D animations of electric field isosurfaces (EFIs) were produced in Paraview, using electric field vector values derived from Lumerical simulations.

4.2.10 Supporting Information

Percent yield

The percent yield for D-Cys and L-Cys CdTe assemblies is estimated to be the ratio of the number of NPs incorporated in all helices (Np) and the number of original NP (Np*). To obtain Np, we dropcast 3 μL of helices solution onto a silicon shard for SEM imaging. We randomly selected 30 regions (each with a surface area of 0.01368 mm2) and determined the amount of helices appearing in these areas by manual counting. Taking into account of the entire droplet surface area, we estimated the number of helices (Nh) in each 3 μL droplet. Separately, 30

images of random individual helices were taken with the intention of obtaining their average length (l) and diameter (⌀) using ImageJ analysis software. We assumed a constant thickness of 25 nm for all helices. Because of the tapered shape of the helices, the volume of an "untwisted" helix is considered to consist of three cuboids and two triangular prisms at the ends. Based on this structural assumption, the volume of a helix (Vh) = $34\times l\times\varnothing$.

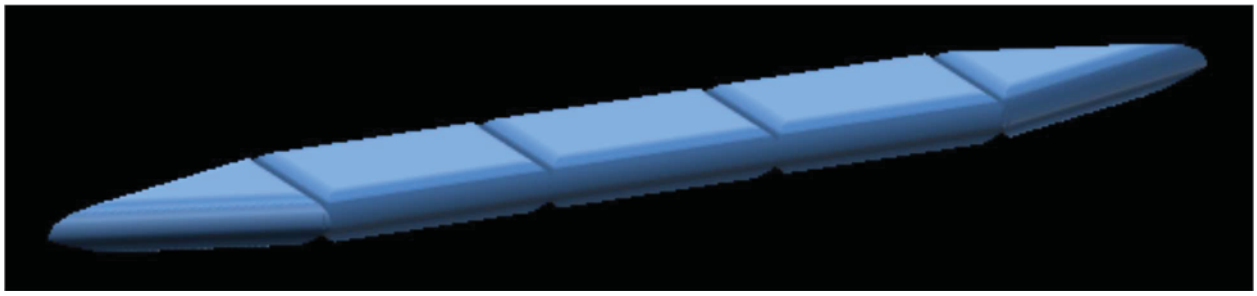

Figure 4.31 Schematic drawing of an "untwisted" helix

The size of the NPs is 3.2 nm. As CdTe NPs are tetrahedral in shape, the volume of a NP is $3.2^3\sqrt{2}$ = 3.86 nm^3. The average number of NP per helix ($N_{a,p}$) = $v_h 3.86$. The number of NP in all helices (N_p) = $N_{a,}\times N_h$.

The absorbance of a 4-times-diluted L- and D-CdTe NP solution is 0.63 and 0.55, respectively. Together with the NP size (3.2 nm), the original NP concentration can be estimated to be 1.28E+19 per liter and 1.12E+19 per liter, for L- and D-CdTe NPs respectively. For 3 μL solution, the number of original L- and D-CdTe NPs (N_{p*}) is calculated to be 3.85E+13 and 3.36E+13, respectively.

The percent yield of helices (N_p/N_{p*}) is 0.0892% ± 0.0063% for L-Cys CdTe assemblies and 0.0944% ± 0.0038% for D-Cys CdTe assemblies. From this percent yield calculation, we see that only a small fraction of NPs self-assembled into helices, whereas the vast majority of NPs formed

random aggregates. Despite the low concentration of helices in solution, the CD intensity and rotatory power of the helices remain excellent owing to their high structural chirality.

	length (l)	diameter (⌀)	thickness (d)	Volume per helix (V_h)	number of nanoparticles per helix ($N_{a,p}$)	number of helices (N_h)	number of nanoparticles in all helices (N_p)	number of original nanoparticles (N_p*)	percent yield (%)	average percent yield (%)	std dev. (%)
L-CdTe 1	4380	378	25	3.10E+07	8.04E+06	4.23E+03	3.40E+10	3.85E+13	0.0884		
L-CdTe 2	4125	363	25	2.81E+07	7.27E+06	4.34E+03	3.15E+10	3.85E+13	0.0819	0.0892	0.00628
L-CdTe 3	4333	384	25	3.12E+07	8.08E+06	4.64E+03	3.74E+10	3.85E+13	0.0973		
D-CdTe 1	3443	331	25	2.14E+07	5.53E+06	5.64E+03	3.12E+10	3.36E+13	0.0929		
D-CdTe 2	3628	350	25	2.38E+07	6.17E+06	5.43E+03	3.35E+10	3.36E+13	0.0997	0.0944	0.00381
D-CdTe 3	3567	339	25	2.27E+07	5.87E+06	5.19E+03	3.05E+10	3.36E+13	0.0907		

Table 4.3 Percent Yield Calculations.

Enantiomeric Excess (e.e.)

The number of helices is obtained by counting from SEM images taken at random regions of the drop casted sample.

$$Helices\ e.e.=\frac{\text{absL}-\text{helices}-\text{absR}-\text{helice}}{\text{absL}-\text{helices}+\text{absR}-\text{helices}}$$

NPs e.e is obtained by comparing the UV-vis absorbance of D-Cys and L-Cys CdTe NPs with the same 4 times of dilution.

$$NPs\ e.e.=\frac{\text{absL}-\text{absD}}{\text{absL}+\text{absD}}=\frac{0.63-0.55}{0.63+0.55}=0.068$$

4.3 Hierarchical Assembly of copper sulfide nano-leaves (Cu_2S NLs) and Their reversible chirality

Contributions: Kotov, N.A. supervised the project. Yeom, J. Kim, J, -Y, Kwon J. and Lee, Y. carried out Cu2S NLs synthesis, assembly, and characterization. G. Silveira took electron tomography. J.-Y Kim performed experiments on reversibility of NL assemblies and take electron microscopic images. Yeom, J. and Kim, J. -Y. analyzed the data. J, -Y Kim wrote the manuscript.

The copper sulfide represents a promising material for photovoltaic and plasmonic devices. The ligand-directed chiral assembly method developed in section 4.2 could be versatile to create chiral structures with similar material system. Our group has been reported spontaneous self-assembly of copper chalcogenide (β- Cu_2S) NPs into nanochains and, subsequently, to nano-leaves (NLs) with continuous crystal lattice.(*170*) Similarity in the spontaneous assembly procedures of Cu_2S and CdTe NPs, we hypothesize that modified the synthetic protocol of β-Cu_2S NPs having chiral surface ligand can result in chiral assemblies of NPs. With addition of cysteine molecules, we obtained twisted stack structure of Cu_2S NLs having distinct direction of chirality.

4.3.1 Synthesis of chiral Cu_2S NLs assemblies

We synthesized chiral Cu_2S nanostructures using modified synthesis procedure from the previous study.(*171*) Thioglycolic acid (TGA) and *L*- or *D*- cysteine aqueous dispersions was used as stabilizers with 1:1.8:6.6:0.5 molar ratio of [Cu^{2+}]:[TGA]:[Cysteine]:[TAA (thioacetamide)]. After 4h reaction at 85 ℃, the sample was rinsed with distilled water, and then incubated at room temperature for 20 h. The incubation process yielded chiral self-assembled

structures with distinctive handedness depends on chirality of involved cysteine. The corresponding morphology of submicron self-assembled NLs is shown in **Fig. 4.32 A** and **B**. We can observe that leaf-like nanostructures are stacked in a clockwise or counterclockwise direction like cholesteric liquid crystals with *D*-cysteine and *L*-cysteine respectively. The nano-leaf is about 1 μm long with 50 nm width, and the average number of leaves in assembled structure was about five. Three dimensional (3D) electron tomography reconstructed from series of scanning transmission eleectron microscopy (STEM) images of assembled NLs vividly shows the assembled patterns. (**Fig. 4.33A)**

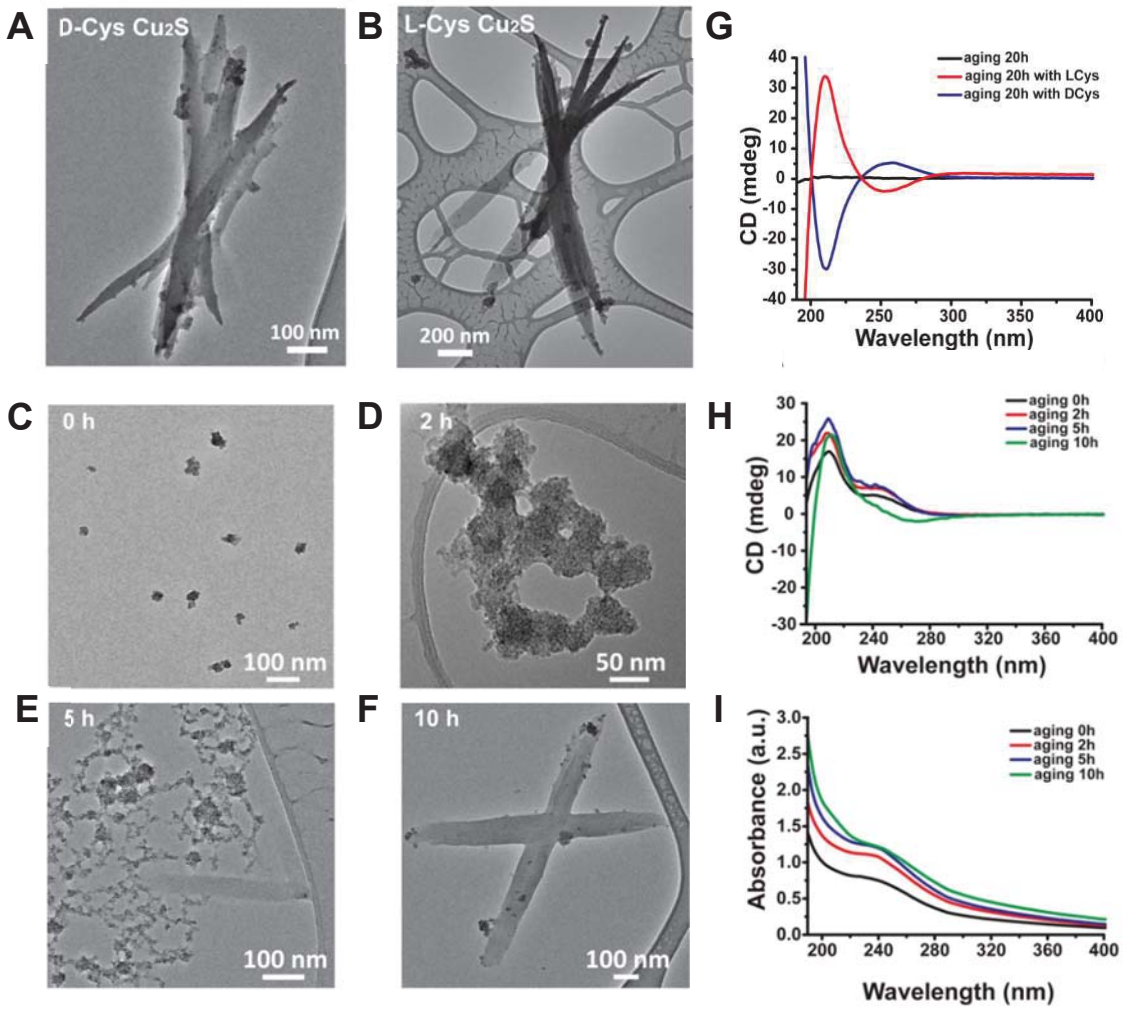

Figure 4.32 Structure and Optical Properties of Copper Sulfide(Cu_2S) Nano-leaves Assemblies. (**A, B**) TEM images of nano-leaves assemblies from D-Cys (A) and L-Cys (B) capped Cu_2S NPs. (**C, D, E, F**) TEM images at different stages of Cu_2S assembly formation. (**G**) CD spectra of chiral assemblies of TGA only (black), L-Cys (red) and D-Cys (blue) capped Cu_2S NPs (**H, I**) CD and UV-vis spectra of assemblies of L-Cys capped Cu_2S NPs at different time points.

4.3.2 Chiropitcal Properties

The chiral preference on micro geometry was also confirmed by CD measurement. Two distinct CD peaks (~ 210 nm and ~ 270 nm) were exhibited in a mirror-symmetry which meant

they have the different cumulative absorbance for left- and right- circularly polarized lights indicating the strong chiroptical activity of *L*-cysteine and *D*-cysteine stabilized Cu_2S self-organized structures. The peak at 210 nm is generated from ligand-to-metal transition, and another at 270 nm is from Cu_2S crystals. With high resolution transmission electron microscopy (TEM) images, we could observe that the nano-leaves were formed with small nanocrystals.

To check the intermediate self-assembly stages during the incubation, we measured CD spectra and TEM images at various aging time. (**Fig. 4.32 G-I)** At the early stage of the aging process (0h), a distinctive CD peak was exhibited around 210 nm which results from the chirality of copper clusters. (**Fig. 4.32C)** The absorbance bands were red-shifted over aging time indicating the assembled structures become larger (**Fig. 4.32I**). The size of clusters became larger from ~ 10 nm to ~50 nm after 2 hours of incubation, and then started to form interlinked chains after 5 hours of incubation (**Fig. 4.32D-E**). With further incubation, we could observe that the chains transformed into leaf-like structures. The weak negative CD peak was shown around 260 nm for the assembled structures aged for 10 h, and the CD peak was more distinctive at the sample aged for 20h (**Fig. 4.32H**). With this analysis, it is examined that the nano-leaves were form by self-assembly of small nanoparticles (NPs). Cu_2S NPs were found to spontaneously assemble into high aspect ratio nano/maicrostructures after partial removal of the stabilizer in a previously reported precipitation-redispersion process. (*171*)

4.3.3 Reversible Assemblies and Chirality Control

The nanoleaves formed by self-assembly of NPs, further assembled into chiral nanostructures. 3D electron tomography image (**Fig. 4.33A**) To confirm the role of chiral

molecules determining the handedness of the nanostructure, we used racemic mixture of cysteine (*DL*-cysteine) as stabilizer for the synthesis. After the reaction, we added either *D*-cysteine or *L*-cysteine before starting the incubation at room temperature. Initially, the sample prepared with racemic mixture did not show optical activity. With further addition of chiral molecules, the nanoleaves self-assembled into distinctive directions depends on the chirality of the added molecules (**S1** and **S2**, **Fig. 4.33D**) whereas the sample kept in DI water still did not show such chirality (**S3**, **Fig. 4.33D**) . This result confirms that the chirality of assembled structure was transferred from molecules. The angled conformation of nanoleaves dominates over the paralleled stacked one because conformations with angles reduce their electrostatic repulsion and, therefore, are more thermodynamically favorable.

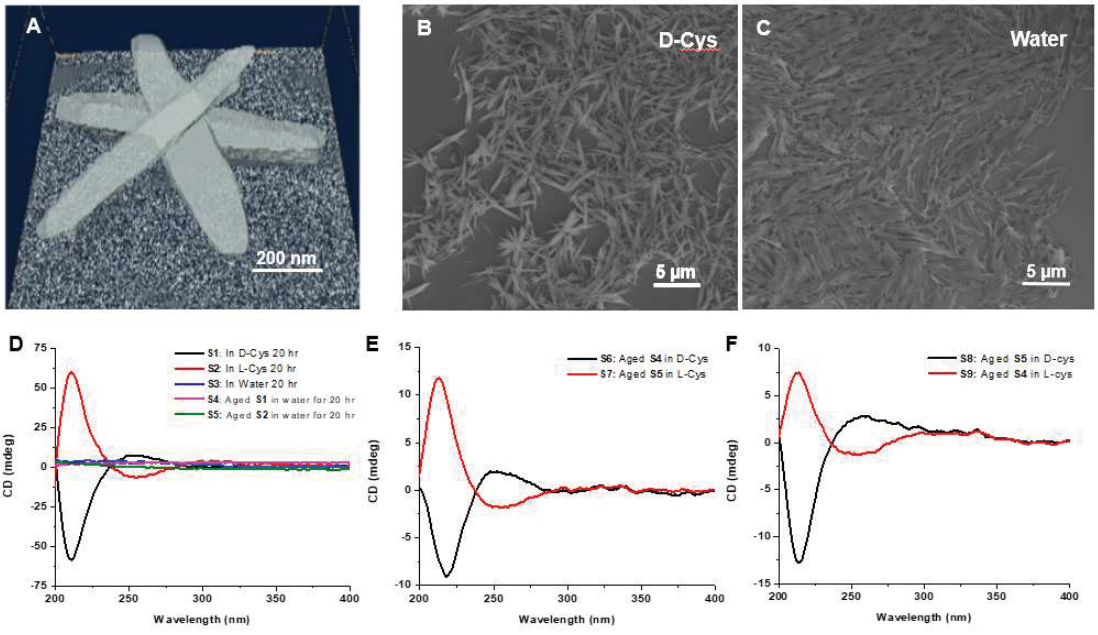

Figure 4.33 Reversible Assembly of Cu_2S NLs. (**A**) 3D electron tomography of NL assembly. (B) SEM image of NLs synthesized from racemic cysteine (B) after 20 hours incubation in D-Cys solution (C) and DI water (**D, E, F**) CD from NLs incubated in the different condition.

We further investigated on reversibility of this chiral conformations of leaves. After re-dispersing **S1** and **S2** in DI water and incubating for 20 hours, the leaves are disassembled into individual nanoleaves, losing chiroptical properties (**S4** and **S5 in Fig. 4.33D**, **Fig. 4.33C**). Upon addition of cysteine molecules into the dispersion, the chirality of these nanoleaves were restored (**Fig. 4.33E**). More interestingly, we could achieve opposite chirality against the first assembly conformation, (**Fig. 4.33F)** which demonstrate that assembly direction of NLs solely depends on active cysteine molecule on the NL surface, regardless of their original chirality conformation.

4.3.4 Summary and Future Work

As previously discussed in section 4.2.8, angled stack of Au NRs theoretically is expected to exhibit strong chiroptical properties. Similar assembly conformation to balance repulsive and attractive forces were also observed for many biopolymers and their nanoscale assemblies. When we modify the synthetic method of continuous crystalline copper sulfide nanoleaves by adding D or L cysteine molecules, nanoleaves were further assembled into similar angled geometries. The strength and directionality of repulsive/attractive interactions in nanoleaves determine the overall geometry of assembled structures. More interestingly, we experimentally showed the reversibility of chiral assemblies of nanoleaves. The result – the fine balance of repulsive-attractive interaction – leads to thermodynamic preference of a specific enetiomer, which we believe originate from intrinsic chirality of organic coating of nanoleaves.

4.3.5 Methods

4.3.5.1 Synthesis of of chiral β-Cu 2 S NPs

25 mL of deionized (DI) water in three-neck round bottom flask (250 mL) was heated to 85 °F and bubbled with nitrogen gas (N_2 gas) for 30 minutes. Thioglycolic acid (TGA) solution (33.3 μL of 70% (w/w) in H_2O) and L-, D-, or racemic (DL-) cysteine solution (2 mL of 0.275 M) were injected into the solution with vigorous stirring and purged with N_2 gas for another 30 minutes. After adding 0.02475 g of copper (I) chloride powder, the solution was purged with N_2 gas for one hour at 85 °C. Sodium hydroxide solution (0.5 M) was added to adjust PH of the solution to 9.0. After 5 min, 1 mL of thioacetamide solution (0.125 M) was injected and reaction was kept for 4 hours at 85 °C with N_2 gas purging. The sample was cooled down with ice water.

4.3.5.2 Assembly of chiral β-Cu 2 S NPs into chiral NL assemblies

The synthesized L-Cys or D-Cys Cu_2S NPs were mixed with isopropanol with 2:1 volume ratio and centrifuged at 8500 rpm for 20 min. The precipitated sample was redispersed in DI water and kept in dark at room temperature for 20 hours. The assembled structures were centrifuged at 6000 rpm for 5 mins and redispersed in DI water for CD measurement.

4.3.5.3 Assembly of achiral β-Cu 2 S NPs into chiral NL assemblies

The precipitation-redispersion process described in section 4.2 was performed for the racemic (DL)-Cys Cu_2S NPs. Collected DL-Cys Cu_2S NPs after partial removal of stabilizer process are redispersed in D- or L-Cys solution (**S1** and **S2**, respectively in **Fig. 4.33D**) and kept

in dark at room temperature for 20 hours. The assembled structures were centrifuged at 6000 rpm for 5 mins and redispersed in DI water for CD measurement.

4.3.5.4 Reversible assembly of NLs

The chiral assemblies of NLs in presence of D- and L-Cys (**S1** and **S2**, respectively) were redispersed in DI water and kept at room temperature for 20 hours to be disassembled. Disassembled individual NLs (**S4** and **S5**) are collected and incubated in cysteine solutions for another 20 hours to restore the chiral assembly structure of NLs.

4.3.5.5 3D TEM tomography

The electron tomography studies at room temperature were carried out on a JEOL2100 electron microscope operating at 300 kV (Michigan Center for Materials Characterization at University of Michigan). A series of 2D projection images were recorded by tilting the specimen from -60º to 60º in increments of 1.5 º. A tomography reconstruction software package Amira avizo 3 D software was used to align the tilt series and calculate three-dimensional tomograms using a weighted back projection algorithm.

4.4 The Switchable Chirality of Gold Composite Structure by Electric Field Modulation

Contributions: Kotov, N.A. supervised the project. Kim, J.-Y. designed the study, prepared the samples to be characterized, performed the experiments, and ran electron tomography. Emre, S., and J.-Y. Kim performed SEM and STEM imaging of modified sample with focused ion beam. Jang, H. helped experiments with vias voltage. Kim, J. -Y, wrote the manuscript.

As the computational studies showed in section 4.2, Au helices have significant differences in CD and *g* factor spectra compared to the semiconductor helices (**Fig. 4.20**), it is not suprising

that gold gives strong chiroptical responses due to the oscillatory nature of plasmon resonances. However, spontaneous self-assembly of Au NPs through the precipitation redispersion process suggested in our previous study is limited due to lack of interparticle attractive forces; This is different from the CdTe and Cu_2S NP having intrinsic dipole moments, dipole-dipole interaction cannot contribute to the interaction potential (E-DLVO) between Au NPs.

Instead relying on the interparticle forces of colloids, we have attempted to embed the AuNPs in an organic matrix, a hydrogel, which helps to assemble the NPs into supra structures but still gives the NPs a flexibility of re-arrangement for chiral conformation. In this study, we have successfully developed hollow chiral AuNP-hydrogel composite particles exhibiting not only distinctive circular dichroism (CD) but also circular polarized luminance (CPL). More interestingly, the chiroptical properties of the structures were changeable with electric field modulation.

4.4.1 Synthesis of chiral gold nanoparticle (Au NP) – hydrogel composite shell

Tetrakis(hydroxymethyl) phosphonium chloride (THPC) has been introduced as an inexpensive, amine-reactive, aqueous cross-linker for 3D cell encapsulation in protein-based hydrogels (**Fig. 4.34**) . (*172*) Since we have learned from our previous studies that cysteine capped NPs are actively assembled into chiral mesostructures, we have determined to synthesize a AuNP hydrogel composite using THPC.

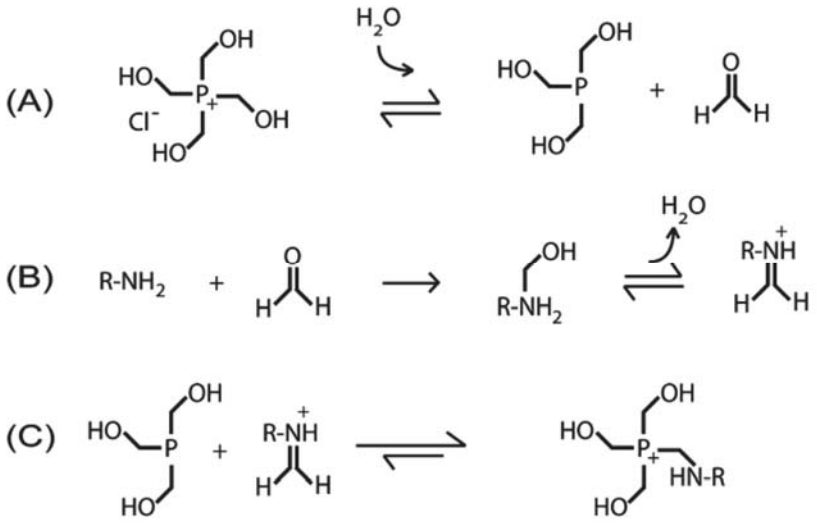

Figure 4.34 Scheme for formation mechanism of hydrogel. (**A**) Formation of formaldehyde to initiate hydroxymethyl arm replacement. (**B**) amine-formaldehyde reaction to yield an immonium ion in a Mannich-type reaction, and (**C**) phosphorus reaction with the immonium ion to complete the aine coupling. From Ref (*172*). Copyright 2012 American Chemical Society

Firstly, we have synthesized THPC-capped small Au NPs (~ 2 nm) with a modification of a previously reported method, adding double, the volume of isopropanol into the Au colloidal solution sample and centrifuged with 8500 rpm for 20 mins. The collected Au NPs were redispersed in L- and D-Cys solutions and kept in dark for 48 hours. The sample then centrifuged at 6500 rpm for 10 minutes in order to rediperse in DI water for further characterization. Interesting uniform microscale particles (diameter: 1-3 μm) consist of nanosheets are observed after the assembly process. (**Fig. 4.35 A-D**) More remarkably, these composite particles have 1-2 μm empty core, which has been revealed by partial cutting with a focused ion beam. (**Fig. 4.35 E,F**)

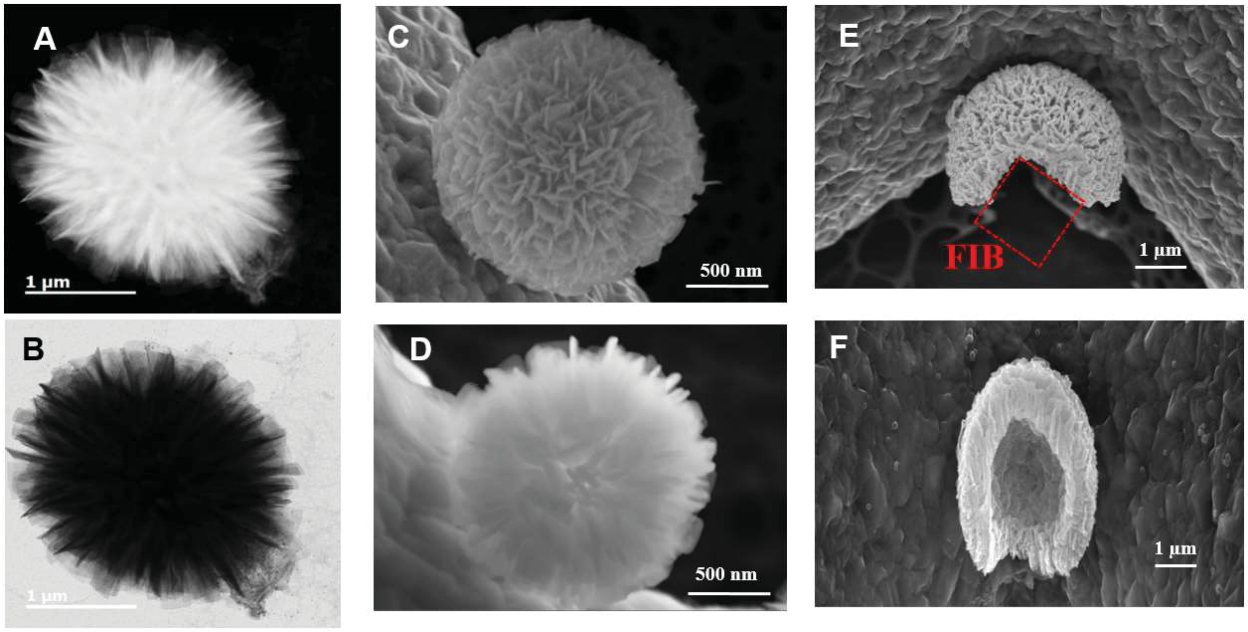

Figure 4.35 Structure of the AuNP –hydrogel composite shell. (**A**, **B**) Dark field and bright field images of the AuNP-hydrogel composite shell in STEM. (**C**) SE mode and (**D**) HADDF mode images obtained from SEM. (**E**, **F**) SEM images in different view after cutting a part by focused ion beam (FIB) to show empty core of structure.

UV-vis spectra (**Fig. 4.36 A**) of the particles showed absorbance of small cysteine capped Au NP , which shows that Au NPs in the microstructures are active individually as is but not physically fused or optically coupled together(*173*). The chiroptical response from these microstructures was also investigated by CD and CPL measurement. The distinct CD and CPL peaks were observed in a mirror-symmetry with a great g-factor, which meant Au NPs have been differently self-assembled or arranged by the strong chiral activity of *L*-cysteine and *D*-cysteine. (**Fig. 4.36 B,C**) We believe that the strong peaks around 375 nm found in CD was generated from surface plasmon resonance of cysteine capped Au NPs while strong CPL at 510 nm was generated without quenching due to isolation of the individual NPs in the composite system.

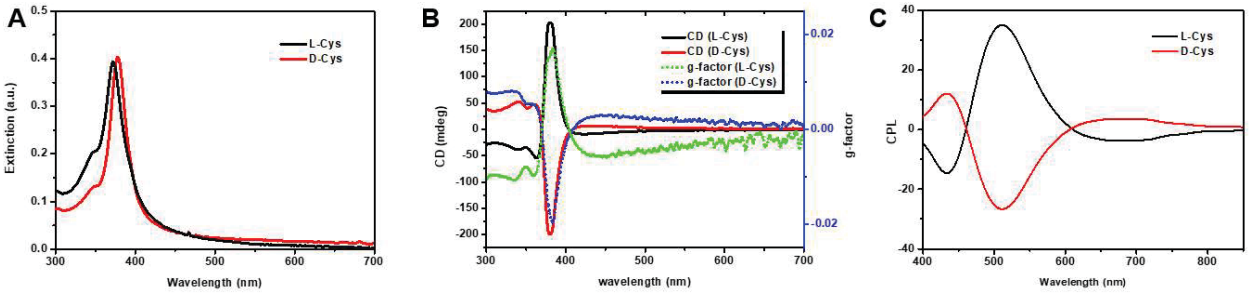

Figure 4.36 Chiroptical properties of the AuNP –hydrogel composite shell. (**A**) UV-vis spectra of the assembled structures with D- and L- cysteine. (**B**) CD and g-factor of the structure. (**C**) Circularly polarized luminescence (CPL) from the assembled structures.

4.4.2 Formation Mechanism

To gain insight into the formation mechanism of this interesting structure, we have taken STEM and SEM images of the structure at different time points (**Fig. 4.37**). At the beginning of the assembly process, Au NPs aggregates were formed within 1-2 μ m hydrogel with no specific arrangement of NPs were observed (**Fig. 4.37A**). At 5 hours, small Au NPs in the microhydrogel seem to be arranged into thin nanowire like structures while some excess Au NP attachment emerges on outer surface of the microparticles (**Fig. 4.37C**). From this point on, the hydrogel becomes porous and enlarged and the spiky outer shell with Au NPs is observed on the surface of the gel (**Fig. 4.37H**). At the final stage, nanosheets are formed bridging the nanowires and core is completely empty. (**Fig. 4.37I**) These STEM and SEM studies demonstrated that almost immediate hydrogel formation and fast re-arrangement of Au NP occurs, followed by a relatively slow growth of nanosheet shell as they are fully formed with hollow core.

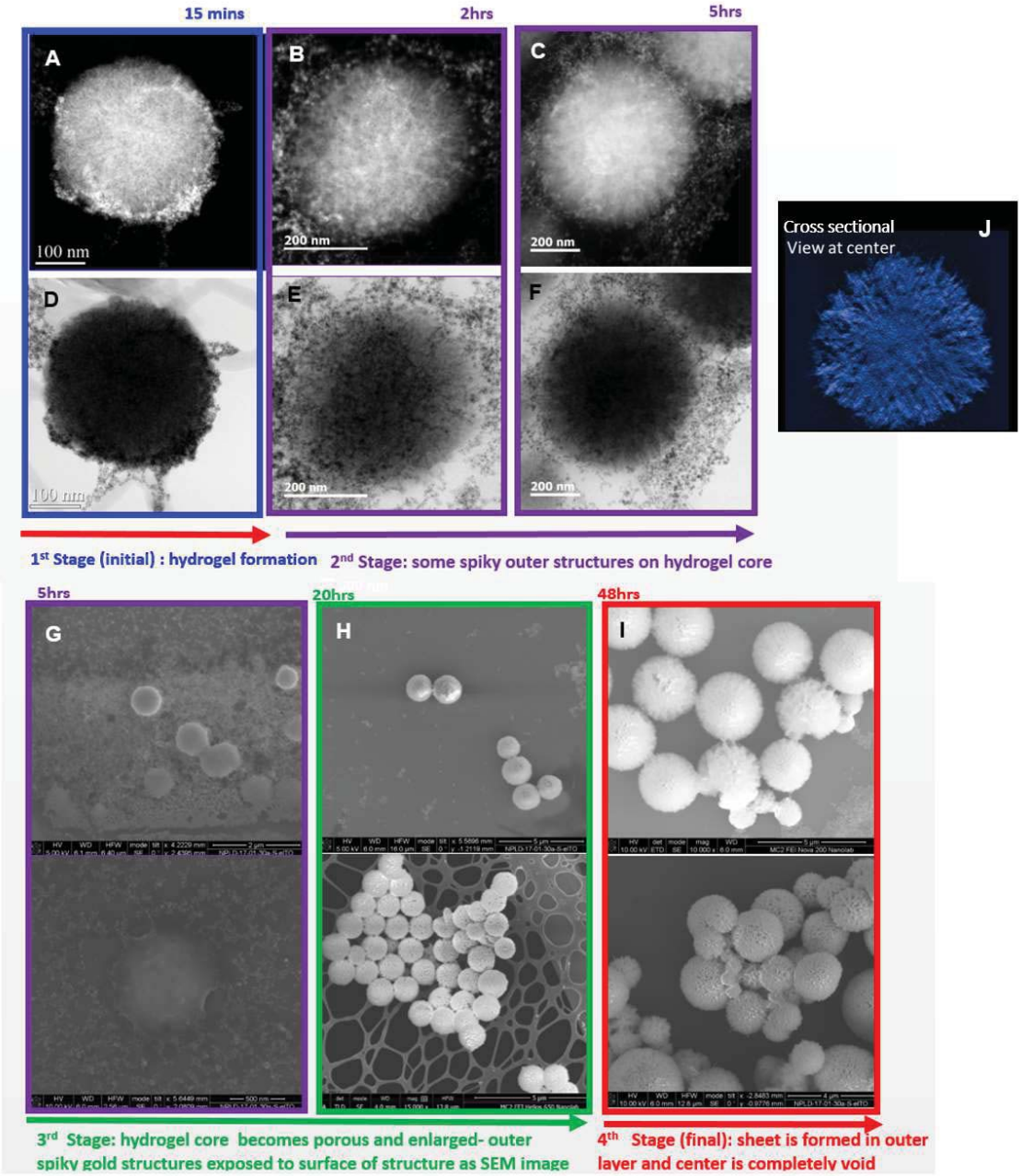

Figure 4.37 Electron microscopic images for the different stages of growth. (**A, B, C**) dark filed and (**D, E, F**) bright field STEM images of AuNP and hydrogel composite micro-particles in early growth stage (**G-I**) SEM images showing the later stage of growth forming the hollow chiral shell. (**J**) 3D electron tomography image of the Au composite particle at 5 hours (cross-sectioned at center)

4.4.3 Chiroptical Responses

The massive change in chiroptical response was observed during the growth of particles, which may represent structural chirality change. Notably, between 20 and 48 hours growth time points, we have observed in CD a dominant peak change. A peak at ~ 365 nm (blue, **Fig. 4.38A**) dominating early growth stage is depressed, and the peak with opposite sign at ~ 380 nm (pink, **Fig. 4.38A**) is significantly enhanced. A similar tendency was observed in CPL responses. These optical changes suggest that hierarchical structures of the particle possibly have opposite chiralities. Further investigation in the relationship between the structural growth and chirality is needed. In addition to the change in dominating peaks, blue-shifts of the peaks are observed, which may indicate that the structure consists of smaller Au NPs. There are multiple reports that showed the ability of thiolated molecule to etch metal NP into nanoclusters.(*93*) We believe that Au NPs digested by excess cysteine are consumed to build up the nanosheets at final stage.

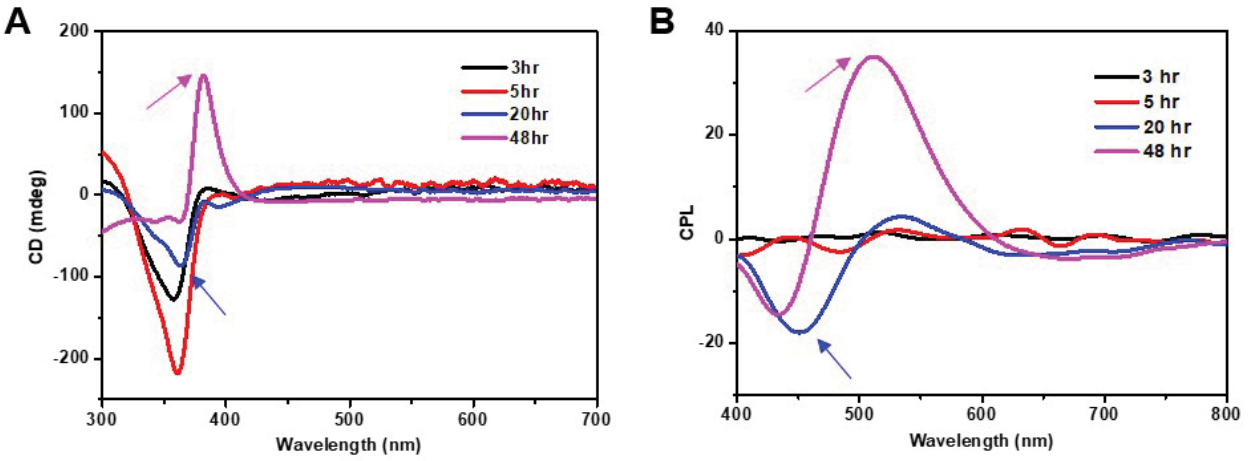

Figure 4.38 Chiroptical reponse at different growth stage. (**A**) CD and (**B**) CPL spectra of the self-assembled Au NP-hydrogel particle at different time points. (3, 5, 20, and 48 hours)

4.4.4 Switchable Chiroptical Properties by Electric Field Modulation

Control of chiropitcal properties with external stimuli is desirable for practical application of the chiroptical materials. We hypothesize that a bias voltage on the sample can change its chiroptical response since the charge density of the structure may play an important role for their plasmonic chiroptical properties. After modifying ITO glass with (3-aminopropyl) triethoxysilane (APTES), the substrate is immersed into the growth solution of the Au NP-hydrogel shell. The half chiral shells are formed on the substrate in large scale. (**Fig. 4.39**). When the positive bias voltage is applied to the substrate, the intensity of CD peaks are decreased whereas negative bias can restore their chiroptical response. (**Fig. 4.40**) Systemic study to clarify the origin of this switchable chiroptical properties is needed for further discussions.

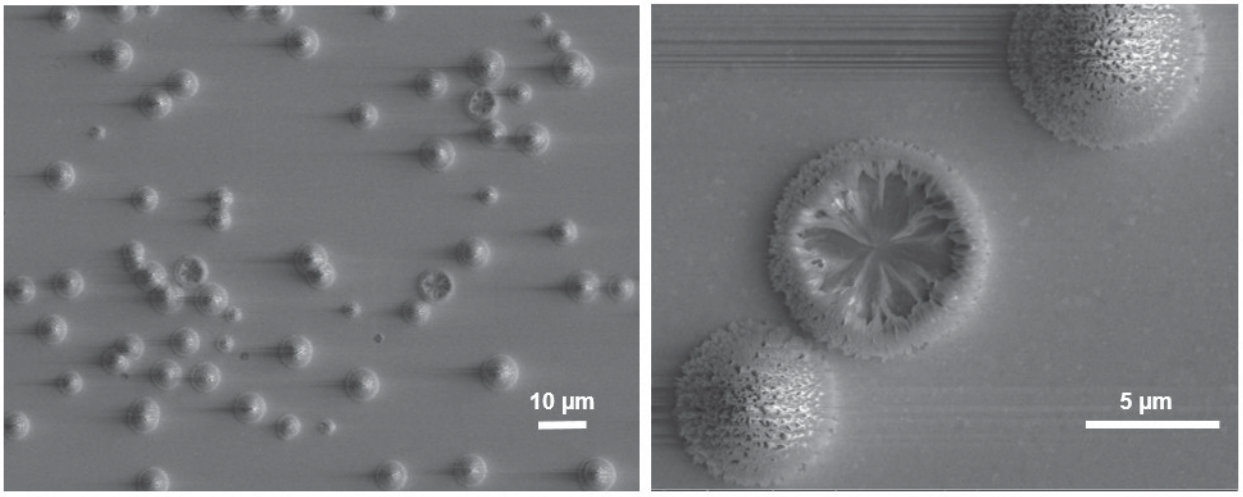

Figure 4.39 SEM image of gold chiral composite shell on ITO substrate with different magnification.

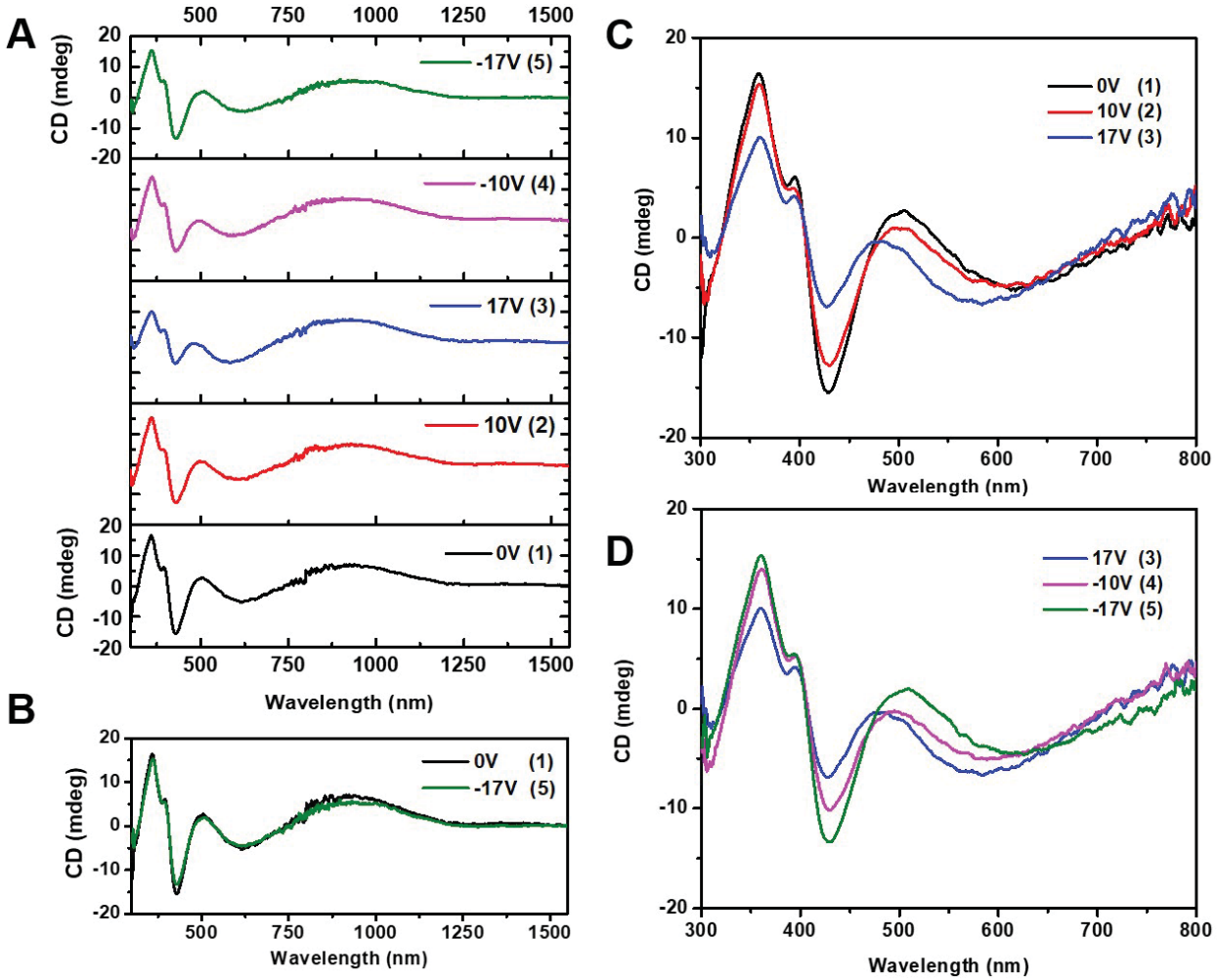

Figure 4.40 Control of Circular Dichroism with Bias Voltage. (**A**) Time series of CD signals with subsequent bias voltage (from sample 1 to 5). (**B**) First and final CD (sample **1** and **5** in **A**) (**C**) Decrease and (**D**) increase in intensity of CD peaks upon applying positive and negative bias voltage, respectively.

4.5 Conclusion and Future work

This work provides an understanding of structure-property relationships for chiral nanomaterials and offers a precise set of guidelines for optical activity modulation based on collective self-organization of chiral nanoscale building blocks. Chiral self-sorting represents an important characteristic for this self-assembly system, ensuring the conservation and amplification of chirality in the eventual superstructures. The chiral interaction and its energetics were investigated by ITC, which indicates stronger interaction between NPs of the same handedness and correlates well with the observed self-sorting phenomena. Since inorganic NPs were likely to be present in the environment of primordial Earth (*174*), the finding that simple chiral ligands control the assembly of semiconductor NPs into homochiral structres could play a key role in explaining the origin of homochirality on Earth. In addition, future chiral nanostructures with tunable, geometry-dependent chiroptical activity and broad-band Vis-NIR characteristics can potentially be integrated into biomedical applications (*139*), telecommunications (*140*), hyperspectral sensors (*141*), and short-wave infrared imaging (*142*).

Chapter 5 Light-Driven Synthesis of Chiral Gold Nanoparticles and Quantification of Chirality

Contributions: Kotov, N.A. supervised the project. Yeom, J. synthesized gold nanoparticles with circularly polarized light. Under the guidance of Zhang, P., Zhao, G. took electron tomography. Kim, J.-Y performed fine element method computation to evaluate circular dichroism of 3D tomography model with Comsol Multiphysics. Kim, J. -Y. extracted point groups for chirality measure and computed Osipov-Pickup-Dunmer chirality indices and Hausdorff Chirality Measure. Calcaterra H. calculate continuous chirality measure. Kim, J. -Y, Yeom, J. and Kotov, N. A. wrote the manuscript.

5.1 Introduction and Background

A number of chemical synthesis techniques are known to produce metal anisotropic nanoparticles with a variety of shapes and sizes. The commonly used synthesis method is a two-step seed-mediated process as introduced in Chapter 2 for the synthesis of Au NRs. First, small gold seed nanoparticles are formed through the chemical reduction of metal ions in the presence of stabilizing agents. Subsequently, these seed are grown into NR shape by a further reduction (growth) process. Photochemical synthesis routes suggest an exciting alternative to these classical synthesis methods, finding merit in the synthesis of metal anisotropic nanoparticles, yielding a variety of distinct shapes such as nanoprisms, nanobipyramids, nanodisks, nanorods, nanorings, and nanohexagons (*175–179*). Despite the need for more study in how electromagnetic radiation throughout the visible region guides the growth process of particles, the decay of a plasmonic excitation is believed to result in the formation of a hot electron–hole

pair, which transfers the excess electron to a surface-adsorbed reducing agent and results in nanoparticle growth.

Synthesis of metallic nanoparticles (NPs) with chiral structures is one of the most intriguing study in field of nanotechnology, due to its surprisingly strong optical activities in the metal-based electronic transitions in the visible region as we also discussed in Chapter 4. The strong dichroic response of plasmonic nanoparticles (NPs) and their assemblies has resulted in a rapid increase of the number of studies on chiral inorganic nanoscale structures over the last decade (*23*, *37*, *130*, *156*, *180*, *181*). While significant progress has been made towards developing synthetic methods of chiral inorganic nanostructures, understanding the relationship between the chiral optical activity and geometrical parameters of plasmonic nanostructures remains to be clarified. Particularly, while the molecular and atomic scale chirality measure of biomolecules has been extensively studied based on their atomic arrangement and is generally well understood (*182*), chirality measure of inorganic nanoparticles in particle-level has been hampered due to complex and bulky structure.

Here, we demonstrate that illumination of Au precursors in the presence of citric acid with right- (left-) handed circularly polarized light (CPL) induces the formation of gold (Au) NPs having distinctive chiropitcal activities. Despite seemingly achiral irregular shapes of the particles, we have successfully demonstrated that their chiroptical responses are solely related to their geometries. Implementing three-dimensional electron tomography into computational model allowed us to develop a new method for chirality measure. The ability of Au NPs to retain

the polarization information of incident photons open a door for further thoughts about light – matter interaction to create new chiral nanomaterials.

5.2 Motivation and Hypothesis

Recently, our group suggested circularly polarized light (CPL) as a new tool to transfer spin angular momenta of photon to matter, retaining the chiral information as a permanent structure.(*183*) CPL 'templating' of cadmium telluride (CdTe) NP assemblies is based on the enantio-selective photoactivation of chiral NPs and clusters, followed by their photooxidation and self-assembly into nanoribbons with specific helicity as a result of chirality-sensitive interactions between the NPs CPL. Here, in this manner, we hypothesize that CPL illumination can also cause a photo induced reaction of the metal nanoparticle precursor and chirality to form a stable chiral plasmonic nanoparticles. Such mechanisms can be slightly different than the assembly mechanism proposed previous study or the growth mechanism proposed for the silver nanoprisms but begin in the reduced state and are exclusively transformed into chiral structure through the light-induced ripening or assembly process.

5.3 Synthesis of Chiral Gold Nanostructures by Circularly Polarized Light

As Au precursors and achiral capping agent, we used HAuCl4 and citrate. In a quartz cuvette, 2 mL aqueous solution of HAuCl4 and citrate was placed and illuminated by left- (LCP) or right-handed circularly polarized light (RCP) with a wavelength of 543 nm. After 50 min illumination, the pale yellow color of solution turned into red which indicates formation of plasmonic Au NPs. The optical activities of obtained solutions were examined by circular

dichroism spectroscopy (CD) that measures absorption differences between LCP and RCP ($\Delta\varepsilon\ (\mathrm{CD}) = \varepsilon_{LCP} - \varepsilon_{RCP}$). Depends on the handedness of the incident CPL, samples showed mirror-imaged opposite CD bands (**Fig. 5.1A**) at the plasmonic resonance region that in good agreement with UV-Vis absorbance spectra (**Fig. 5.1B**). We observed the morphology of obtained NPs using transmission electron microscopy (TEM) (**Fig. 5.1C** and **D**). The shape of NPs was not a typical sphere but v-like twisted structures that were about 10 nm a cross. To our knowledge, this is the first reported example of using circularly polarized light and metal ion solution to synthesize chiral metal NPs.

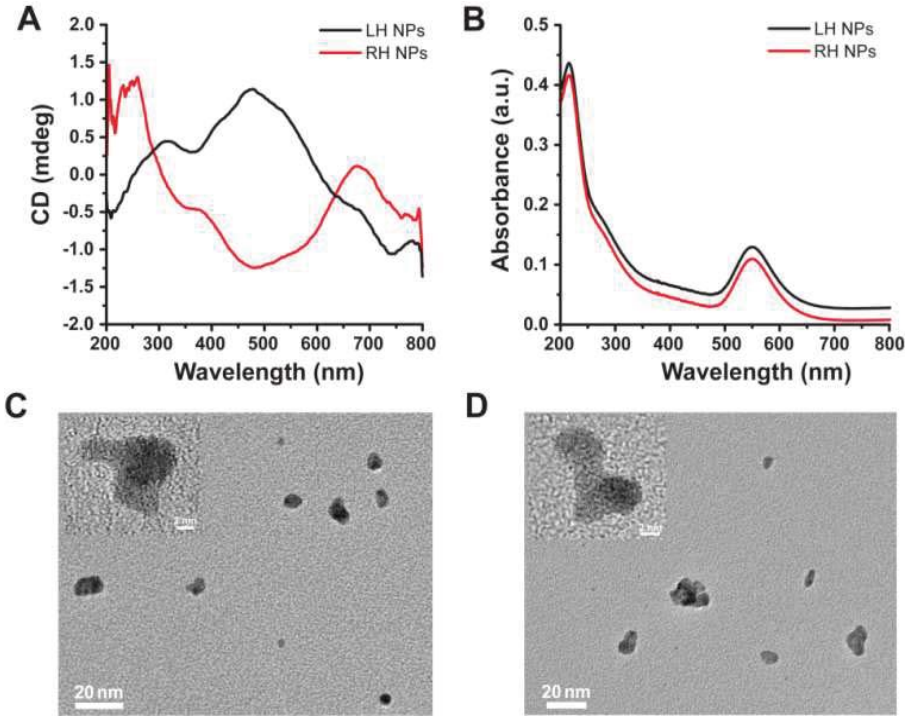

Figure 5.1 Optical properties and shape of gold (Au) NP after 50 min CPL illumination. Circular Dichroism (**A**) and UV-Vis absorbance (**B**) spectra of LH (black) and RH (red) chiral Au NPs. (**C, D**) HR-TEM images of Au NPs obtained after 50 min illumination of LCP (**C**) and RCP (**D**).

5.4 Formation Mechanism

The CPL photolysis of HAuCl4 in water can be described as a sequence of reactions resulting in reduction of Au III to Au 0 and Au colloid formation. Excitation of $HAu^{3+}Cl_4$ solutions by energetic photons resulted in irreversible reduction of Au complexes. Kurihara et al.,(*184*) demonstrated using transient absorption spectra that the Au^{3+} reduction to Au^0 is a multiphoton event. The formations of caged divalent gold complex occurs following excitation. (**Eq. 5.1, 1-2)** The complex then dissociates and disproportionate (**Eq. 5.1, 2-4**). The long term buildup of stable absorbance is due, of course, to colloidal gold formation (**Eq. 5.1, 6**), subsequent to the reduction of the gold monocation (**Eq. 5.1, 5**).

$$(HAu^{3+}Cl_4) \xrightarrow{h\nu} (HAu^{3+}Cl_4)^* \quad (1)$$

$$(HAu^{3+}Cl_4)^* \rightarrow (HAu^{2+}Cl_3 \dots Cl) \quad (2)$$

$$(HAu^{3+}Cl_4)^* \rightarrow (HAu^{2+}Cl_3 \dots Cl) \quad (3)$$

$$(HAu^{2+}Cl_3 \dots Cl) \rightarrow HAu^{2+}Cl_3 + Cl \quad (4)$$

$$HAu^{+}Cl_2 \xrightarrow{h\nu} Au^0 + HCl + Cl \quad (5)$$

$$nAu^0 \rightarrow (Au^0)_n \quad (6)$$

(Eq. 5.1) Suggested colloidal gold formation mechanism by photon absorbance, subsequent to the reduction of the gold monocation. From ref. (*184*)

Our experimental results suggest that circularly polarized momenta of photons can be transferred to the nano-geometry during the sequential light-induced reduction procedures. The photon energy effects were examined by checking the intermediate stages of the chiral growth of Au NPs. At various illumination times, we recorded TEM images and CD spectra (**Fig. 5.2**) After 5 min of illumination, spherical ~ 2 nm NPs were observed, and with continuous illumination, the NPs were self-assembled into anisotropical structures. With the shape transformation and the size incensement to about 10 nm, CD and UV-vis absorbance bands arose accordingly at around 550 nm (**Fig. 5.2B** and **C**).

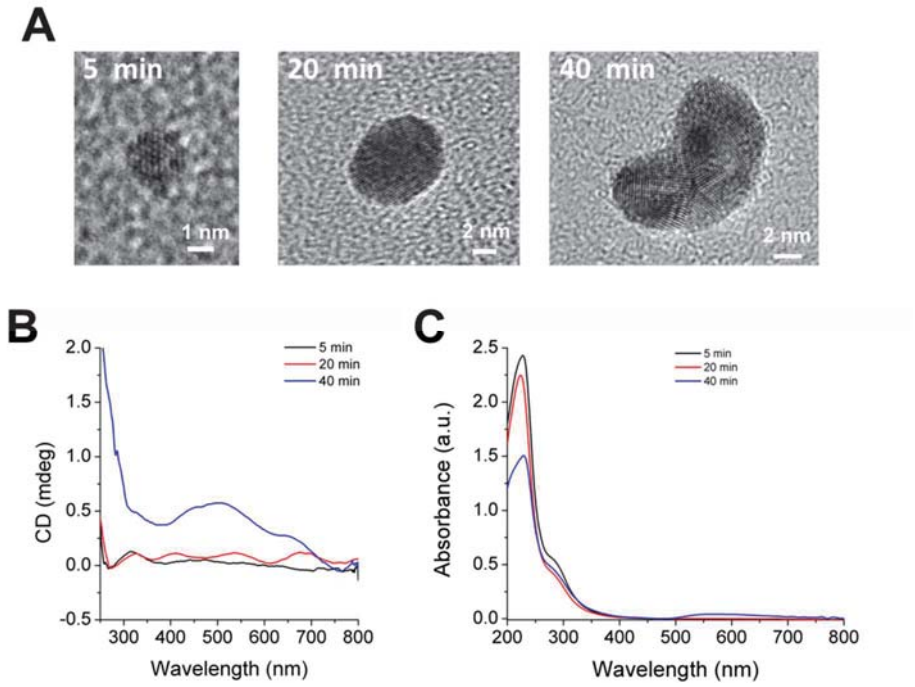

Figure 5.2 TEM images (**A**), CD (**B**) and absorbance (**C**) spectra of chiral Au NPs at various illumination time points.

The light-driven shape transformation of plasmonic NPs has been well-studied. According to the previously reported papers, originally spherical citrated capped Ag NPs changed their shapes into prism-like shape with white unpolarized light illumination. (*177*, *178*) In the study, it has been understood that the overall kinetics, and final shapes of the transformation were decided by the nature of citrates. Upon prolonged light exposure, citrate on the NPs surface undergoes continuous photo-oxidation with a sacrificial electron donation process that contributes to metal ion reduction. The transformation procedure have identified three distinctive stages: induction, growth, and termination. In the induction period, extremely small spherical silver clusters (2 to 4 nm) and the small nanoprisms (5- to 10-nm edge lengths)

were formed concurrently. The silver nanoprisms then act as seeds and grow as the small spherical crystals are digested. Once the spherical particles and small nanoclusters are consumed, the reaction terminates. The photoinduced conversion of silver particles or silver salt into small clusters makes the use of light an efficient way to control the growth of the silver nanoprisms. Those silver clusters may have formed from either fragmentation or dissolution of the larger particles. Photoinduced fragmentation of silver nanoparticles (visible laser at 532nm) has been observed by Hartlandandco-workers (29), albeit with a much higher intensity source. Other researchers have used visible lasers, UV, or γ irradiation to prepare spherical silver nanocrystals from silver salts in the presence of organic reducing agents (30, 31), and, typically, photoinduced reduction mechanisms are invoked to describe such processes.

Based on these previous observation of shape transformation process, we can suggest the following growth mechanism for our chiral Au NPs. With CPL illumination, (1) Au precursors reduced to Au seed colloids, and while the citrate provides hot electrons on the surfaces, (2) Au colloids assembles into anisotropic shapes accordingly depend on the handedness of the light. To confirm the circular momentum effect on the gold ion reduction reaction, use used linearly polarized light (LPL) as the illuminating source (**Fig. 5.3**). After 50 min of illumination, the pale-yellow solution again turned into a red color, but the solution did not show CD signals where it had an absorbance band (**Fig. 5.3A** and **B**). We observed that the geometry Au NPs was elongated in 2-dimension (**Fig. 5.2C**). This result also confirms transformation of polarization information of photon to nano-geometry.

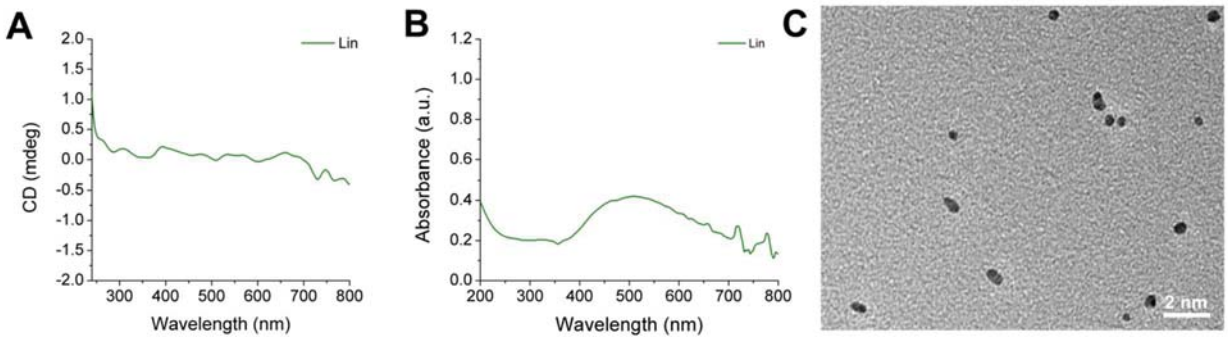

Figure 5.3 CD (**A**), absorbance (**B**) graphs and TEM images (**C**) of Au NPs illuminated by linearly polarized light for 50 min.

5.5 Circular Dichroism (CD) and Their Geometry

Since TEM only measures 2-dimensionally projected images, we carried out 3D TEM tomography imaging of NPs that were obtained by CPL illumination to visualize their chiral structures. The reconstructed images revealed complicated structures that do not show obvious representative handedness (**Fig. 5.4A** and **B**). To confirm the optical activities of each individual NP, we computationally calculated their CD signals using experimentally obtained 3D structures as simulation models. So far, simplified representative models have been used to calculate optical activities of nano-systems to simplify simulations. This is the first approach that imported experimentally obtained 3D information into the calculations. Despite the complicated structures, the individual NPs showed mirror-imaged spectra (**Fig. 5.4C**). Considering that the experimental spectra represent NPs dispersions containing a range of various shapes and sizes, calculated spectra of two individual NPs is generally agrees well with the experimental results.

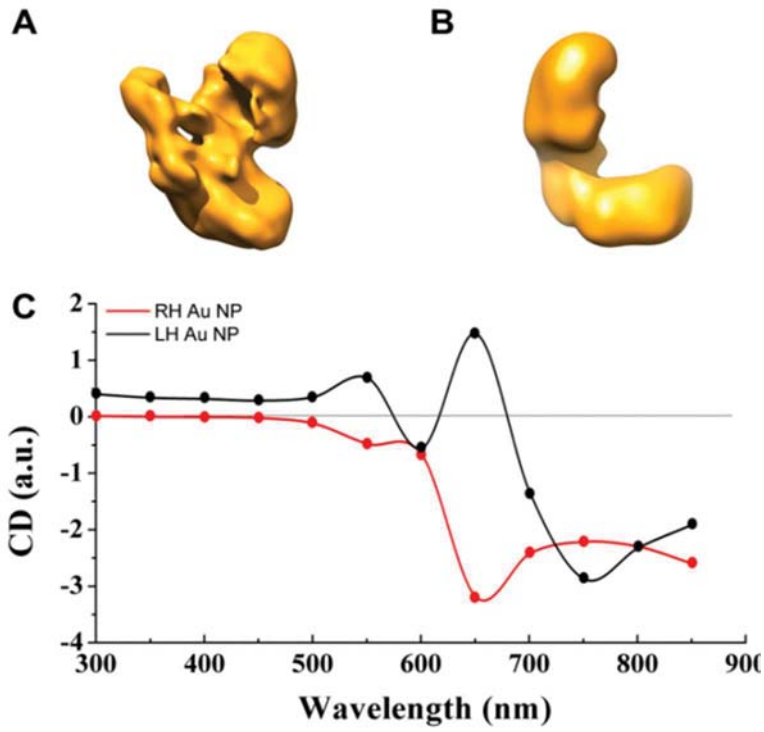

Figure 5.4 TEM electron tomography of chiral Au NRs and their theoretical CD spectra. (**A, B**) Experimentally obtained TEM tomography reconstructed images of LH (A) and RH (B) gold NPs. (**C**) Calculated CD spectra with models importing from electron tomography.

5.6 Quantifying Chirality

To further elucidate chirality of these particles, we de-termined to quantify the chirality of these nanostructures. Quantifying chirality in atomic-scale dynamics of matter has been studied intensively with various methods based on the sets of atomic coordinates and bonding. Rassat et al. (*185*) introduced the evaluation of the smallest Haussdorf dis-tance between chiral objects as a chirality measure and his approach was applied by Buda et al. for the tetrahedron and examined indices of chirality based on their geometric pa-rameters. (*182*) By rotating and

translating one enantiomorph with respect to the other, one can find the minimal value of Hausdorff's distances corresponding to the optimal over-lap(s). Zabrodsky et al. defined the continuous chirality measure (CCM) given a configuration of points(*186*), its chirality content is determined by finding the nearest configuration of points which has an improper element of symmetry and by calculating the distance between the two sets. A consistent chirality index must not only be identically zero for achiral objects and nonzero for chiral objects, but also change sign under space inver-sion, allowing for the determination of an absolute configu-ration. Either of two approaches mentioned above cannot provide proper sign for the chiral structures. Osipov et al. suggested a new method to quantify a molecular chirality with signs using intrinsic molecular chirality tensor based on only on nuclear positions.(*187*) The tensor gives rise to two universal chirality indices; the first giving information about absolute chirality, and the second about the anisotropy chirality, i.e., the degree of chirality in different spatial directions.

Although chirality of various nano/atomic-scale materials including ligand-protected metal clusters has been quantified, chirality solely from geometry metal NP core has not been studied well since atomic information of the metal core without chiral ligand shows achiral property in principle. Importing experimentally obtained geometry of our chiral Au NPs into the computation model allowed us to develop a new chirality quantification method for spatial information from whole structure of inorganic NPs, demonstrating spatial chirality of these seemingly irregular shape of particles.

5.6.1 Mass points from 3D Tomography of NP

Various chirality quantification methods are developed by considering the chirality of an arbitrary geometrical object or an idealized molecule which can be represented as a set of rigid 'atoms'. A chiral object or molecule may be repre-sented uniquely by a generalized density p(r) which, for a molecule consisting of point atoms, could be a sum of delta functions. Instead using coordinates having actual mass point of nuclei or atom, we extracted a coordinate of mass centers from partitions of the entire geometry to simplify spatial information of mass of entire geometry. The import-ed 3D e-tomo model was placed in Cartesian coordinate system having origin at the center of total mass. The surface point with longest distance from the center is aligned with z axis, subsequent alignment of the particle with x axis having largest intercept. (b in Figure **5.5A**) With the 8 otants of the coordinates system, the particles were sectioned into pieces (**Fig. 5.5B**) and coordinates from their center of partial masses have been collected. (**Fig. 5.5C**, **Table 5.1**)

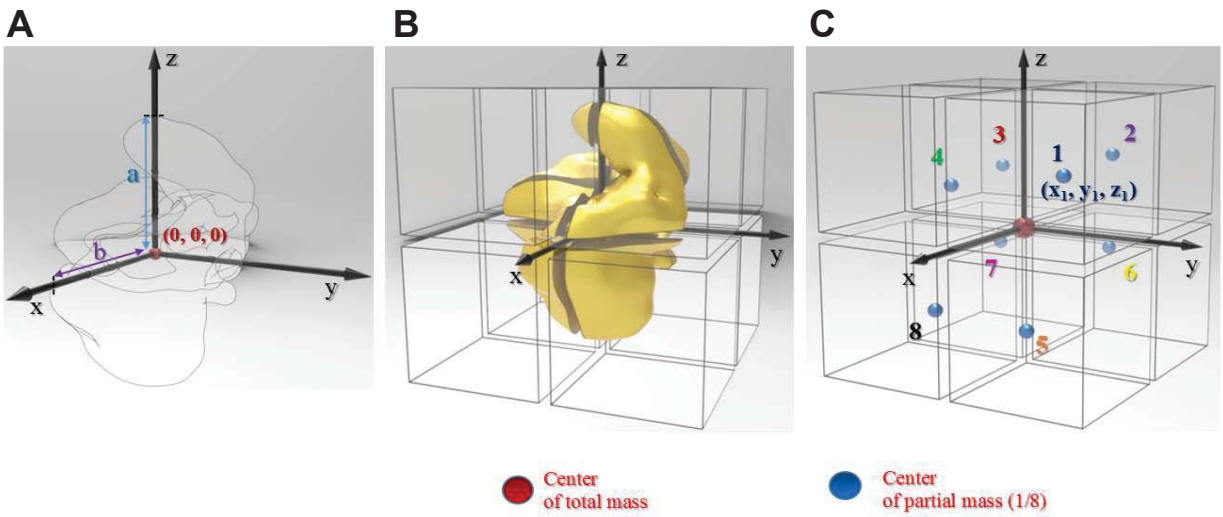

Figure 5.5 Schematic description of calculation model for chirality quantifications with LH tomographic data. (**A**) Placement of the particle in Cartesian coordinate system having origin at the center of total mass. (**B**) Sectioning particles with the 8 octants of coordinate system (**C**) Generating center of mass from 8 different partitions.

	RH				LH		
	x	Y	z		x	y	z
Center of total mass	0	0	0	Center of total mass	0	0	0
X>0, Y>0, Z>0 partition	12.071	3.9194	12.65	X>0, Y>0, Z>0 partition	19.081	27.564	26.915
X>0, Y>0, Z<0 partition	8.1812	8.1482	-11.178	X>0, Y>0, Z<0 partition	13.518	35.605	-11.34
X>0, Y<0, Z>0 partition	12.127	-7.8578	23	X>0, Y<0, Z>0 partition	25.579	-18.834	24.52
X>0, Y<0, Z<0 partition	7.2927	-5.932	23.486	X>0, Y<0, Z<0 partition	18.262	-29.319	-28.395
X<0, Y>0, Z>0 partition	-7.1751	5.4704	36.723	X<0, Y>0, Z>0 partition	-24.438	27.854	17.862
X<0, Y>0, Z<0 partition	-12.309	9.7693	-19.863	X<0, Y>0, Z<0 partition	-25.079	25.381	-11.681
X<0, Y<0, Z>0 partition	-4.1409	-5.5582	32.353	X<0, Y<0, Z>0 partition	-20.893	-14.169	16.526
X<0, Y<0, Z<0 partition	-11.312	-6.6891	-17.12	X<0, Y<0, Z<0 partition	-13.288	-32.022	-24.321

Table 5.1 Coordinates of point of mass extracted from model in Fig. 5.5 .

5.6.2 Quantifying chirality from the extracted point group

From the extracted coordinates of LH and RH AuNPs. (**Table 5.1**), we have calculated Osipov-Pickup-Dunmer chirality indices (G_0),(*187*) Hausdorff chirality measure (HCM), (*182*) and Continuous chirality measure (CCM)(*186*) (**Table 5.2**). Note that CCM calculation was performed for the model of which center of total mass (coordinate: (0,0,0)) connected to the

eight centers of partial mass respectively. RH NP consistently showed bigger quantitative value in three different chirality quantifying methods, which is well matched with CD computation result in section 5.5. More importantly, G_0 of LH and RH NP showed the signs as expected in experimental CD.

	RH Au NP	**LH Au NP**
Osipov-Pickup-Dunmur Chirality Index	-4.965	0.6493
Hausdorff Chirality Measure	0.1861	0.1343
Continious Chirality Measure	1.738	1.315

Table 5.2 Chirality quantification results for RH and LH Au NPs.

5.7 Conclusion and Outlook

Data obtained in this study indicates that CPL reduces light absorbing materials and directs assembly of NPs to have structural chirality. The produced Au NPs showed opposite chiroptical activities depending on the handedness of illuminated CPL. Their chiral structures and optical activities were confirmed by developing a new computational method implementing 3D e-tomo imaging into theoretical calculations. Technologies suggested in this study can be expanded to a large family of nanoscale materials. Similar consideration of chirality found in these seemingly irregular particles is applicable to other nanoscale structures; for which the property-governing symmetry of the geometry may differ from the apparent shape of particles observed in microscopic images.

5.8 Materials and Methods

5.8.1 Optical set-up for the CPL induced assembly

The green (543 nm) helium-neon laser with random polarization of emitted photons (Research Electro-Optics, Inc. Boulder, Colorado) was used as a light source. The laser emission was transformed to CPL by directing it through a linear polarizer and a quarter-wave plate. Since the quarter-wave plate is made with a birefringent material, the linearly polarized light turned to CPL by passing through the quarter-wave plate with the 45° transmission angle. By rotating the quarter-wave plate 90° relative to the previous angle, the handedness of the CPL is changed.

5.8.2 Synthesis of Chiral Au NPs

An aqueous solution was prepared by dissolving HAuCl4 and citrate 2.5 mM each in E-pure water. The solution was places in a dark room, and then exposed to CPL for 50 min. As NPs were formed, the pale-yellow color turned to a red color. The obtained NPs were washed to remove remained salts by gentle centrifugation (bench-top centrifuge, 3000 rpm, 3 min) and re-dispersion in E-pure water. The morphology was analyzed by using transmission electron microscopy (TEM, JEOL 3011, Michigan Center for Materials Characterization at University of Michigan), and CD spectra were obtained by a JASCO J-815 instrument.

5.8.3 3D TEM tomography

The electron tomography studies at room temperature were carried out on a Tecnai F20 electron microscope (FEI Corporation, Hillsboro, OR.) equipped a Gatan 4K ×4K CCD camera and a field emission gun (FEG) operating at 200 kV. A series of 2D projection images were

recorded by tilting the specimen from -75º to 60º for LH Au NP and -66º to 75º for RH NP in increments of 1.0 º. A tomography reconstruction software package IMOD (*188*), was used to align the tilt series and calculate three-dimensional tomograms using a weighted back projection algorithm. The surface rendering was generated using the UCSF Chimera software .

5.8.4 Computation of Circular Dichroism by Comsol Multiphysics

We compute the chiroptical property of Au nanoparticles by importing experimental 3D tomographic geometries into the wave-optics module of COMSOL Multiphysics 5.1. Since we directly imported the 3D images obtained by TEM tomography, the simulating model had the same dimension and shape of the selected real particles. The imported structures were assigned as a domain of which material is gold and the environment was set as water whose refractive index is 1.33. Optical constants of gold were adapted from ref (*189*)

Using the finite element method, we solved the frequency domain form of Maxwell's equations in the optics module. We obtained scattering and absorbance of the gold structures when they interact with left- and right-hand circularly polarized electromagnetic waves of which wavelength ranged from 300 nm to 850 nm with 50 nm interval. To remove directionality problem of the object in the model, we averaged CDs simulated for 144 different propagation directions defined by two spherical angles with a step of π/6. At the first, their shape looked irregular, however, the simulation results clearly show that these two geometries of each particle showed distinctive opposite chirality and even fit the tendency of experimental CD signals. Note that the RH CD signal is amplified five times compared to original to offer better comparison of data. Considering size and volume difference between RH and LH particle, this intensity

difference can be rationalized. In the same context, although positions and intensity of peaks are different in some degree from, given the singularity of the selected 3D imaged particle and breadth of the size distribution, computed CDs are accurately matched with experimental observations.

Chapter 6 Conclusion and Future Directions

The latest progress in solution processable devices, lead by developing methods to produce inorganic NPs and their assemblies, is remarkable. Although symmetry assignment of the nanostructure is tremendously important to understand its fundamental properties and design the assembly strategies using it as the nano-"building blocks", the symmetry of the inorganic nanoscale object, is rarely questioned and just generalized into a simple geometry model based on the inorganic core. These foundational assumptions, however, need to be reexamined according to our recent studies.

In chapter 2 and 3, we demonstrated that AuNRs are electrostatically non-centrosymmetric despite the appearance of the nearly perfect central symmetry in TEM images. Due to the uneven distribution of CTAB between the two ends, AuNRs are highly polarized, and act as non-centrosymmetric mateirals. With this finding, we have successfully obtained a complete self-consistent picture of both coherent and incoherent light scattering. The presence of surface charge asymmetry is expected to play a role in, and be further exploited in relation to optical properties (*81*, *82*), electrical properties (*11*, *83*), catalysis (*51*), and especially self-assembly behavior (*84*, *85*), including dissipative systems (*9*), and chiral nanostructures (*86*).

In Chapter 4, we have found that simple chiral ligands control the assembly of various NPs into homochiral structures, which had not been developed for engineered inorganic materials. While cysteine capped CdTe NP assembled into a helices, copper sulfide and gold NPs are assembled into more complex and hierarchical structures having complex chiroptical properties. Although further studies are necessary for conclusive results, we could see the possibility of controllable chiroptical properties which will facilitate the development of solution processed chiroptical devices.

In Chapter 5, we have confirmed the light-matter interaction can be permanently retained in light absorbing materials with a newly developed computational method, implementing 3D tomography imaging into theoretical calculations. The tomography technology breakthrough in the computational limitation caused by simplified model, proves the fact that the Au NPs produced with the light-driven method retained light-polarization information in their structure despite that they seem to have an irregular shape.

In Summary, this dissertation is devoted to the understanding of asymmetry of inorganic nanomaterial and developing experimental and computational strategies to engineer assembled materials with desirable properties. This dissertation is highly interdisciplinary over chemistry, nanotechnology, materials science, condensed matter physics, electronics, and optics and has been implemented by a variety of research techniques and instrumentation, including, but not limited to, computational simulations and electron microscopic analysis. Although this thesis work focused mostly on the simple chiroptical responses from the developed assemblies,

controllable nonlinear optical response from these asymmetrical/chiral structures would be another interesting direction.

Bibliography

1. S. C. Glotzer, M. J. Solomon, Anisotropy of building blocks and their assembly into complex structures. *Nat. Mater.* **6**, 557–562 (2007).
2. S. Kathleen, L. Eric, G. Moniraj, Oriented Assembly of Metamaterials. *Science*. **325**, 159–161 (2009).
3. M. C. Roco, W. S. Bainbridge, Converging technologies for improving human performance: Integrating from the nanoscale. *J. Nanoparticle Res.* **4**, 281–295 (2002).
4. M. C. Roco, The long view of nanotechnology development: The National Nanotechnology Initiative at 10 years. *J. Nanoparticle Res.* **13**, 427–445 (2011).
5. I. S. I. Web, S. This, H. Press, N. York, A. Nw, Plasmonics : Merging Photonics and. *Science*. **189**, 189–194 (2012).
6. S. K. Sahoo, S. Parveen, J. J. Panda, The present and future of nanotechnology in human health care. *Nanomedicine Nanotechnology, Biol. Med.* **3**, 20–31 (2007).
7. E. Prodan, C. Radloff, N. J. Halas, P. Nordlander, A hybridization model for the plasmon response of complex nanostructures. *Science*. **302**, 419–22 (2003).
8. N. M. Litchinitser, J. Sun, Optical meta-atoms: Going nonlinear. *Science*. **350**, 1033–1034 (2015).
9. J. Yan *et al.*, Reconfiguring active particles by electrostatic imbalance. *Nat. Mater.* **15**, 1095–1099 (2016).
10. N. M. Litchinitser, J. Sun, Optical meta-atoms: Going nonlinear. *Science*. **350**, 1033–1034 (2015).
11. J. Y. Kim, N. A. Kotov, Charge transport dilemma of solution-processed nanomaterials. *Chem. Mater.* **26** (2014), pp. 134–152.
12. X. K. Zhao, J. H. Fendler, Size Quantization in Semiconductor Particulate Films. *J. Phys. Chem.* **95**, 3716–3723 (1991).
13. J. Zuloaga, E. Prodan, P. Nordlander, Quantum plasmonics: Optical properties and tunability of metallic nanorods. *ACS Nano*. **4**, 5269–5276 (2010).
14. A. M. Funston, C. Novo, T. J. Davis, P. Mulvaney, Plasmon coupling of gold nanorods at short distances and in different geometries. *Nano Lett.* **9**, 1651–1658 (2009).
15. A. H. R. Koch *et al.*, Surface asymmetry of coated spherical nanoparticles. *Nano Lett.* **14**, 4138–4144 (2014).
16. X. Huang, I. H. El-Sayed, W. Qian, M. A. El-Sayed, Cancer cell imaging and photothermal therapy in the near-infrared region by using gold nanorods. *J. Am. Chem. Soc.* **128**, 2115–2120 (2006).
17. Y. Fu, J. Zhang, J. R. Lakowicz, Plasmon-enhanced fluorescence from single fluorophores

end-linked to gold nanorods. *J. Am. Chem. Soc.* **132**, 5540–5541 (2010).
18. X. Zou, S. Dong, Surface-enhanced Raman scattering studies on aggregated silver nanoplates in aqueous solution. *J. Phys. Chem. B*. **110**, 21545–21550 (2006).
19. P. Zijlstra, J. W. M. Chon, M. Gu, Five-dimensional optical recording mediated by surface plasmons in gold nanorods. *Nature*. **459**, 410–413 (2009).
20. J. Do, M. Fedoruk, F. Jäckel, J. Feldmann, Two-color laser printing of individual gold nanorods. *Nano Lett.* **13**, 4164–4168 (2013).
21. G. Von Maltzahn *et al.*, Computationally guided photothermal tumor therapy using long-circulating gold nanorod antennas. *Cancer Res.* **69**, 3892–3900 (2009).
22. P. Zijlstra, P. M. R. Paulo, M. Orrit, Optical detection of single non-absorbing molecules using the surface plasmon resonance of a gold nanorod. *Nat. Nanotechnol.* **7**, 379–382 (2012).
23. A. Kuzyk *et al.*, DNA-based self-assembly of chiral plasmonic nanostructures with tailored optical response. *Nature*. **483**, 311–314 (2012).
24. S. E. Lohse, C. J. Murphy, The quest for shape control: A history of gold nanorod synthesis. *Chem. Mater.* **25**, 1250–1261 (2013).
25. C. F. Bohren, D. R. Huffman, *Absorption and scattering of light by small particles* (John Wiley & Sons, New York, 1983).
26. M. Lien, Problems in Scattering and Imaging by. *Dr. Diss.* **Retrieved** (2017).
27. S. W. Prescott, P. Mulvaney, Gold nanorod extinction spectra. *J. Appl. Phys.* **99**, 123504 (2006).
28. M. Lippitz, M. a Dijk, M. Orrit, Third-harmonic generation from single gold nanoparticles. *Nano Lett.* **5**, 799–802 (2005).
29. O. Schwartz, D. Oron, Background-free third harmonic imaging of gold nanorods. *Nano Lett.* **9**, 4093–4097 (2009).
30. A. Singh, A. Lehoux, H. Remita, J. Zyss, I. Ledoux-Rak, Second harmonic response of gold nanorods: A strong enhancement with the aspect ratio. *J. Phys. Chem. Lett.* **4**, 3958–3961 (2013).
31. J. I. Dadap, J. Shan, K. B. Eisenthal, T. F. Heinz, Second-Harmonic Rayleigh Scattering from a Sphere of Centrosymmetric Material. *Phys. Rev. Lett.* **83**, 4045–4048 (1999).
32. J. I. Dadap, J. Shan, T. F. Heinz, Theory of optical second-harmonic generation from a sphere of centrosymmetric material: small-particle limit. *J. Opt. Soc. Am. B*. **21**, 1328–1347 (2004).
33. R. Janoschek, *Chirality: From weak bosons to the α-helix* (Springer-Verlag, Berlin, 1991).
34. H. Kitzerow, *Chirality in liquid crystals* (Springer, New York, 2001).
35. N. Berova, K. Nakanishi, R. W. Woody, *Circular dichroism: Principles and applications* (Wiley-VCH, New York, 2000).
36. Z. Fan, A. O. Govorov, Chiral nanocrystals: Plasmonic spectra and circular dichroism. *Nano Lett.* **12**, 3283–3289 (2012).
37. T. Hu *et al.*, Self-organization of plasmonic and excitonic nanoparticles into resonant chiral supraparticle assemblies. *Nano Lett.* **14**, 6799–6810 (2014).

38. K. Sawai, R. Tatumi, T. Nakahodo, H. Fujihara, Asymmetric Suzuki-Miyaura coupling reactions catalyzed by chiral palladium nanoparticles at room temperature. *Angew. Chemie - Int. Ed.* **47**, 6917–6919 (2008).
39. V. I. Kopp *et al.*, Chiral fiber gratings. *Science*. **305**, 74–75 (2004).
40. E. R. Trivedi *et al.*, Chiral porphyrazine near-IR optical imaging agent exhibiting preferential tumor accumulation. *Proc. Natl. Acad. Sci. U. S. A.* **107**, 1284–1288 (2010).
41. R. Yang, Z. L. Wang, Springs, rings, and spirals of rutile-structured tin oxide nanobelts. *J. Am. Chem. Soc.* **128**, 1466–1467 (2006).
42. P. X. Gao, W. Mai, Z. L. Wang, Superelasticity and nanofracture mechanics of ZnO nanohelices. *Nano Lett.* **6**, 2536–2543 (2006).
43. A. M. Seddon, H. M. Patel, S. L. Burkett, S. Mann, Chiral templating of silica-lipid lamellar mesophase with helical tubular architecture. *Angew. Chemie - Int. Ed.* **41**, 2988–2991 (2002).
44. J. H. Zhu, S. H. Yu, A. W. Xu, H. Cölfen, The biomimetic mineralization of double-stranded and cylindrical helical BaCO3nanofibres. *Chem. Commun.*, 1106–1108 (2009).
45. W. Ma *et al.*, Chiral Inorganic Nanostructures. *Chem. Rev.* **117**, 8041–8093 (2017).
46. M. N'Gom *et al.*, Electron-beam mapping of plasmon resonances in electromagnetically interacting gold nanorods. *Phys. Rev. B - Condens. Matter Mater. Phys.* **80**, 1–4 (2009).
47. B. S. Guiton *et al.*, Correlated optical measurements and plasmon mapping of silver nanorods. *Nano Lett.* **11**, 3482–3488 (2011).
48. D. Rossouw, M. Couillard, J. Vickery, E. Kumacheva, G. A. Botton, Multipolar plasmonic resonances in silver nanowire antennas imaged with a subnanometer electron probe. *Nano Lett.* **11**, 1499–1504 (2011).
49. E. J. R. Vesseur, R. De Waele, M. Kuttge, A. Polman, Direct observation of plasmonic modes in Au nanowires using high-resolution cathodoluminescence spectroscopy. *Nano Lett.* **7**, 2843–2846 (2007).
50. K. Imura, T. Nagahara, H. Okamoto, Near-field two-photon-induced photoluminescence from single gold nanorods and imaging of plasmon modes. *J. Phys. Chem. B*. **109**, 13214–13220 (2005).
51. X. Zhou *et al.*, Quantitative super-resolution imaging uncovers reactivity patterns on single nanocatalysts. *Nat. Nanotechnol.* **7**, 237–41 (2012).
52. I. Russier-Antoine, E. Benichou, G. Bachelier, C. Jonin, P. F. Brevet, Multipolar Contributions of the Second Harmonic Generation from Silver and Gold Nanoparticles. *J. Phys. Chem. C*. **111**, 9044–9048 (2007).
53. C. Hubert *et al.*, Role of surface plasmon in second harmonic generation from gold nanorods. *Appl. Phys. Lett.* **90**, 88–91 (2007).
54. M. B. Mohamed, V. Volkov, S. Link, M. A. El-Sayed, The `lightning' gold nanorods: fluorescence enhancement of over a million compared to the gold metal. *Chem. Phys. Lett.* **317**, 517–523 (2000).
55. N. Verellen *et al.*, Two-photon luminescence of gold nanorods mediated by higher order plasmon modes. *ACS Photonics*. **2**, 410–416 (2015).

56. J. Butet *et al.*, Optical second harmonic generation of single metallic nanoparticles embedded in a homogeneous medium. *Nano Lett.* **10**, 1717–1721 (2010).
57. G. Bachelier, I. Russier-Antoine, E. Benichou, C. Jonin, P.-F. Brevet, Multipolar second-harmonic generation in noble metal nanoparticles. *J. Opt. Soc. Am. B*. **25**, 955 (2008).
58. P. Ray, Size and shape dependent second order nonlinear optical properties of nanomaterials and their application in biological and chemical sensing. *Chem. Rev.* **110**, 5332–5365 (2010).
59. V. Knittel *et al.*, Nonlinear Photoluminescence Spectrum of Single Gold Nanostructures. *ACS Nano*. **9**, 894–900 (2015).
60. E. C. Hao, G. C. Schatz, R. C. Johnson, J. T. Hupp, Hyper-Rayleigh scattering from silver nanoparticles. *J. Chem. Phys.* **117**, 5963–5966 (2002).
61. M. Beversluis, A. Bouhelier, L. Novotny, Continuum generation from single gold nanostructures through near-field mediated intraband transitions. *Phys. Rev. B*. **68**, 1–10 (2003).
62. C. J. Johnson, E. Dujardin, S. A. Davis, C. J. Murphy, S. Mann, Growth and form of gold nanorods prepared by seed-mediated, surfactant-directed synthesis. *J. Mater. Chem.* **12**, 1765–1770 (2002).
63. B. Goris *et al.*, Atomic-scale determination of surface facets in gold nanorods. *Nat. Mater.* **11**, 930–935 (2012).
64. B. Nikoobakht, M. A. El-Sayed, Preparation and Growth Mechanism of Gold Nanorods (NRs) Using Seed - Mediated Growth Method. *Chem. Mater.* **15**, 1957–1962 (2003).
65. S. K. Meena, M. Sulpizi, Understanding the Microscopic Origin of Gold Nanoparticle Anisotropic Growth from Molecular Dynamics Simulations. *Langmuir*. **29**, 14954–14961 (2013).
66. H. Katz-Boon *et al.*, Three-dimensional morphology and crystallography of gold nanorods. *Nano Lett.* **11**, 273–278 (2011).
67. M. J. Polking *et al.*, Ferroelectric order in individual nanometre-scale crystals. *Nat. Mater.* **11**, 700–709 (2012).
68. E. Volkl, L. F. Allard, D. C. Joy, *Introduction to electron holography* (1999).
69. A. Sanchez, M. A. Ochando, Calculation of the mean inner potential. *J. Phys. C Solid State Phys.* **18**, 33–41 (1985).
70. A. Gole, C. J. Murphy, Polyelectrolyte-coated gold nanorods: Synthesis, characterization and immobilization. *Chem. Mater.* **17**, 1325–1330 (2005).
71. A. P. Leonov *et al.*, Detoxification of gold nanorods by treatment with polystyrenesulfonate. *ACS Nano*. **2**, 2481–2488 (2008).
72. S. Magonov, J. Alexander, Single-pass Kelvin force microscopy and dC/dZ measurements in the intermittent contact: applications to polymer materials. *Beilstein J. Nanotechnol.* **2**, 15–27 (2011).
73. B. Nikoobakht, M. A. El-Sayed, Preparation and Growth Mechanism of Gold Nanorods (NRs) Using Seed - Mediated Growth Method. *Chem. Mater.* **15**, 1957–1962 (2003).
74. R. A. Farrer, F. L. Butterfield, V. W. Chen, J. T. Fourkas, Highly efficient multiphoton-

absorption-induced luminescence from gold nanoparticles. *Nano Lett.* **5**, 1139–1142 (2005).
75. M. Lien *et al.*, Optical Asymmetry and Nonlinear Light Scattering from Colloidal Gold Nanorods. **11**, 5925–5932 (2017).
76. S. Farid, M. Choi, D. Datta, M. A. Stroscio, M. Dutta, Spontaneous polarization induced electric field in zinc oxide nanowires and nanostars. *J. Appl. Phys.* **119**, 163108 (2016).
77. M. Shim, P. Guyot-Sionnest, Permanent dipole moment and charges in colloidal semiconductor quantum dots. *J. Chem. Phys.* **111**, 6955–6964 (1999).
78. S. Shanbhag, N. A. Kotov, On the origin of a permanent dipole moment in nanocrystals with a cubic crystal lattice: Effects of truncation, stabilizers, and medium for CdS tetrahedral homologues. *J. Phys. Chem. B*. **110**, 12211–12217 (2006).
79. S. Dag, S. Wang, L.-W. Wang, Large surface dipole moments in ZnO nanorods. *Nano Lett.* **11**, 2348–2352 (2011).
80. Y. Yang *et al.*, Size Dependence of Dielectric Constant in a Single Pencil-Like ZnO Nanowire. **12**, 10–13 (2012).
81. G. Morello *et al.*, Intrinsic optical nonlinearity in colloidal seeded grown CdSe/CdS nanostructures: Photoinduced screening of the internal electric field. *Phys. Rev. B - Condens. Matter Mater. Phys.* **78**, 1–8 (2008).
82. F. Van Mourik, G. Giraud, D. Tonti, M. Chergui, G. Van Der Zwan, Linear dichroism of CdSe nanodots: Large anisotropy of the band-gap absorption induced by ground-state dipole moments. *Phys. Rev. B - Condens. Matter Mater. Phys.* **77**, 1–6 (2008).
83. W.-K. Hong *et al.*, Tunable Electronic Transport Characteristics of Surface-Architecture-Controlled ZnO Nanowire Field Effect Transistors. *Nano Lett.* **8**, 950–956 (2008).
84. W. Feng *et al.*, Assembly of mesoscale helices with near-unity enantiomeric excess and light-matter interactions for chiral semiconductors. *Sci. Adv.* **3**, e1601159 (2017).
85. Z. Tang, N. A. Kotov, M. Giersig, Spontaneous Organization of Single CdTe Nanoparticles into Luminescent Nanowires. *Science*. **297**, 237–240 (2002).
86. W. Ma *et al.*, Chiral plasmonics of self-assembled nanorod dimers. *Sci. Rep.* **3**, 1934 (2013).
87. L. Gou, C. J. Murphy, Tuning the Shape of Gold Nanorods. *Chem. Mater.* **17**, 3668–3672 (2005).
88. G. Decher, Fuzzy Nanoassemblies: Toward Layered Polymeric Multicomposites. *Science*. **277**, 1232–1237 (1997).
89. L. Reimer, Energy-Filtering Transmission Electron Microscopy. *Adv. Electron. Electron Phys.* **81**, 43–126 (1991).
90. R. F. Egerton, Electron energy-loss spectroscopy in the TEM. *Reports Prog. Phys.* **72**, 16502 (2009).
91. F. Hofer, W. Grogger, G. Kothleitner, P. Warbichler, Quantitative analysis of EFTEM elemental distribution images. *Ultramicroscopy*. **67**, 83–103 (1997).
92. D. A. Walker, C. E. Wilmer, B. Kowalczyk, K. J. M. Bishop, B. A. Grzybowski, Precision assembly of oppositely and like-charged nanoobjects mediated by charge-induced dipole

interactions. *Nano Lett.* **10**, 2275–2280 (2010).
93. T. J. Collins, ImageJ for microscopy. *Biotechniques*. **43**, 25–30 (2007).
94. J. Pérez-Juste, B. Rodríguez-González, P. Mulvaney, L. M. Liz-Marzán, Optical control and patterning of gold-nanorod-poly(vinyl alcohol) nanocomposite films. *Adv. Funct. Mater.* **15**, 1065–1071 (2005).
95. M. Kauranen, A. V. Zayats, Nonlinear plasmonics. *Nat. Photonics*. **6**, 737–748 (2012).
96. S. Link, M. B. Mohamed, M. A. El-Sayed, Simulation of the Optical Absorption Spectra of Gold Nanorods as a Function of Their Aspect Ratio and the Effect of the Medium Dielectric Constant. *J. Phys. Chem. B*. **103**, 3073–3077 (1999).
97. P. K. Jain, K. S. Lee, I. H. El-Sayed, M. a El-Sayed, Calculated absorption and scattering properties of gold nanoparticles of different size, shape, and composition: applications in biological imaging and biomedicine. *J. Phys. Chem. B*. **110**, 7238–48 (2006).
98. W. Ni, X. Kou, Z. Yang, J. Wang, Tailoring longitudinal surface plasmon wavelengths, scattering and absorption cross sections of gold nanorods. *ACS Nano*. **2**, 677–686 (2008).
99. D. Fava, Z. Nie, M. A. Winnik, E. Kumacheva, Evolution of self-assembled structures of polymer-terminated gold nanorods in selective solvents. *Adv. Mater.* **20**, 4318–4322 (2008).
100. J. York, D. Spetzler, F. Xiong, W. D. Frasch, Single-molecule detection of DNA via sequence-specific links between F1-ATPase motors and gold nanorod sensors. *Lab Chip*. **8**, 415–9 (2008).
101. H. Wang *et al.*, In vitro and in vivo two-photon luminescence imaging of single gold nanorods. *Proc. Natl. Acad. Sci. U. S. A.* **102**, 15752–15756 (2005).
102. X. Huang, I. H. El-Sayed, W. Qian, M. a. El-Sayed, Cancer cell imaging and photothermal therapy in the near-infrared region by using gold nanorods. *J. Am. Chem. Soc.* **128**, 2115–2120 (2006).
103. N. Durr *et al.*, Two-photon luminescence imaging of cancer cells using molecularly targeted gold nanorods. *Nano Lett.* **7**, 941–945 (2007).
104. G. T. Boyd, Z. H. Yu, Y. R. Shen, Photoinduced luminescence from the noble metals and its enhancement on roughened surfaces. *Phys. Rev. B*. **33**, 7923–7936 (1986).
105. R. a. Farrer, F. L. Butterfield, V. W. Chen, J. T. Fourkas, Highly Efficient Multiphoton-Abrortion-Induced Luminescence from Gold Nanoparticles. *Nano Lett.* **5**, 1139–1142 (2005).
106. L. Tong, Q. Wei, A. Wei, J.-X. Cheng, Gold Nanorods as Contrast Agents for Biological Imaging: Optical Properties, Surface Conjugation and Photothermal Effects. *Photochem. Photobiol.* **85**, 21–32 (2009).
107. A. Bouhelier *et al.*, Surface plasmon characteristics of tunable photoluminescence in single gold nanorods. *Phys. Rev. Lett.* **95** (2005).
108. G. Y. Panasyuk, J. C. Schotland, V. A. Markel, Classical theory of optical nonlinearity in conducting nanoparticles. *Phys. Rev. Lett.* **100** (2008).
109. B. Nik, M. El-Sayed, Preparation and Growth Mechanism of Gold Nanorods (NRs) Using Seed - Mediated Growth Method. *Chem. Mater.* **15**, 1957–1962 (2003).

110. J.-Y. Kim *et al.*, in *251st American Chemical Society National meeting & Exposition* (American Chemical Society, San Diego, 2016), p. 244.
111. E. Völkl, L. F. Allard, D. C. Joy, *Introduction to Electron Holography* (Springer US, 1999), vol. 53.
112. R. W. Boyd, *Nonlinear Optics* (2008).
113. R. H. M. Groeneveld, R. Sprik, A. Lagendijk, Femtosecond spectroscopy of electron-electron and electron-phonon energy relaxation in Ag and Au. *Phys. Rev. B*. **51**, 11433–11445 (1995).
114. M. Perner *et al.*, Optically Induced Damping of the Surface Plasmon Resonance in Gold Colloids. *Phys. Rev. Lett.* **78**, 2192–2195 (1997).
115. Z. Lin, L. V. Zhigilei, V. Celli, Electron-phonon coupling and electron heat capacity of metals under conditions of strong electron-phonon nonequilibrium. *Phys. Rev. B*. **77** (2008).
116. G. S. Agarwal, Quantum electrodynamics in the presence of dielectrics and conductors. I. Electromagnetic-field response functions and black-body fluctuations in finite geometries. *Phys. Rev. A*. **11**, 230–242 (1975).
117. G. S. Agarwal, Brownian Motion of a Quantum Oscillator. *Phys. Rev. A*. **4**, 739–747 (1971).
118. S. Link, M. A. Ei-Sayed, Spectroscopic determination of the melting energy of a gold nanorod. *J. Chem. Phys.* **114**, 2362–2368 (2001).
119. P. X. Gao *et al.*, Conversion of zinc oxide nanobelts into superlattice-structured nanohelices. *Science*. **309**, 1700–1704 (2005).
120. D. Moore, Y. Ding, L. W. Zhong, Hierarchical structured nanohelices of ZnS. *Angew. Chemie - Int. Ed.* **45**, 5150–5154 (2006).
121. G. Z. Shen *et al.*, Single-crystalline cubic structured InP nanosprings. *Appl. Phys. Lett.* **88**, 3–6 (2006).
122. V. Y. Prinz *et al.*, Free-standing and overgrown InGaAs/GaAs nanotubes, nanohelices and their arrays. *Phys. E Low-Dimensional Syst. Nanostructures*. **6**, 828–831 (2000).
123. E. D. Sone, E. R. Zubarev, S. I. Stupp, Semiconductor nanohelices templated by supramolecular ribbons. *Angew. Chem. Int. Ed.* **41**, 1705–1709 (2002).
124. C. Tan *et al.*, Self-assembled chiral nanofibers from ultrathin low-dimensional nanomaterials. *J. Am. Chem. Soc.* **137**, 1565–1571 (2015).
125. E. L. Ivchenko, B. Spivak, Chirality effects in carbon nanotubes. *Phys. Rev. B*. **66**, 155404 (2002).
126. A. Sánchez-Castillo, C. E. Román-Velázquez, C. Noguez, Optical circular dichroism of single-wall carbon nanotubes. *Phys. Rev. B*. **73**, 045401 (2006).
127. S. Liu, Y. Duan, X. Feng, J. Yang, S. Che, Synthesis of enantiopure carbonaceous nanotubes with optical activity. *Angew. Chemie - Int. Ed.* **52**, 6858–6862 (2013).
128. H. Matsukizono, R. H. Jin, High-temperature-resistant chiral silica generated on chiral crystalline templates at neutral pH and ambient conditions. *Angew. Chemie - Int. Ed.* **51**, 5862–5865 (2012).

129. B. Liu *et al.*, Growth of optically active chiral inorganic films through DNA self-assembly and silica mineralisation. *Sci. Rep.* **4** (2014), doi:10.1038/srep04866.
130. X. Wu *et al.*, Unexpected chirality of nanoparticle dimers and ultrasensitive chiroplasmonic bioanalysis. *J. Am. Chem. Soc.* **135**, 18629–18636 (2013).
131. W. Ma *et al.*, Attomolar DNA detection with chiral nanorod assemblies. *Nat. Commun.* **4**, 2689 (2013).
132. A. Sharma *et al.*, Detecting, visualizing, and measuring gold nanoparticle chirality using helical pitch measurements in nematic liquid crystal phases. *ACS Nano*. **8**, 11966–11976 (2014).
133. S. D. Elliott, M. P. Moloney, Y. K. Gun'ko, Chiral shells and achiral cores in CdS quantum dots. *Nano Lett.* **8**, 2452–2457 (2008).
134. M. V. Mukhina *et al.*, Intrinsic chirality of CdSe/ZnS quantum dots and quantum rods. *Nano Lett.* **15**, 2844–2851 (2015).
135. A. S. Baimuratov, I. D. Rukhlenko, Y. K. Gun'ko, A. V Baranov, A. V Fedorov, Dislocation-induced chirality of semiconductor nanocrystals. *Nano Lett.* **15**, 1710–1715 (2015).
136. Y. Zhou, M. Yang, K. Sun, Z. Tang, N. A. Kotov, Similar topological origin of chiral centers in organic and nanoscale inorganic structures: Effect of stabilizer chirality on optical isomerism and growth of CdTe nanocrystals. *J. Am. Chem. Soc.* **132**, 6006–6013 (2010).
137. J. Yeom *et al.*, Chiral templating of self-assembling nanostructures by circularly polarized light. *Nat. Mater.* **14**, 66–72 (2014).
138. C. A. Silvera Batista, R. G. Larson, N. A. Kotov, Nonadditivity of nanoparticle interactions. *Science*. **350**, 1242477–1242477 (2015).
139. A. M. Smith, M. C. Mancini, S. Nie, Bioimaging: Second window for in vivo imaging. *Nat. Nanotechnol.* **4**, 710–711 (2009).
140. Z. Y. Wang, *Near-Infrared Organic Materials and Emerging Applications* (CRC Press, Boca Raton, 2013).
141. D. J. Mulla, Twenty five years of remote sensing in precision agriculture: Key advances and remaining knowledge gaps. *Biosyst. Eng.* **114**, 358–371 (2013).
142. R. G. Driggers, V. Hodgkin, R. Vollmerhausen, in *Proc. SPIE 8706, Infrared Imaging Systems: Design, Analysis, Modeling, and Testing XXIV* (Baltimore, 2013), p. 87060L.
143. Y. Zhou *et al.*, Biomimetic hierarchical assembly of helical supraparticles from chiral nanoparticles. *ACS Nano*. **10**, 3248–3256 (2016).
144. S. Che *et al.*, Synthesis and characterization of chiral mesoporous silica. *Nature*. **429**, 281–285 (2004).
145. G. Singh *et al.*, Self-assembly of magnetite nanocubes into helical superstructures. *Science*. **345**, 1149–1153 (2014).
146. J. Zhu *et al.*, Formation of chiral branched nanowires by the Eshelby Twist. *Nat. Nanotechnol.* **3**, 477–481 (2008).
147. D. M. Hall, I. R. Bruss, J. R. Barone, G. M. Grason, Morphology selection via geometric

frustration in chiral filament bundles. *Nat. Mater.* **15**, 727–732 (2016).
148. Z. Tang, Y. Wang, K. Sun, N. A. Kotov, Spontaneous transformation of stabilizer-depleted binary semiconductor nanoparticles into selenium and tellurium nanowires. *Adv. Mater.* **17**, 358–363 (2005).
149. Z. Tang, Y. Wang, S. Shanbhag, M. Giersig, N. A. Kotov, Spontaneous transformation of CdTe nanoparticles into angled Te nanocrystals: From particles and rods to checkmarks, X-marks, and other unusual shapes. *J. Am. Chem. Soc.* **128**, 6730–6736 (2006).
150. M. M. Safont-Sempere, G. Fern, W. Frank, Self-sorting phenomena in complex supramolecular systems. *Chem. Rev.* **111**, 5784–5814 (2011).
151. B. Adhikari, J. Nanda, A. Banerjee, Multicomponent hydrogels from enantiomeric amino acid derivatives: Helical nanofibers, handedness and self-sorting. *Soft Matter*. **7**, 8913 (2011).
152. H. Sun *et al.*, Homochiral columns constructed by chiral self-sorting during supramolecular helical organization of hat-shaped molecules. *J. Am. Chem. Soc.* **136**, 7169–7185 (2014).
153. T. Koga, M. Matsuoka, N. Higashi, Structural control of self-assembled nanofibers by artificial β-sheet peptides composed of D- or L-isomer. *J. Am. Chem. Soc.* **127**, 17596–17597 (2005).
154. A. Klug, The tobacco mosaic virus particle: structure and assembly. *Philos Trans R Soc L. B Biol Sci*. **354**, 531–535 (1999).
155. E. Yashima, K. Maeda, Chirality-responsive helical polymers. *Macromolecules*. **41**, 3–12 (2008).
156. W. Yan *et al.*, Self-assembly of chiral nanoparticle pyramids with strong R/S optical activity. *J. Am. Chem. Soc.* **134**, 15114–15121 (2012).
157. P. McPhie, Circular dichroism studies on proteins in films and in solution: Estimation of secondary structure by g-factor analysis. *Anal. Biochem.* **293**, 109–119 (2001).
158. B. A. San Jose, S. Matsushita, K. Akagi, Lyotropic chiral nematic liquid crystalline aliphatic conjugated polymers based on disubstituted polyacetylene derivatives that exhibit high dissymmetry factors in circularly polarized luminescence. *J. Am. Chem. Soc.* **134**, 19795–19807 (2012).
159. B. N. Khlebtsov, N. G. Khlebtsov, Multipole plasmons in metal nanorods: Scaling properties and dependence on particle size, shape, orientation, and dielectric environment. *J. Phys. Chem. C*. **111**, 11516–11527 (2007).
160. E. K. Payne, K. L. Shuford, S. Park, G. C. Schatz, C. A. Mirkin, Multipole plasmon resonances in gold nanorods. *J. Phys. Chem. B*. **110**, 2150–2154 (2006).
161. I. O. Sosa, C. Noguez, R. G. Barrera, Optical properties of metal nanoparticles with arbitrary shapes. *J. Phys. Chem. B*. **107**, 6269–6275 (2003).
162. C. Noguez, Surface plasmons on metal nanoparticles: The influence of shape and physical environment. *J. Phys. Chem. C*. **111**, 3806–3819 (2007).
163. J. H. Singh, G. Nair, A. Ghosh, A. Ghosh, Wafer scale fabrication of porous three-dimensional plasmonic metamaterials for the visible region: Chiral and beyond.

Nanoscale. **5**, 7224–7228 (2013).
164. A. Guerrero-Martínez *et al.*, Intense optical activity from three-dimensional chiral ordering of plasmonic nanoantennas. *Angew. Chemie - Int. Ed.* **50**, 5499–5503 (2011).
165. L. Y. Wang *et al.*, Circular differential scattering of single chiral self-assembled gold nanorod dimers. *ACS Photonics*. **2**, 1602–1610 (2015).
166. B. Auguié, J. L. Alonso-Gómez, A. Guerrero-Martínez, L. M. Liz-Marzán, Fingers crossed: Optical activity of a chiral dimer of plasmonic nanorods. *J. Phys. Chem. Lett.* **2**, 846–851 (2011).
167. K. Antoine, Fermi level, work function and vacuum level. *Mater. Horizons*. **3**, 7–10 (2015).
168. N. Gaponik *et al.*, Thiol-capping of CdTe nanocrystals: An alternative to organometallic synthetic routes. *J. Phys. Chem. B*. **106**, 7177–7185 (2002).
169. W. W. Yu, L. Qu, W. Guo, X. Peng, Experimental determination of the extinction coefficient of CdTe, CdSe, and CdS nanocrystals. *Chem. Mater.* **15**, 2854–2860 (2003).
170. G. Ma *et al.*, Self-assembly of copper sulfide nanoparticles into nanoribbons with continuous crystallinity. *ACS Nano*. **7**, 9010–9018 (2013).
171. G. Ma *et al.*, Self-Assembly of Copper Sul fi de Nanoparticles into Nanoribbons with Continuous Crystallinity, 9010–9018 (2013).
172. C. Chung, K. J. Lampe, S. C. Heilshorn, Tetrakis(hydroxymethyl) phosphonium chloride as a covalent cross-linking agent for cell encapsulation within protein-based hydrogels. *Biomacromolecules*. **13**, 3912–3916 (2012).
173. S. N. Sarangi, A. M. P. Hussain, S. N. Sahu, Strong UV absorption and emission from L-cysteine capped monodispersed gold nanoparticles. *Appl. Phys. Lett.* **95**, 1–4 (2009).
174. A. Y. Mulkidjanian, On the origin of life in the zinc world: 1. Photosynthesizing, porous edifices built of hydrothermally precipitated zinc sulfide as cradles of life on Earth. *Biol. Direct*. **4** (2009), doi:10.1186/1745-6150-4-26.
175. J. Zhang, M. R. Langille, C. A. Mirkin, Photomediated synthesis of silver triangular bipyramids and prisms: The effect of pH and BSPP. *J. Am. Chem. Soc.* **132**, 12502–12510 (2010).
176. T. Nanoplates, S. Templates, F. Generating, T. Nanorings, Triangular Nanoplates of Silver: Synthesis, Characterization, and Use as Sacrificial Templates For Generating Triangular Nanorings of Gold**. *Adv. Mater.* **15**, 695–699 (2003).
177. G. P. Lee *et al.*, Light-driven transformation processes of anisotropic silver nanoparticles. *ACS Nano*. **7**, 5911–5921 (2013).
178. R. Jin *et al.*, Photoinduced conversion of silver nanospheres to nanoprisms. *Science*. **294**, 1901–1904 (2001).
179. M. Maillard, P. Huang, L. Brus, Silver Nanodisk Growth by Surface Plasmon Enhanced Photoreduction of Adsorbed [Ag +]. *Nano Lett.* **3**, 1611–1615 (2003).
180. Y. Wang, J. Xu, Y. Wang, H. Chen, Emerging chirality in nanoscience. *Chem. Soc. Rev.* **42**, 2930–2962 (2013).
181. J. K. Gansel *et al.*, Gold helix photonic metamaterial as broadband circular polarizer.

Science. **1513**, 1513–1515 (2009).
182. A. B. Buda, K. Mislow, A Hausdorff Chirality Measure. *J. Am. Chem. Soc.* **114**, 6006–6012 (1992).
183. J. Yeom *et al.*, Chiral templating of self-assembling nanostructures by circularly polarized light. *Nat. Mater.* **14**, 66–72 (2015).
184. K. Kurihara, J. Kizling, P. Stenius, J. H. Fendler, Laser and pulse radiolytically induced colloidal gold formation in water and in water-in-oil microemulsions. *J. Am. Chem. Soc.* **105**, 2574–2579 (1983).
185. A. Rassat, Un critère de classement des systèmes chiraux de points à partir de la distance au sens de Haussdorf. *Compt. Rend. Acad. Sci.* **299**, 53 (1984).
186. H. Zabrodsky, D. Avnir, Continuous Symmetry Measures . 4 . Chirality. *J. Am. Chem. Soc.* **117**, 462–473 (1995).
187. M. A. Osipov, B. T. Pickup, D. A. Dunmur, A new twist to molecular chirality : intrinsic chirality indices. *Mol. Phys.* **84**, 1193–1206 (1995).
188. J. R. Kremer, D. N. Mastronarde, J. R. McIntosh, Computer visualization of three-dimensional image data using IMOD. *J. Struct. Biol.* **116**, 71–6 (1996).
189. P. B. Johnson, R. W. Christy, Optical constants of the noble metals. *Phys. Rev. B*. **6**, 4370–4379 (1972).